

© Copyright 2010

Varun Gupta.

All Rights Reserved

DETERMINATION OF STRUCTURAL CHANGES AND PHASE
TRANSFORMATIONS IN BORON CARBIDE BY STATIC AND DYNAMIC
STUDIES

By

VARUN GUPTA

A dissertation submitted to the Graduate School-New Brunswick

Rutgers, The State University of New Jersey

In partial fulfillment of the requirements

For the degree of

Doctor of Philosophy

Graduate Program in Materials Science and Engineering

Written under the direction of

Prof. Manish Chhowalla

And approved by

New Brunswick, New Jersey

May, 2010

ABSTRACT OF THE DISSERTATION

Determination of structural changes and phase transformations in boron carbide by static
and dynamic studies

VARUN GUPTA

Dissertation Director: Manish Chhowalla, Ph.D.

Recent transmission electron microscopy results demonstrate that the failure of B_4C is commensurate with the segregation of boron icosahedra embedded in amorphous carbon in 2–3 nm wide amorphous bands along the (113) lattice direction, in good agreement with our recent theoretical results. Boron carbide is generally composed of multiple polytypes of B_4C which have the same primitive lattice parameters but differ from each other by the location of the boron and carbon atoms in the unit cells. The unit cells are formed by a 12-atom $B_{12-n}C_n$ icosahedron and a 3-atom $(C_{3-n}B_n)$ chain. Our theoretical results indicate that one polytype, $B_{12}(C_3)$, whose formation is responsible for the failure of the entire material. This anomalous and poorly understood glass-like behavior in boron carbide has been the subject of research since its discovery over 70 years ago.

The characterization of disorder in hot pressed and powder boron carbide samples is therefore of primary interest. The research work has focused on characterization techniques which can be used at a micrometric sampling size so that individual powder grains of the material can be utilized. Specifically, micro-Raman and electrical conductivity measurements can be used with micrometric gap cells to understand the disorder in B_4C . The results also demonstrate that it is possible to induce transformations in boron carbide using electric fields that are comparable with those obtained under shock and nanoindentation.

Our calculations present a hypothesis which can provide a solution to prevent the premature failure of B_4C . A route to achieve suppression of the $B_{12}(CCC)$ polytype without significantly affecting the elastic constants is via low concentration Silicon (Si) doping of B_4C . Suppression of $B_{12}(CCC)$ by Si doping has implications towards development of boron carbide armor with improved properties for protection against high velocity threats. In order to achieve this, nanostructures (nanowires, nanorods, etc.) of Si-doped boron carbide have been synthesized using a Solid-Liquid-Solid (SLS) growth mechanism. The resulting structures have been characterized by SEM, TEM and Raman spectroscopy and consolidated to evaluate their mechanical properties. In addition, the application of nanowires in a transparent and thermally conducting nanocomposite is demonstrated.

DEDICATIONS

My PhD thesis is dedicated to my father (Krishan Gopal Gupta), who always motivated us (my sister and I) to be the best in all our endeavors. His constant support and resourceful advice, guided me at every step of my life. Without his sacrifices, I would not be able to do this thesis and all my education. This thesis is also dedicated to my mother (Beena Gupta) and my sister (Neha Gupta) for their constant support and encouragement.

ACKNOWLEDGMENTS

I would like to express my gratitude to my thesis advisor, Prof. Manish Chhowalla, for his guidance, constant support and help in many aspects of my graduate studies and research work. I would like to thank, Prof. Adrian Mann, for his understanding, trust and support given throughout the course of my graduate studies and my committee members, Prof. Lisa Klein, Prof. Frederic Cosandey and Prof. Giovanni Fanchini.

Above all, my deepest gratitude goes to my parents, my sister and my girl friend for their continued moral support and endurance in helping me in accomplishing my goal.

I would like to give my thanks to Steve Miller and Alokik Kanwal for their constant motivation and help. I also wish to thank all my friends, colleagues, faculty and staff members in the Department of Materials Science and Engineering who gave me the opportunity to learn from their advice and who have made my stay here at Rutgers unforgettable. Others who have made my work here at Rutgers University stimulating and enjoyable include: John Yaniero, Claudia Kuchinow, Phyllis Cassell, Sara Reynaud, Cecilia Mattevi, Sueng Yol Jeung, Kendall Mills, James Fischer, James Kantor, Dr. Jafar Al Sharab, Prof. Rich Haber and Prof. Dale Niesz. I would like to thank my collaborators in Oak Ridge National Laboratory, Army Research Laboratory and Chungju National University, South Korea.

This work was made possible with support from National Science Foundation (NSF) and Army Research Laboratory (ARL). Any opinions, findings, and conclusions or recommendations expressed in this thesis are those of the author and do not reflect the views of NSF and ARL.

TABLE OF CONTENTS

ABSTRACT OF THE DISSERTATION	ii
DEDICATIONS.....	iv
ACKNOWLEDGMENTS	v
TABLE OF CONTENTS.....	vi
LIST OF TABLES.....	x
LIST OF FIGURES	xi
 CHAPTER 1 INTRODUCTION	 1
 1.1 Motivation.....	 2
1.2 Chapter Outline.....	3
 CHAPTER 2 BACKGROUND AND LITERATURE REVIEW	 6
 2.1 History of Boron Carbide	 7
2.2 Synthesis Methods	8
2.3 Boron Carbide: Structure and Defects	9
2.4 Properties and Applications	12
2.4.1 Chemical Stability	13
2.4.2 Hardness and Density	13
2.4.3 Limitations of Boron Carbide.....	14
2.4.4 Doping in Boron Carbide	25
 CHAPTER 3 EXPERIMENTAL TECHNIQUES	 27
 3.1 Indentation	 28
3.2 Nano-Indentation	28
3.3 Raman Spectroscopy	31

3.3.1 Surface Enhanced Raman Spectroscopy (SERS)	33
3.4 Scanning Electron Microscopy (SEM) Characterization	35
3.5 Transmission Electron Microscopy (TEM) Characterization.....	38
3.5.1 General Concept of Transmission Electron Microscopy.....	38
3.5.2 Electron Diffraction.....	41
CHAPTER 4 STATIC INDENTATION STUDIES	45
4.1 Introduction.....	46
4.2 Experimental Details	48
4.2.1 Size of the sp^2 aromatic domains.....	51
4.2.2 Concentration of the inclusions	52
4.3 Results and Discussion	54
4.3.1 Powder samples	54
4.3.2 As prepared hot-pressed sample.....	57
4.3.3 Indented hot-pressed sample	60
4.3.4 Surface-enhanced Raman spectroscopy (SERS) on the hot- pressed indented sample	64
4.3.5 Origin of the dispersive peak between $1700 - 1800\text{ cm}^{-1}$	67
4.4 Summary and Conclusions	68

CHAPTER 5 <i>IN-SITU</i> MONITORING OF STRUCTURAL CHANGES UNDER ELECTRICAL FIELDS.....	69
5.1 Phase Transformations of Boron Carbide.....	70
5.2 Experimental Details of the samples	72
5.3 Results and Discussion	73
5.4 Conclusion	81
 CHAPTER 6 SYNTHESIS AND SILICON DOPING OF BORON CARBIDE NANOWIRES.....	 82
6.1 Nanowires and Nanostructures of Boron Carbide	83
6.2 Synthesis Method and Characterization Techniques	84
6.2.1 Synthesis.....	84
6.2.2 Characterization.....	85
6.3 Parametric Study for the Growth of Boron Carbide Nanowires.....	86
6.3.1 Effect of Boron to Carbon Ratio	86
6.3.2 Effect of Temperature.....	88
6.3.3 Effect of addition of Silicon	92
6.3.4 Thermo Gravimetric Analysis (TGA)	98
6.3.5 Summary of the diameter and length distributions.....	101
6.3.6 Discussion of the growth mechanism.....	104
6.4 Summary	112

CHAPTER 7 NANOCOMPOSITES FROM ULTRA-LONG BORON CARBIDE NANOWIRES AND POLY(METHYL METHACRYLATE)	113
7.1 Introduction.....	114
7.2 Method and Experimental Details	115
7.3 Results and Discussion	117
7.4 Summary.....	126
CHAPTER 8 CONCLUSIONS AND FUTURE WORK	127
8.1 Future Work.....	128
8.1.1 In situ TEM investigation under electric field.....	128
8.1.2 Investigation of mechanical properties of Si-doped boron carbide nanostructures	128
8.1.3 Understanding the effect of higher boron content in boron carbide.....	129
8.1.4 Structural Analysis using Monte Carlo Simulation.....	130
LIST OF REFERENCES	132
APPENDIX.....	144
I. List of Abbreviations.....	144
VITA.....	145

LIST OF TABLES

Table1. Important historical events in the synthesis and development of boron carbide (after Ref. [4]).	7
---	---

LIST OF FIGURES

Fig 1 (A) Atomic structure of boron carbide indicating the various positions of atoms. There are six atoms along the equator of the unit icosahedron, each forming five intraicosahedral bonds and one intericosahedral bond to a terminal atom in the linear chain. There are also six atoms forming three-atom poles on the top and bottom of the icosahedra, which form five intraicosahedral bonds. One of the atoms will be a carbon atom in the case of $B_{11}C$ icosahedral. The atoms in the extreme of the linear chain, either carbon or boron, have a tetrahedral-like coordination to three atoms in three different icosahedra and to the central atom in the chain, and (B) SEM image (a) of a typical icosahedron crystal of boron carbide. The inset shows an illustrating model of an isolated icosahedron corresponding to the real crystal shown in a. (b-d) Icosahedral crystals observed with various orientations along with the 5 fold symmetry of the boron carbide [21, 22].	10
Fig 2 Boron Carbon phase diagram indicating the regime of boron carbide and presence of the other phases including solid solutions of B_4C [4, 25].	11
Fig 3 Graph showing the Vickers hardness (HV) as a function of temperature for various hard materials, including boron carbide; the hardness of B_4C increases with a decrease in temperature and reaches a plateau [41].	14
Fig 4 Raman spectra from (a) the polished (0001) surface and (b) a 100 mN indentation in $B_{4.3}C$ recorded using three different excitation wavelengths. Arrows indicate (a) the 1570 cm^{-1} peak of the pristine surface and (b) the peaks appearing after indentation [46].	16
Fig 5 Impact pressure vs. shear strength of boron carbide indicating the transition from a ceramic to a glass-like behavior. The region marked in green shows the HEL limit of B_4C . Boron carbide is hard and elastic till HEL ($\sim 17\text{-}20\text{ GPa}$) but it dramatically changes above the Hugoniot, leading to a region of limited plasticity [45, 48].	17
Fig 6 HRTEM image showing the evidence of a 2-3 nm amorphous band along the (113) direction that leads to the premature failure in B_4C and b) the corresponding simulated structure containing the collapsed segregated phases of B_{12} icosahedra and carbon along the (113) direction [1, 2].	18

Fig 7 Plan view TEM micrograph of a 100mN Berkovich indent on hot-pressed polycrystalline boron carbide; (b) a magnified image showing the amorphous bands along the (113) and (003) planes; (c-d) HR lattice images corresponding to the boxed area in (a-b); (e) a primarily amorphous region within the Berkovich indent [50]. 20

Fig 8 Diagrams of the four (i) – (iv) steps required to transform $B_{11}C_p(CBC)$ into B_{12} and graphite at 10^{-4} GPa (lower panel) and 16 GPa (upper panel). Only step (iv), the less energetically expensive, is required if the starting carbide has already locally organized as $B_{12}(CCC)$. It can be seen that, at 16 GPa, the $B_{12}(CCC)$ phase has become an unstable point. The thin lines fitting the energy functional are visual aids only [2]. 21

Fig 9 (a) Low-temperature and (b) High-temperature Raman spectra of a- B_4C measured from 83 K to room temperature and room temperature to 873 K [51]. 23

Fig 10 High-pressure Raman spectra of single crystal B_4C loaded in DAC with powdery B_4C as PTM. (a) Raman spectra of B_4C loaded from ambient pressure up to 50 GPa, (b) unloaded from 50 GPa to ~ 1.4 GPa; and (c) Raman spectra of recovered B_4C pressurized to 25.9, 35.8, and 50 GPa. (d) Optical micrograph of the recovered sample pressurized to 50 GPa. Cracks and surface relief reveal that the crystal is loaded under a nonhydrostatic state. The Raman spectra shown in (c) are acquired from the region free of cracks, for example, the marked region in (d) [52]. 23

Fig 11 (a) Visible Raman spectra and (c) UV Raman spectra from unidentented and damaged regions of static and dynamic indetation [53]. 24

Fig 12 (a) Schematic of silicon (Si) doped B_4C and (b) Gibbs free energy of the $B_{11}C_p(CBC)$ and $B_{12}(CCC)$ polytypes as a function of silicon atom concentration. It can be observed that the difference in Gibbs free energy between the stable polytype, $B_{11}C_{(1-y,p)}Si_{(y,p)}(CBC)$ and the most energetically favored minority polytype, $B_{12}(CSi_yC_{1-y}C)$ increase with the silicon content. Hence silicon-containing boron carbide is less affected by disorder than the undoped one [57]. 26

Fig 13 Schematic of deformation mechanism taking place during indentation: (a) dislocation-induced plastic flow, (b) brittle fracture, and (c) ductility induced by a high pressure phase transition into metallic state. 29

Fig 14 Schematic diagram of the nanoindentation experimental setup. 30

Fig 15 Schematic of a Raman microspectrometer. The monochromatic incident beam is redirected through a set of optical components into the microscope objective. The objective is used to illuminate the sample and to collect light scattered on the sample. Inelastically scattered light is then dispersed into a spectrum inside the main spectrometer unit. The computer collects the Raman signal from the charged coupled device (CCD) detector attached to the spectrometer and optical images from the video camera attached to the microscope.	32
Fig 16 Raman spectra of pristine and indented boron carbide by a Ramascope 2000 (Reinshaw, UK). It shows that after nanoindentation, there is evolution different bands ~ 1320 and 1580 cm^{-1} , corresponding to D and G modes in carbon materials.	32
Fig 17 Comparison of (a) normal Raman and (b) SER spectra of tyr-gly molecule [60] shoing the increase in the detection and intensity of the peaks.	34
Fig 18 Schematic diagram of a scanning electron microscopy [63].	36
Fig 19 Schematic of a transmission electron microscope [67]	40
Fig 20 The scattering of an incident electron beam (I) by a crystal lattice. On the other side of the specimen, two kinds of intense beams can be found: the direct beam (T) and the diffracted beam (D). In other directions (e.g. N), no intense electron beam will be detected.	43
Fig 21 Schematic illustrating electron diffraction in TEM.	44
Fig 22 Scanning electron micrographs (SEM) of the samples analyzed in the present work: (a) Powder sample in which the distribution of grain sizes can be recognized. (b) Hot pressed sample from the same powder type reported in panel a, where brighter, presumably more conducting, grains (presumably intergranular graphitic islands) can be recognized. Inset in panel b reports the optical absorption coefficient of the sample, as inferred by spectroscopic ellipsometry data (Jobin-Yvon UVISEL ellipsometer) assuming a semi-infinite medium for the air-sample system. Vertical bars indicate the used Raman excitation energies.	50
Fig 23 Raman active modes in typical boron carbide spectrum are shown. The three Raman vibrations used for our statistical analysis: the icosahedral breathing	

(IBM) mode of boron carbide at $\sim 1075\text{ cm}^{-1}$ and the D and G peaks of graphite and a-C ($1250\text{-}1350\text{ cm}^{-1}$ and $1500\text{-}1600\text{ cm}^{-1}$ respectively) [26, 72, 73]..... 54

Fig 24 (a) Example of B_4C powder spectra at three different excitation wavelengths spanning from near-infrared (785 nm, 1.57 eV) to visible wavelength (532 nm, 2.34 eV). The steady decrease of the low frequency modes (275 cm^{-1} and 325 cm^{-1}) and the reduced sensitivity to the D and G sp^2 carbon modes at increasing excitation energy can be observed. (b) Example of four B_4C powder spectra on different powder grains at constant excitation energy (785 nm, 1.57 eV). 56

Fig 25 (a) Statistical distribution of the $I(\text{G}) / I(\text{D})$ ratio in the 48 of 50 stochastically recorded Raman spectra on powder in which these modes could be detected (b) Statistical distribution of the $I(\text{IBM}) / I(\text{G})$ ratio in the stochastically recorded Raman spectra on powder. It can be seen that in both cases (panel a and b) the distributions are bimodal. (c) correlations between the statistical distributions of $I(\text{IBM}) / I(\text{G})$ and $I(\text{G}) / I(\text{D})$ ratios, revealing two different groups of Raman spectra, “type 1” and “type 2” corresponding to intra- and intergranular graphitic inclusions in the powder. 57

Fig 26 Micro Raman spectrum (a) Comparison of substantially identical 785 nm Raman spectra from powder and hot pressed sample. (b) The similarity in D and G modes is also evident. 59

Fig 27 SPM images of indents on the B_4C hot pressed sample at increasing load: (a) 100 g, (b) 200 g and (c) 300g. 61

Fig 28 Raman Mapping grid on the optical images of the “type b” indentation at 300 mg load used for our considerations (a) before and (b) after dispersion of the gold particles. The grids used for Raman-mapping of the indentation are also evidenced. Each grid has a $2.5\text{ }\mu\text{m}$ step..... 61

Fig 29 Results from bulk and surface-Raman mapping the “type b” indentation at 300 mg load, with the identification of four broadly homogeneous characteristic regions: (a) region where load produced medium-range ordered nanocrystalline graphite (b) region of medium-range disordered and strongly amorphized graphitic islands (c) large cracks where medium-range disordered olefinic $\text{C}=\text{C}$ chains are produced (d) comminuted cracks presenting region of medium-range disordered, strongly amorphized graphitic islands under residual stress..... 63

Fig 30 Red lines: results from SERS mapping the “type 2” indentation at 300 mg load, with comparison with the baseline-corrected bulk Raman spectra reported in Figures 29(a-d) (grey lines). In panels a-b, the stronger amorphization of the surface, leading to broader D and G peaks, can be observed. In panels c-d we can observe the stress release on the surface, leading the SERS G_{σ} peaks to recover their ‘usual’ position below 1600 cm^{-1} 66

Fig 31 Dispersion for the G-mode under residual stress (G_{σ}) as a function of the excitation wavelength for the map point investigated in Figure 29d and 30d. The mode dispersivity ($\sim 0.5\text{ cm}^{-1}/\text{nm}$) coincides with that reported in the literature for the G-mode of diamond-like amorphous carbon. 66

Fig 32 (A) Schematic of the apparatus used for in-situ Raman investigation of boron carbide under electric field. Raman spectra as a function of the electrical field showing the (B) entire frequency range, including the boron carbide modes and (C) detailed plot of the frequency region where the carbon D and G peaks are present and (D) the ratio of $I(D)/I(G)$ vs. applied electric field 74

Fig 33 (A) Sheet conductance of the boron carbide sample as a function of the applied electric field at room temperature. At low fields (below 3000 V/cm), the increase in conductance is attributed to the formation of an amorphous a-C(:B) phase while at higher fields significant sp^2 clustering leads to a substantial increase of the aromatic cluster size. (B) Arrhenius plot of sheet conductance as a function of temperature at three different electric fields. 77

Fig 34 Plot of (A) activation energy and (B) prefactor as a function of the electric field strength. 78

Fig 35 SEM images of the B_4C nanostructures with varying B to C ratio along with diameter distribution of B_4C NWs and nanostructures. Figures a to d correspond to different B to C ratio i.e. a) 1:0.25, b) 1:1, c) 1:4, and d) 1:8 and temperature of $1250\text{ }^{\circ}\text{C}$ (Scale bar $10\text{ }\mu\text{m}$). 87

Fig 36 SEM images showing the effect of temperature on the growth and morphology of nanostructures when the temperature was varied from $1000\text{ }^{\circ}\text{C}$ (during which no growth was observed) to $1250\text{ }^{\circ}\text{C}$. Figure a, b, c and d correspond to a temperature $1150\text{ }^{\circ}\text{C}$ and e, f, g and h to $1250\text{ }^{\circ}\text{C}$. More specifically (a) B:C ratio = 1:0.25 at $1150\text{ }^{\circ}\text{C}$, (b) B:C ratio = 1:1 at $1150\text{ }^{\circ}\text{C}$, (c) B:C ratio = 1:4 at $1150\text{ }^{\circ}\text{C}$, (d) B:C ratio = 1:8 at $1150\text{ }^{\circ}\text{C}$ and (e) B:C ratio = 1:0.25 at $1250\text{ }^{\circ}\text{C}$, (f) B:C ratio = 1:1 at $1250\text{ }^{\circ}\text{C}$, (g) B:C ratio = 1:4 at $1250\text{ }^{\circ}\text{C}$, (h) B:C ratio = 1:8 at $1250\text{ }^{\circ}\text{C}$ 90

Fig 37 TEM images showing morphology, size and presence of catalyst particles (arrows) in different boron carbide nanowires and nanostructures. a) Indicates the presence of different diameters and b) shows an example of a long, straight nanowire along with a diffraction pattern indicating the single crystalline nature. The growth condition for a) and b) B:C ratio = 1:1 at 1150 °C.....	91
Fig 38 SEM images of Si-doped BC NWs at various B to C ratio of 1: a) 0.25, b) 1, c) 4 and d) 8 at 1250°C. The scale bar corresponds to 5 µm.	93
Fig 39 SEM images of Si-doped BC NWs at various growth temperatures: a-d) correspond to 1150 °C and e- h) to 1250 °C. More specifically (a) B:C ratio = 1:0.25 at 1150 °C, (b) B:C ratio = 1:1 at 1150 °C, (c) B:C ratio = 1:4 at 1150°C, (d) B:C ratio = 1:8 at 1150 °C and (e) B:C ratio = 1:0.25 at 1250 °C, (f) B:C ratio = 1:1 at 1250 °C, (g) B:C ratio = 1:4 at 1250 °C, (h) B:C ratio = 1:8 at 1250 °C. The arrows in the inset of figure 39d corresponds to nanowires with a visible catalyst tip.	95
Fig 40 (a) TEM images showing the single crystalline nature and elemental composition of Boron Carbide nanowires. a) TEM image of a single long Si-doped boron carbide nanowire b) HRTEM image along with a FFT pattern confirming boron carbide NWs and c) EDS spectrum (tail and head of NW) indicating the elemental composition. All the images correspond to growth condition with B:C ratio = 1:1 and 2 wt. % Si at 1150 °C.....	97
Fig 41 STEM image and EELS compositional maps of a single Si-doped boron carbide nanowire indicating the presence of catalyst at the top. a) STEM image of the mapped wire, b) a representative EELS spectrum with the characteristic boron and carbon K-edges used in elemental mapping, and c-g) the elemental maps of various elements present in the nanowire, c) Boron (B), d) Carbon (C), e) Nickel (Ni), f) Cobalt (Co) and g) Silicon (Si). Each map was collected over a region of 50 nm by 100 nm with different colors corresponding to different elements.....	98
Fig 42 Thermo-grams comparing the weight loss and weight gain for different temperatures and different B to C ratios in the B ₄ C/Si-doped B ₄ C NWs and bulk boron carbide.	101
Fig 43 Experimental distribution of the nanowire diameters in the various examined growth conditions. With the exception of one point (B/C = 0.25, 1250°C, in the presence of Si) the trends predicted by the model in the text are fulfilled.....	102

Fig 44 Experimental distribution of the nanowire lengths. The length of nanowires grown at $T_1 \approx 1250^\circ\text{C}$ undergoes a non-monotonic behavior as a function of the B/C ratio. 103

Fig 45 (a) Schematic of the boron-rich end of the B-C phase diagram . Areas involving supersaturated liquid are highlighted in blue (C-rich liquid and B_4C crystallites) or red (B-rich liquid and crystallites at variable B_xC composition). (b) Consequently at $T_1 \approx 1250^\circ\text{C}$, the critical catalyst diameter d_c (hence the nanowire diameter $D \sim d_c$), first decreases with B/C ratio and then increases. In contrast, at $T_2 \approx 1150^\circ\text{C}$, the behavior described Figure 45c leads d_c and D to increase with B/C ratio. Dotted lines are regions of the phase diagram where the liquid phase does not exist, but may locally appear due to inhomogeneities in precursors (B and C powders), as described in the text. (c) According to the lever's rule, at $T_1 \approx 1250^\circ\text{C}$, the degree of supersaturation of the catalyst particles first decreases with the B/C ratio (in the region involving carbon-rich liquid) and then increases (in the region involving boron-rich liquid), while (d) At $T_2 \approx 1150^\circ\text{C}$, only B-rich liquid exists, thus supersaturation increases. 106

Fig 46 Schematic of three different mechanisms examined for the incorporation of B and C in the supersaturated liquid catalyst particles: (a) Incorporation from superficial diffusion along the sidewalls of the wire (b) sublimation driving growth and (c) direct dissolution into the droplets from solid precursors. The crude trends of the growth rate (and the nanowire L) in the three cases are shown and (d) since L is proportional to D in our case, we suggest that the growth mainly occurs by direct dissolution of the precursors into the catalyst droplet. 109

Fig 47 (a) Characterization of ultra-long B_4C nanowires. (a) scanning electron microscopy (SEM, FEI XL30 was used at an operating voltage of 5 kV and a working distance of 6mm) and (b), (c) transmission electron microscopy (TEM, Topcon 002, 200 kV) images of typical NWs. The lengths of the NWs ranged from 1 – 5 mm while the diameter varied from 50 – 100 nm. (c) High-resolution TEM imaging reveals the single crystalline nature of the NWs. A fast Fourier transform (FFT, Gatan Image Acquisition and Processing Software: Digital MicrographTM) pattern shown at the bottom inset corresponds to the B_4C or B_{13}C_2 lattice viewed along the [010] zone axis. The atomic resolution image in the top inset of shows the spacing of 0.39 nm, corresponding to the distance between (003) planes and (d) Raman (Renishaw InVia Raman microscope equipped with a 100X objective was used. The excitation source wavelength was 785 nm) spectra of the B_4C NWs. 118

Fig 48 Nanocomposite fabrication and structural properties. (a) typical morphology of nanocomposites (0.025 wt.%) examined using SEM, revealing the

presence of B₄C NWs (indicated by arrows) in the PMMA matrix. Specimens in (b)-(d) were prepared by focused ion beam etching. Images in (b)-(d) are high magnification images of NWs protruding from the polymer matrix. (e) The glass transition (T_g) temperature monitored by differential scanning calorimetry (DSC, TA Instruments Co. Model: 2010). Adding 0.025 wt% of ultra-long B₄C NWs into PMMA increases the T_g by ~ 40 °C of the nanocomposites. 120

Fig 49 Typical SEM images from nanocomposite containing 0.025 wt.% B₄C NWs in PMMA matrix. The NWs are generally covered with the polymer indicating good adhesion with the polymer matrix..... 121

Fig 50 Typical SEM images from nanocomposite containing 0.015 wt.% B₄C NWs in PMMA matrix. The NWs are generally covered with the polymer indicating good adhesion with the polymer matrix..... 121

Fig 51 Thermal, electrical and optical properties of the nanocomposites. (a) Thermal and electrical conductivities of the nanocomposites as a function of filler (B₄C NWs) concentration. b) UV-VIS (Perkin Elmer) spectrum of the transmittance versus wavelength of pure PMMA and free standing composite. The transmittance at 550 nm was found to be approximately 80 – 85 %, slightly less than pure PMMA. The photograph in the inset clearly indicates the transparent nature of the nanocomposite. 124

| CHAPTER 1 | INTRODUCTION

One of the equilibrium compounds in the Boron-Carbon (B-C) system is Boron Carbide (B_4C). Other compounds within this system are regarded as solutions of boron in B_4C or solid solutions with carbon. During the last 50 years, Boron Carbide (B_4C) has been shown to possess outstanding ballistic armor properties because of its high hardness (~ 30 GPa), low density (theoretical density: 2.52 g/cm^3) and high Hugoniot elastic limit (HEL ~ 17 - 20 GPa). In particular, the combination of its low density with its high hardness and Young's modulus (~ 500 GPa) would make boron carbide very attractive for armor applications where weight is critical. Although these properties suggest that boron carbide should withstand high velocity impacts, this has not been observed. One of the primary reasons for failure of boron carbide at significantly lower than expected impact rates and pressures is the absence of residual plastic strength above the HEL.

1.1 Motivation

Recent transmission electron microscopy (TEM) results demonstrate that the failure of B_4C is commensurate with the segregation of boron icosahedra embedded in 2–3 nm wide amorphous bands along the (113) lattice direction, in good agreement with our recent theoretical results [1, 2]. In our work, we used density functional theory (DFT) calculations used to determine the root cause of failure of boron carbide just above the HEL. A range of B_4C polytypes were found to be stable at room temperature and pressure. The energetic barrier for failure was by far the lowest for the $B_{12}(CCC)$ polytype, requiring only 7 GPa $\approx P(HEL)$ for collapse. The failure of the $B_{12}(CCC)$ minority polytype results in the formation of B_{12} icosahedras which are embedded in 2-3 nm amorphous carbon bands.

Our calculations suggest a route to achieve suppression of the $B_{12}(CCC)$ polytype without significantly affecting the elastic constants or the density of boron carbide via low concentration silicon doping. Recently, our collaborators have shown that Si-doped amorphous boron carbide films were much harder in comparison to undoped films [3]. The HEL of Si-containing boron carbide is predicted to be above 40 GPa, one of the highest values ever found in solids. Suppression of $B_{12}(CCC)$ via Si doping has implications towards the development of boron carbide as a protective, impact resistant material and promises to greatly improve its properties for protection against high velocity impact.

1.2 Chapter Outline

Chapter 1 describes the motivation and the chapter outline, while the Background and Literature Review in Chapter 2 details needs and salient research currently pursued on Boron Carbide systems. Chapter 3 describes the experimental and characterization tools employed to carry out the research described in this thesis.

In order to verify the weak-link $[B_{12}(CCC)]$ theory for the failure of B_4C , the structural changes in boron carbide were evaluated and monitored by using a two pronged approach: Static (Indentation combined with Raman Spectroscopy) and Dynamic (*In situ* Electrical Field Raman Spectroscopy) studies.

Static (Chapter-4): Static/ex-situ impact studies were used to characterize the changes in structure and phase transformations by using indentation and Raman Spectroscopy. It has been previously demonstrated that ex-situ Raman measurements can be used to characterize local graphitization and phase changes induced during nanoindentation (discussed in the chapter). It was shown that graphitization does not occur until a pressure of ~ 40 GPa, twice the value of B_4C failure under impact. In addition, boron rich B_4C samples were evaluated to see the extent of graphitization, or sp^2 clustering, as they have been shown to possess superior properties.

Dynamic (Chapter-5): Real time characterization of the graphitization process could provide valuable insights into why B_4C fails prematurely in dynamic tests. The application of relatively low electric fields can be used to show the *in situ* graphitization in B_4C . By applying pulses of increasing voltage and simultaneously monitoring phase

changes with Raman spectroscopy, it is possible to observe not only the onset but also the degree of graphitization in real time. Furthermore, through electrical measurements as a function of temperature in conjunction with Raman spectroscopy, we can determine a critical electrical field above which the graphitization leads to the collapse of the B_4C structure. In addition, this tool provides a viable method to characterize B_4C non-destructively.

In chapter 6, a route to achieve suppression of the $B_{12}(CCC)$ polytype without significantly affecting the elastic constants is via low concentration Silicon (Si) doping of B_4C is presented. A novel technique was developed to actually synthesize Si doped boron carbide at nanoscale. Nanowires of boron carbide and Si doped boron carbide were produced by Solid Liquid Solid (SLS) growth mechanism. The diameter of the nanostructures varied widely, ranging from 5 nm to 2 μm . The lengths of the nanowires were found to vary from several micrometers up to a few millimeters (ultra long). By using these ultra long nanowires, thermally conducting, transparent nanocomposites were fabricated (Chapter-7) from direct solution blending of ultra-long boron carbide (B_4C) nanowires (NWs) with poly(methyl methacrylate) (PMMA). Introduction of just 0.025 wt% of B_4C NWs into PMMA leads to an almost one order of magnitude increase in the thermal conductivity and diffusivity (from 0.176 W/m-K and $1.26 \times 10^{-3} \text{ cm}^2/\text{sec}$, respectively, for PMMA to 1.11 W/mK and $8.538 \times 10^{-3} \text{ cm}^2/\text{sec}$, respectively, for the nanocomposite) along with a substantial increase (by $\sim 40^\circ\text{C}$) in the glass transition temperature. The exceptional low loading of B_4C NWs into PMMA at which these properties are achieved in comparison to other filler materials is attributed to the very high aspect ratio (10^4 – 10^5) of the ultra-long NWs.

In chapter 8, the conclusions of this work are discussed and some ideas about the future direction of the current research are presented. A suggestion of how these nanostructures (nanowires, nanorods, nanobelts etc.) of Si-doped boron carbide need to be consolidated to evaluate their mechanical properties is presented, in the process, validating the hypothesis that Si-doped boron carbide can potentially lead to an improvement in the properties of boron carbide.

| CHAPTER 2 | BACKGROUND AND LITERATURE REVIEW

Boron Carbide is one of the hardest materials of our era [4]. It has manifold applications (cutting tools, abrasives, coatings etc.), which we can rarely see round us, but if we look closely, the versatile material serves a bigger purpose than is expected (neutron absorber, electronics, armor etc.). Boron Carbide, or B_4C , has not been sufficiently studied by researchers to date. However, it invokes a lot of curiosity in the scientific world due to the various complexities present in its structure. In the last 30 years, several papers have been written that mentioned boron carbide and its catastrophic failure and its relation to some of its polytypes. However, there are still many gaps in understanding the phase transformation mechanisms and metastable phases formed during contact loading and high velocity experiments which provide some insights into its premature catastrophic failure. In the following sections, the most salient studies on boron carbide, its properties and applications, and experimental studies on pressure induced phase transformations and developing B_4C nanostructures, are reviewed.

2.1 History of Boron Carbide

Boron carbide belongs to the important group of nonmetallic hard materials, which includes alumina, silicon carbide and diamond [4, 5]. It is the third hardest material, next only to diamond and cubic boron nitride. It was allegedly discovered more than a century ago, in 1858. Although it was synthesized and identified in 1883 (Joly *et al.*), the formula of B_4C was not assigned until 1934 [6]. Various important events in the development and synthesis of boron carbide are shown in Table 1. Today, a homogeneity range from $B_{4.3}C$ to $B_{10.4}C$ has been established. The composition of boron carbide is usually close to a boron:carbon stoichiometry of 4:1, with the stoichiometric limit on the high-carbon side of the phase diagram [4].

Table 1. Important historical events in the synthesis and development of boron carbide (after Ref. [4]).

Year	Boron Carbide Advances	Source
1883 and 1894	First synthesis of B_3C and B_6C	Jolly and Moissan
1934	The “stoichiometric formula B_4C ” was assigned	Rigdway
1935–1940	Abrasive grit production	Norton Comp., USA ESK, Germany
1952	Hot Pressed B_4C , TETRABO nozzles and n-absorbers produced	Norton Comp., USA ESK, Germany
1956	$B_{12}C_2$ and $B_{12}C_3$ identified	Samsonov
1961	One compound with a large homogeneity range $B_{11.5}C - B_{4.0}C$	Elliot <i>et al.</i>
1977	Pressure-less sintered submicron powder	ESK, Germany
1980	HIP- B_4C , posted Hipped pore-free	ESK, Germany
1990	$B_{4.3}C$ instead of $B_{4.0}C$ is the carbon rich limit of homogeneity range	Schwetz
1993	B_4C-TiB_2 alloys	ESK, Germany
2002	Structural Changes in B_4C determined by Raman Spectroscopy	Dominich <i>et al.</i>
2003	Evidence of shock-induced localized amorphization in B_4C	Chen <i>et al.</i>

2.2 Synthesis Methods

One of the oldest methods to make B₄C is by using an arc furnace process. The electric arc furnace process for making boron carbide was patented by Schroll *et al.* [7] in 1939, wherein the mixture of boric acid and petroleum coke is melted in an arc furnace followed by crushing the resultant product and mixing it with substantially the same quantity of boric acid and remelting the mixture a second time. The design and operation of the electric arc furnace for large scale production of boron carbide has been explained by Scott [8]. In the arc furnace process, the temperatures are generally very high (~2400 °C) due to localised electric arcs, which are responsible for heavy loss of boron by evaporation of its oxides. Moreover, the product obtained is chunks of melted boron carbide, which needs subsequent laborious crushing and grinding operations.

Boron Carbide can also be synthesized by a number of reduction methods such as reduction of boron anhydride (or acid) with carbon [9] and reduction of boron anhydride with magnesium in the presence of carbon black [10]. The most typical manufacturing method uses boric acid and graphite; after thermal conversion of boric acid to boron oxide, boron carbide is formed via the reaction [11]:



(where l, g, s stand for liquid, gaseous and solid)

The process is strongly endothermic (1812 kJ/mol), and is usually carried out at 1500 – 2500 °C in an electric furnace [12]. Either arc furnaces or resistance furnaces, analogous to Acheson furnaces for SiC, are used for the synthesis.

Although the traditional methods are still used in industrial production of boron carbide, recently, new routes to synthesize boron carbide have resulted in better yield. A H_2 -Ar plasma using a BCl_3 - CH_4 - H_2 mixture produces boron carbide powders in excellent yield, with a wide stoichiometry range (B/C:15.8-3.9) and a fine spherical granularity (20-30 nm) [13, 14]. Ultrafine (34 nm particle size) B_4C powders are also prepared by the CO_2 laser-driven pyrolysis of the same BCl_3 - CH_4 -(C_2H_4)- H_2 mixture. In addition, thin films and coatings of B_4C can also be prepared and deposited on a variety of substrates by chemical vapor deposition (CVD) [15-17], plasma enhanced chemical vapor deposition (PECVD) [18], magnetron sputtering [19] and microwave synthesis [20].

2.3 Boron Carbide: Structure and Defects

Boron carbide has an unusual structure that differs from that of other metal carbides. Its structure is related to α -rhombohedral boron (space group $R_{\bar{3}m}$), where the boron icosahedra are linked directly and as a part of a linear three-atom chain in the center of the rhombohedron and on the principle body diagonal of the rhombohedron oriented along the three-fold axis, as shown in Figure 1. Carbon atoms are placed in the three-atom chain (B-C-C, B-C-B or C-B-C etc.) and in the icosahedra, as shown in Figure 1a [21, 22]. The structure can also be described in terms of a hexagonal lattice based on a non-primitive unit cell, in which case the (0001) axis of the hexagonal lattice corresponds to the (111) rhombohedral direction, which is along the three-atom chain axis [21, 23, 24].

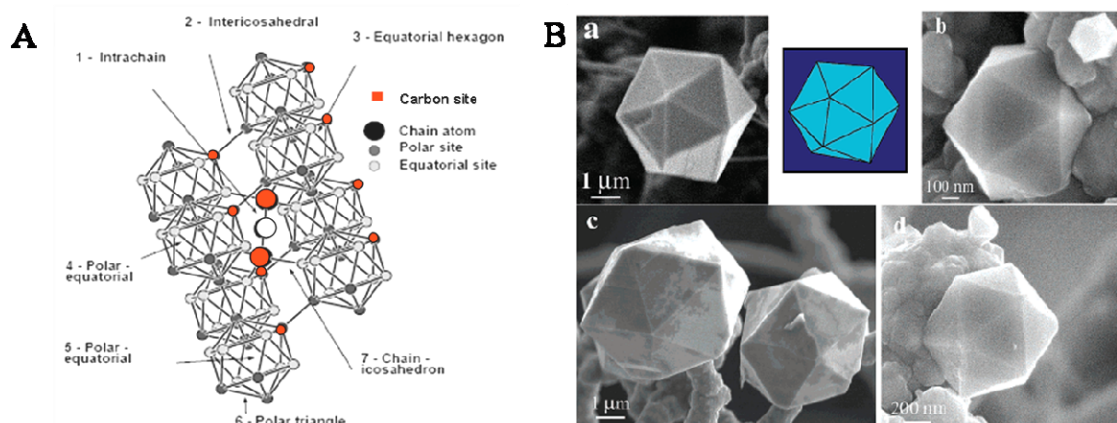


Figure 1. (A) Atomic structure of boron carbide indicating the various positions of atoms. There are six atoms along the equator of the unit icosahedron, each forming five intraicosahedral bonds and one intericosahedral bond to a terminal atom in the linear chain. There are also six atoms forming three-atom poles on the top and bottom of the icosahedra, which form five intraicosahedral bonds. One of the atoms will be a carbon atom in the case of $B_{11}C$ icosahedron. The atoms in the extreme of the linear chain, either carbon or boron, have a tetrahedral-like coordination to three atoms in three different icosahedra and to the central atom in the chain, and (B) SEM image (a) of a typical icosahedron crystal of boron carbide. The inset shows an illustrating model of an isolated icosahedron corresponding to the real crystal shown in a. (b-d) Icosahedral crystals observed with various orientations along with the 5 fold symmetry of the boron carbide [21, 22].

Furthermore, boron carbide can also be considered as a prototype of the interstitial compounds of rhombohedral boron, which include $B_{12}C$, $B_{12}C_2Al$, $B_{12}S$, $B_{12}O_2$, $B_{12}As_2$, $B_{12}P_2$, and $B_{3-4}Si$. The crystal structure of these materials consists of icosahedra that occupy the corners of the rhombohedron, and a chain of atoms that runs along the c-axis of the rhombohedron. For the most part, boron atoms occupy the points of the icosahedra. The second constituent C, Al, O in general occurs on the chain. The rigid framework of polyatomic units of closely bonded atoms is reflected in the refractory nature and great hardness [9].

The bonding of boron carbide is intriguing; its structure consists of B_{12} icosahedra with carbon/boron chains linking them together (Figure 1). B_{12} icosahedra are also linked to other adjacent icosahedra. Therefore, using a tight bonding description, there are four

important bond types in boron carbide. The first type is the highly delocalized intra-icosahedron sp^2 bonds. The second is the inter-icosahedron bond, consisting of boron p (or sp hybrids) orbitals, forming presumably a π bond. The third type exists in the chain of $C=B-C$ as a possible double resonant bond with π characteristic. The fourth type is the bond between carbon in the chain and the boron in the icosahedra at the so-called equatorial positions. The incorporation of various dopants can dramatically affect the bonding and, therefore, impact the physical properties of the material.

Boron carbide is a solid solution with a reported homogeneity range of 8.8 to 20 mol% C, which corresponds to $B_{10.4}C$ to $B_{4.3}C$ respectively. It melts congruently at 2490°C (13.3 mol% C), and forms a eutectic with carbon at $2375\text{--}2400^\circ\text{C}$ at a composition of 29 mol% C, as shown in Figure 2 [4, 25].

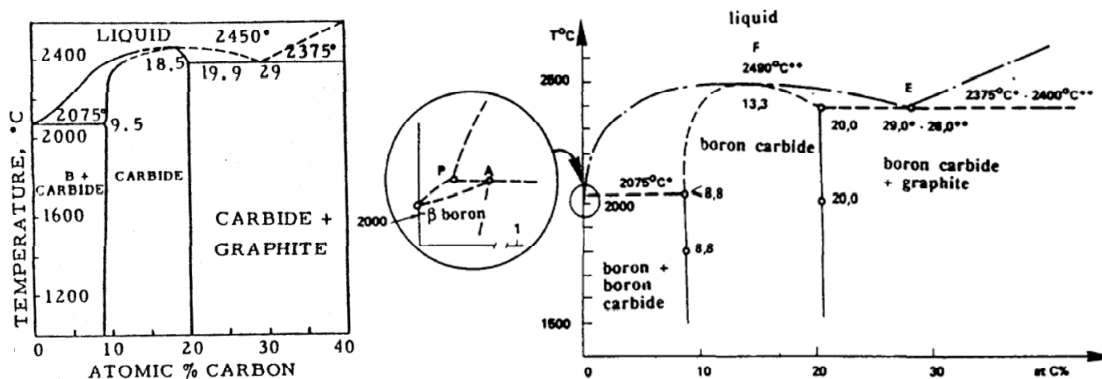


Figure 2. Boron Carbon phase diagram indicating the regime of boron carbide and presence of the other phases including solid solutions of B_4C [4, 25].

As proposed by Emin *et al.* [26], for stoichiometric B_4C , the icosahedra are $B_{11}C$ and the chains are $C-B-C$. As the boron content is initially increased, the carbons in the icosahedra are retained, while one of the carbons in each chain is replaced by boron. For compositions richer in boron than 13.3 mol% C ($B_{13}C_2$), some of the $B_{11}C$ icosahedra are

then replaced by B_{12} icosahedra, while the chains remain C-B-B. The volume of the unit cell decreases linearly with increasing carbon content. Correspondingly, the theoretical density increases linearly with increasing carbon content, extending from 2.465 for $B_{10.4}C$ to 2.52 for $B_{4.3}C$. More recent work by Kwei *et al.* [27] shows that in the C-B-C chain, the central boron atom is relatively loosely held and these locations can form vacancies. The formation of vacancies along the 3-atom chain with boron substitution decreases the thermal conductivity, as phonon transport increasingly resembles that of an amorphous material [28]. The increasing concentration of atomic defects has been attributed to weakly bound electrons, which explains the increasing electrical conductivity with increasing boron content (with a break at 13.3 mol% C). Also, with the change in the composition, there is a prominent effect on mechanical properties. Aselage *et al.* [29] found a significant drop in elastic modulus when the carbon concentration fell below the 13.3% C point, reflecting a change in stiffness of the most compressible structural unit, the icosahedra (i.e. when $B_{11}C$ to B_{12}).

2.4 Properties and Applications

Boron carbide has become one of the most interesting materials currently available, with a hardness value lagging behind only to diamond and cubic boron nitride. Depending on its structure, B_4C is theoretically transparent while retaining its high hardness. B_4C is a high neutron absorber, a thermoelectric material and is also used in electronic applications. But of particular interest are its high strength and low density, which render it ideal for armor applications. Properties of B_4C , and their different potential applications (such as in electronic devices, body armor and vehicle armor) will be discussed here.

2.4.1 Chemical Stability

Boron carbide is one of the most stable compounds, with low standard enthalpy of formation (-38.9 to -71.5 kJ/mol). Boron carbide is not attacked by cold chemical reagents and reacts with metal oxides only at elevated temperatures to yield carbon monoxide and metal borides. Oxidation of B_4C in oxygen and moisture results in the formation of a surface layer of species like B_2O_3 , HBO_3 or H_3BO_3 . Oxidation starts at 600 °C and results in the formation of a thin transparent B_2O_3 film, which cracks after cooling. Further, the oxidation process up to 1200 °C is limited by the diffusion of reagents through the oxide layer [30-32]. Oxidation of B_4C in air will be discussed in detail in the section of boron carbide nanostructures.

Boron carbide can be oxidized by hot oxidizing acids (HNO_3 , H_2SO_4 , $HClO_4$, etc.) and fused salts [33]. B_4C reacts with chlorine at 600 °C and bromine at 800 °C to give boron trihalides; being activated by halides, B_4C is used for the boronizing of steels and alloys [34]. Chlorination of B_4C is also used to produce a high surface area carbon called carbide-derived carbon (CDC) which has potential applications in molecular sieves, gas storage, catalyses, absorbents, battery electrodes, supercapacitors, water/air filters and medical devices [35, 36].

2.4.2 Hardness and Density

The density of boron carbide increases linearly with carbon content within the homogeneity range in the phase diagram. The density measured for $B_{4.3}C$ is 2.52 g/cm³; $B_{13}C_2$, 2.488 g/cm³ and $B_{10.4}C$ is 2.465 g/cm³ [37].

Boron carbide is among the hardest materials (diamond and cubic BN), with a Vickers hardness varying from 25-40 GPa. The hardness (Vickers) of B_4C as function of temperature is shown in Figure 3. The influence of carbon content on hardness of B_4C content is debatable. Allen *et al.* [38] found an increase in the hardness with C content, whereas Schwetz *et al.* [39] did not find any dependence on C content. In addition to its high hardness and low density, B_4C has a high melting point (2450°C), a high elastic modulus (450 GPa) and a high flexural strength (350-500 MPa), which makes it ideal as a grinding medium for hard materials, a lightweight ceramic armor, and a wear-resistant material for sandblasting nozzles [9, 40].

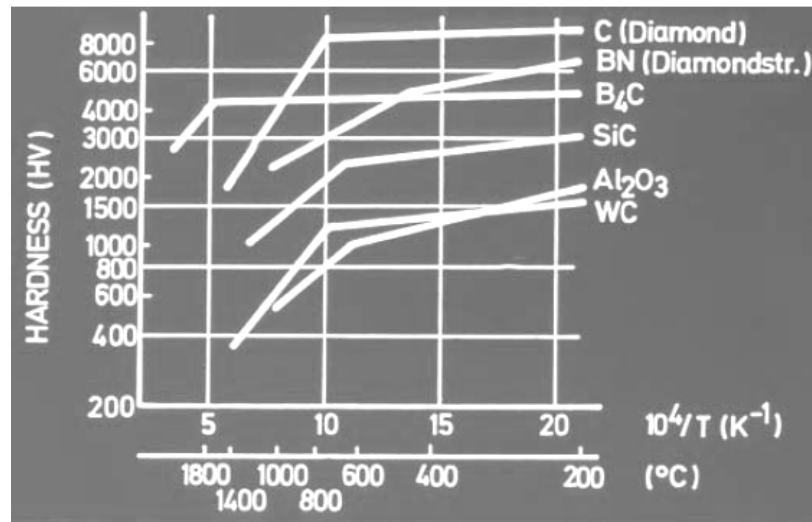


Figure 3. Graph showing the Vickers hardness (HV) as a function of temperature for various hard materials, including boron carbide; the hardness of B_4C increases with a decrease in temperature and reaches a plateau [41].

2.4.3 Limitations of Boron Carbide

The main limitation in boron carbide is its high failure rate above its HEL. This anomalous and poorly understood glasslike behavior in boron carbide has been the subject of research since its discovery over 75 years ago. It presents an enormous

problem when using B_4C in armor applications, where failure of the material could become catastrophic, and serves as the main reason for the lack of use of boron carbide in high impact applications.

Several authors have given different explanations for the anomalous behavior of B_4C . Bourne witnessed the mechanical response of B_4C and found that it was similar to that of amorphous glass [42]. It has also been speculated that the anomalous behavior might be the result of the propagation of cracks, cleavage and melting zones induced by impact [43]. Models of ballistic performance of B_4C were developed to predict this behavior above the critical impact pressure, but most of them have not been experimentally corroborated and are unreliable [44].

In order to understand and identify the root cause for the catastrophic failure of B_4C , studies were also conducted to identify if there is a possibility of a high-pressure phase transformation [45]. Domnich *et al.* conducted nanoindentation experiments combined with Raman spectroscopy that provided evidence of incompletely characterized phase transitions or localized graphitization [46]. They indented oriented single crystals of boron carbide and analysed the Raman spectra of the samples (Figure 4). The spectra obtained before indentation show a series of Raman bands extending from 200 to 1200 cm^{-1} and are generally in good agreement with the spectra recorded in the literature, as shown in Figure 4a. Postindentation characterization of samples revealed the most dramatic changes. Figure 4b shows the appearance of high frequency bands, the most intense of which is at 1330 cm^{-1} and weaker but still prominent are the bands at 1520 and 1810 cm^{-1} , with the latter frequency well above any band observed in boron carbide or any related compound. The appearance of these bands were speculated to be

realized to phase transformation or result of different forms of carbon which tend to give rise to peaks at 1330 and 1520 cm^{-1} , however, the exact mechanism responsible for the observed changes in the Raman spectra of boron carbide after indentation was not identified [46].

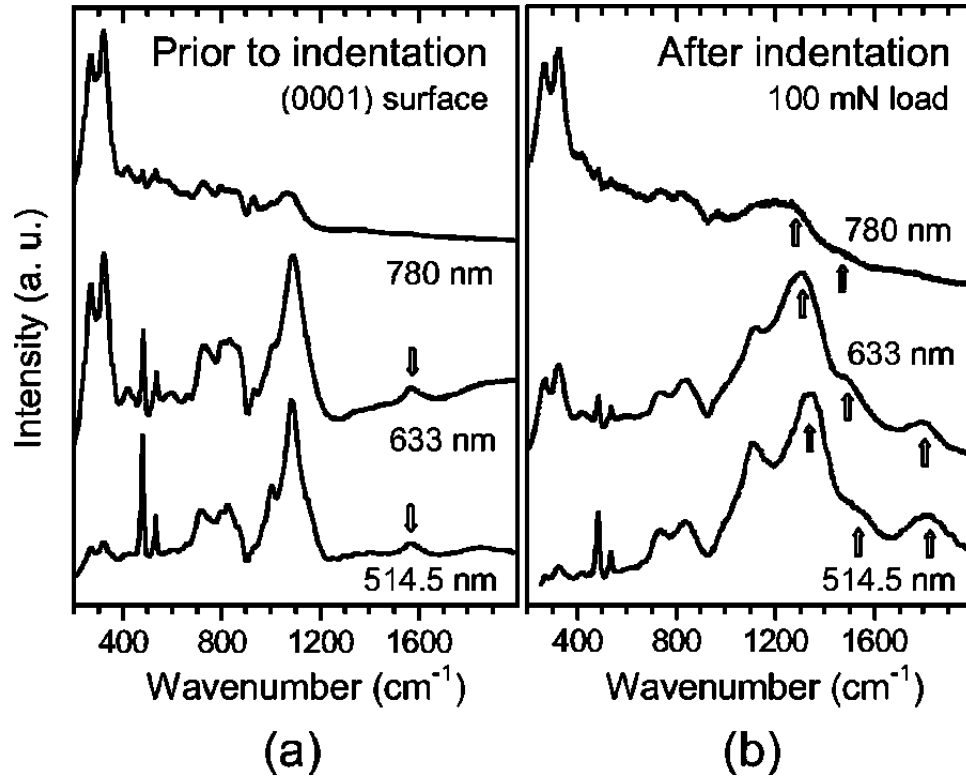


Figure 4. Raman spectra from (a) the polished (0001) surface and (b) a 100 mN indentation in $\text{B}_{4.3}\text{C}$ recorded using three different excitation wavelengths. Arrows indicate (a) the 1570 cm^{-1} peak of the pristine surface and (b) the peaks appearing after indentation [46].

In contrast, Vogler *et al.* [47] demonstrated that the collapse at 20–23 GPa cannot be attributed to phase transformations, which occur only above 40 GPa. Instead, Vogler proposed that a phase transition explaining the failure at the HEL must occur [44] at pressures P greater than or equal to $P(\text{HEL})$ of ~ 7.81 GPa, corresponding to the pressure on the hydrostatic stress-strain curve at the Hugoniot conditions for HEL ~ 17 –20 GPa.

The failure of B_4C has also been attributed to its low density, its low fracture toughness, or the activation of an unidentified damage mechanism at high impact rates and pressures. The latter explanation is supported by the fact that an abrupt drop in the shear strength has been measured at impact pressures of 20 to 23 GPa in impact experiments, as shown in Figure 5 [45-48]. This drop in strength has been related to a change in the fragmentation characteristics of B_4C , but a microscopic description of the damage mechanism that leads to this marked reduction in properties is still lacking.

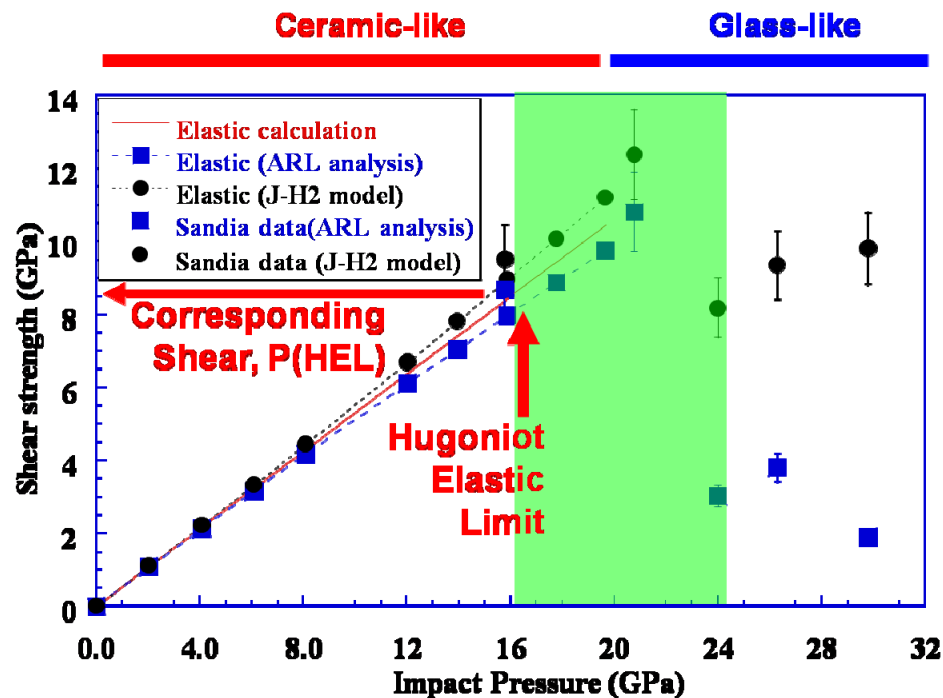


Figure 5. Impact pressure vs. shear strength of boron carbide indicating the transition from a ceramic to a glass-like behavior. The region marked in green shows the HEL limit of B_4C . Boron carbide is hard and elastic till HEL (~17-20 GPa) but it dramatically changes above the Hugoniot, leading to a region of limited plasticity [45, 48].

Transmission electron microscopy results by Chen *et al.* demonstrated that the failure of B_4C is commensurate with the segregation of boron icosahedra embedded in 2–3 nm wide amorphous carbon bands along the (113) lattice direction [1], which is in good

agreement with our group's recent theoretical results (Figure 6) [2]. Chen, McCauley and Hemker used the B_4C fragments which were obtained from a study in which armor-piercing projectiles with velocities ranging from 750 to 1000 m/s were used to evaluate the impact resistance of hot-pressed B_4C -composite laminates [49]. The extreme conditions associated with shock compression produced a complex loading state in both space and time, but the impact pressure in these experiments was estimated to vary from 19 to 25 GPa. The experimental results observed in this study pointed to the onset of localized shock amorphization as a potential high-rate mode of deformation; however, the characterization and composition of these amorphous bands were not addressed.

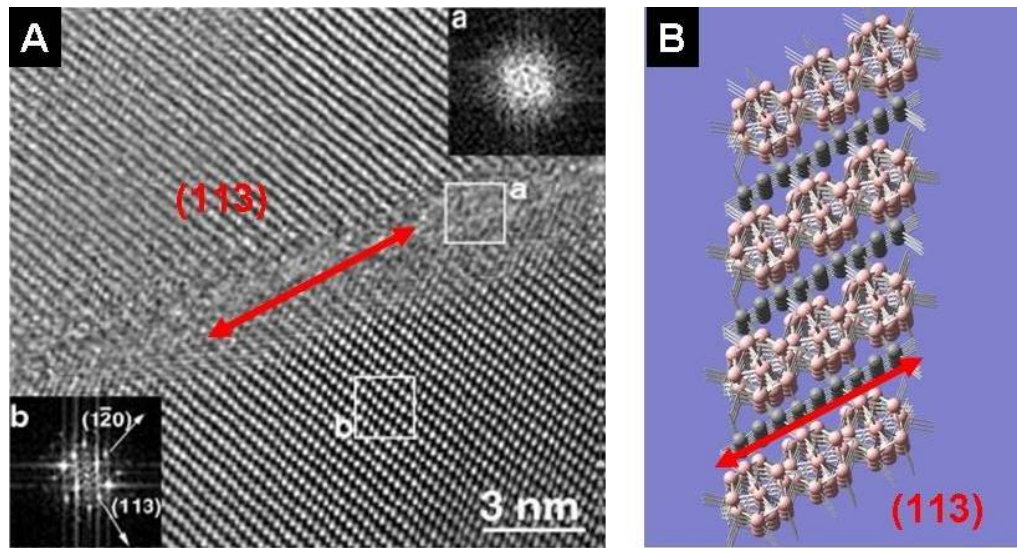


Figure 6. HRTEM image showing the evidence of a 2-3 nm amorphous band along the (113) direction that leads to the premature failure in B_4C and b) the corresponding simulated structure containing the collapsed segregated phases of B_{12} icosahedra and carbon along the (113) direction [1, 2].

Similar amorphous bands were also observed by Ge *et al.* upon indentation (Figure 7). The plan-view investigation of boron carbide revealed the presence of these

amorphous narrow bands and local amorphous region produced during the process of nanoindentation [50].

In our case, density functional theory calculations were used to determine the root cause of failure of boron carbide just above the HEL. A range of B_4C polytypes were found to be stable at room temperature and pressure and it was deduced that the energetic barrier for failure was by far the lowest for the $B_{12}(CCC)$ polytype, requiring only 7 GPa $\approx P(HEL)$ for collapse (Figure 8). The failure of the weak link of $B_{12}(CCC)$ leads to the failure of boron carbide, although the collapsed B_4C maintains and preserves the stoichiometry of the initial material [2].

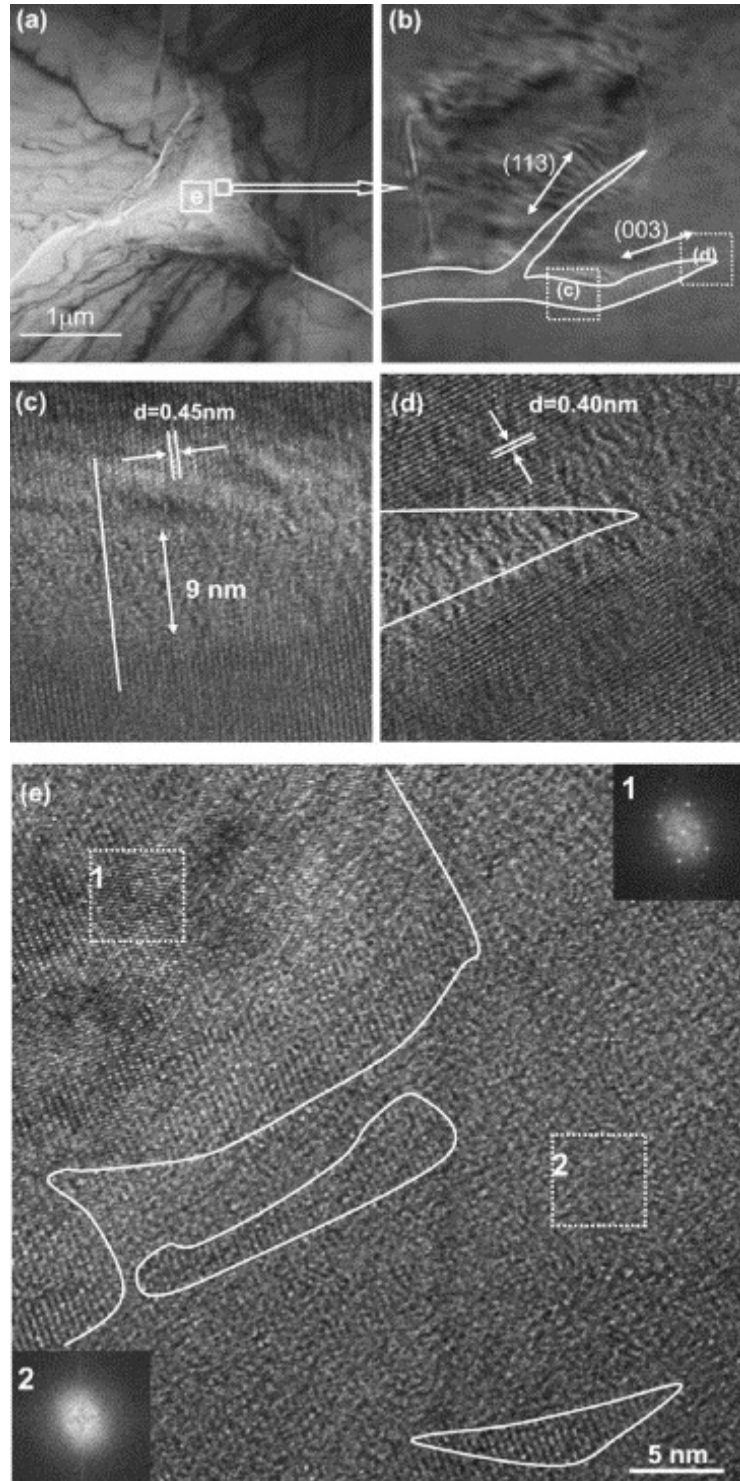


Figure 7. Plan view TEM micrograph of a 100mN Berkovich indent on hot-pressed polycrystalline boron carbide; (b) a magnified image showing the amorphous bands along the (113) and (003) planes; (c-d) HR lattice images corresponding to the boxed area in (a-b); (e) a primarily amorphous region within the Berkovich indent [50].

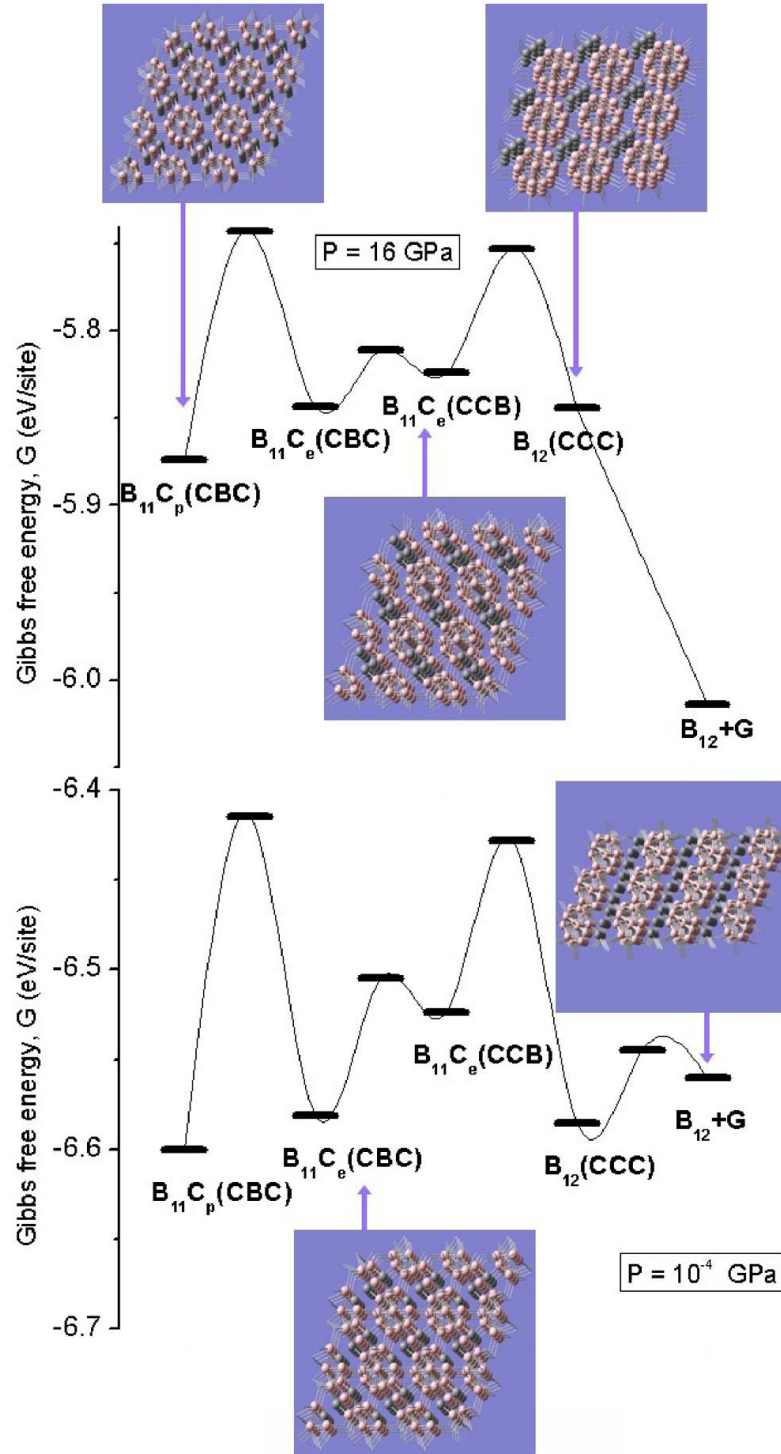


Figure 8. Diagrams of the four (i) – (iv) steps required to transform $B_{11}C_p(CBC)$ into B_{12} and graphite at 10^{-4} GPa (lower panel) and 16 GPa (upper panel). Only step (iv), the less energetically expensive, is required if the starting carbide has already locally organized as $B_{12}(CCC)$. It can be seen that, at 16 GPa, the $B_{12}(CCC)$ phase has become an unstable point. The thin lines fitting the energy functional are visual aids only [2].

After the experimental evidence of the formation of amorphous bands as the possible failure of boron carbide, several authors conducted further studies to understand these phenomena. Chen *et al.* used indented samples of a (223) single crystal boron carbide and sealed them in a heating/cooling stage to carry out temperature-dependent (83 to 873 K) Raman spectroscopy and understand the origin of amorphization in boron carbide. Their studies indicated the failure of the amorphization of B₄C may be mainly accomplished through the structural change of C–B–C chains; nevertheless, the origin of the peak at 1810 cm⁻¹ was not discussed. The Raman spectra from the low and high temperature experiments are shown in Figure 9 [51].

More recently, Yan *et al.* showed depressurization amorphization of (223) single-crystal B₄C investigated by *in situ* high-pressure Raman spectroscopy. By using a high-pressure diamond anvil cell (DAC) and pressure transmitting media (PTM) experiments, they were able to provide unique insights on the phase transition. It was found that localized amorphization of B₄C takes place during unloading from high pressures, and nonhydrostatic stresses play a critical role in the high-pressure phase transition. Their studies indicated that amorphization of B₄C in the form of nanosized bands takes place during unloading from high pressures, and nonhydrostatic stresses play a critical role in the high-pressure amorphization (Figure 10) [52].

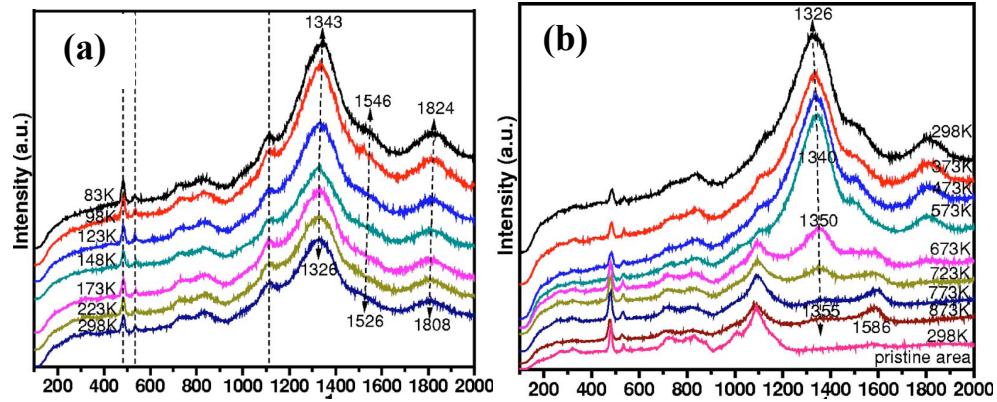


Figure 9. (a) Low-temperature and (b) High-temperature Raman spectra of α - B_4C measured from 83 K to room temperature and room temperature to 873 K [51].

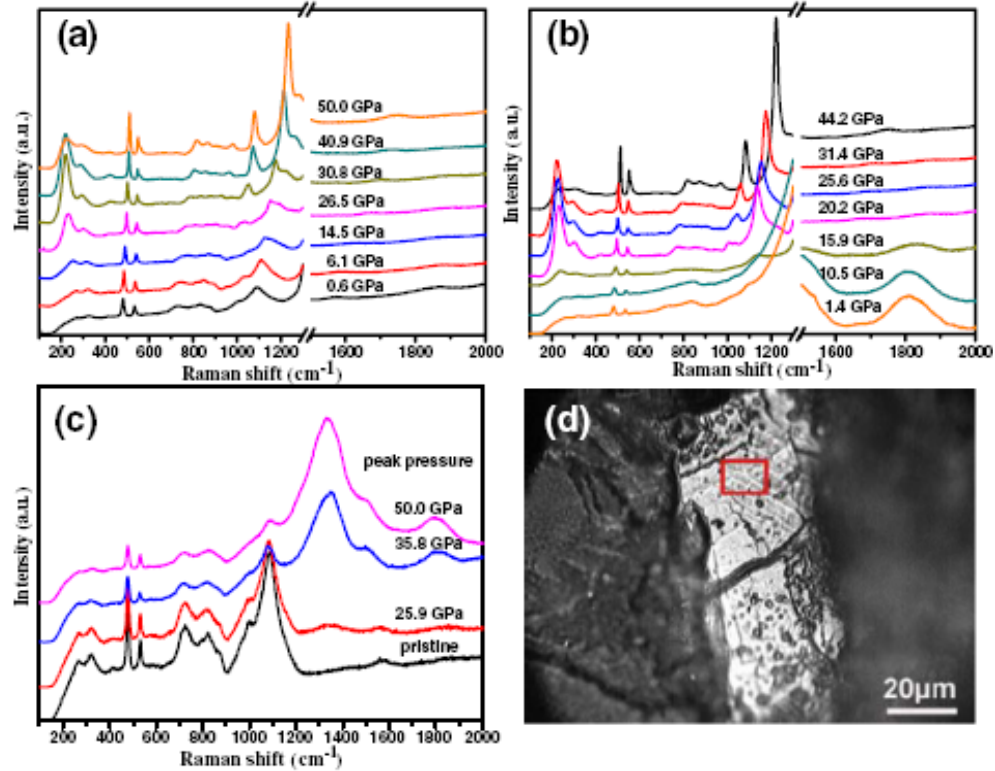


Figure 10. High-pressure Raman spectra of single crystal B_4C loaded in DAC with powdery B_4C as PTM. (a) Raman spectra of B_4C loaded from ambient pressure up to 50 GPa, (b) unloaded from 50 GPa to ~ 1.4 GPa; and (c) Raman spectra of recovered B_4C pressurized to 25.9, 35.8, and 50 GPa. (d) Optical micrograph of the recovered sample pressurized to 50 GPa. Cracks and surface relief reveal that the crystal is loaded under a nonhydrostatic state. The Raman spectra shown in (c) are acquired from the region free of cracks, for example, the marked region in (d) [52].

In a separate study, Ghosh *et al.* utilized higher strain rates in their dynamic indentation experiments to show the drastic transformations occurring in B_4C . They compared their results with static indentation using multi-wavelength Raman and photoluminescence studies. It was shown that the failure of B_4C is due to the collapse of $B_{11}C$ icosahedron which results in reorganization of the B and C atoms into $a-B_{12}$ cluster and sp^2 C clusters. The authors also found that the level of amorphization or structural disorder is higher when induced by dynamic indentation in comparison to static indentation, as shown in Figure 11 [53].

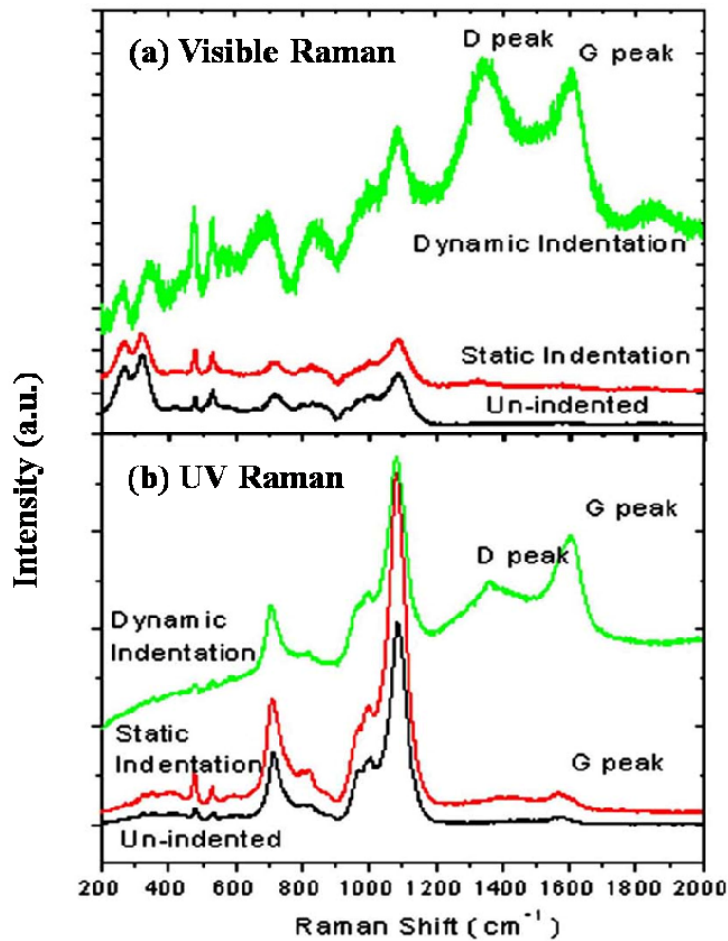


Figure 11. (a) Visible Raman spectra and (c) UV Raman spectra from unidented and damaged regions of static and dynamic indetation [53].

2.4.4 Doping in Boron Carbide

Identifying the root cause of dynamic failure in boron carbide opens up the possibility of tailoring its properties through careful reduction of disorder during synthesis. However, thermal disorder is unavoidable during hot pressing of boron carbide. Therefore, in order to provide an alternative solution for improved impact performance of boron carbide, we have studied the effects of doping. Previously, Schmechel *et al.* studied the use of Al as a dopant in B_4C to improve electric properties [54], Wood *et al.* explored the use of Mg as dopant in B_9C to improve thermoelectric properties [55], while Cai *et al.* showed the feasibility of doping B_4C with Si also to improve thermoelectric properties and energy conversion [56]. Of these, Si is most attractive due to its similar atomic size and properties to B; in fact, adding Si has the same effect as increasing the B ratio in boron carbide. However, the use of Si as a dopant is plagued by the formation of SiC, as it is difficult to avoid by using conventional ceramic processing methods. There is a possible solid state synthesis route with low concentration of Si doping, through nanotechnology, which can eliminate failure phenomenon and pave the way for better armor and ceramic bodies of boron carbide, as is discussed in this work.

The Gibbs free energy of the $B_{11}C_p(CBC)$ and $B_{12}(CCC)$ polytypes as a function of substitutional Si doping is shown in Figure 12. It can be observed that the difference in Gibbs free energy between the stable polytype, $B_{11}C_{(1-y,p)}Si_{(y,p)}(CBC)$, and the most energetically favored minority polytype, $B_{12}(CSi_yC_{(1-y)}C)$, strongly increases by a factor of 15, from $\Delta G = 0.015$ eV at 0 at.% Si to $\Delta G = 0.23$ eV at 6.7 at.% Si. Hence, in the latter case, the concentration of the minority polytype decreases by $\exp(-15) \approx 3 \cdot 10^{-7}$

times in the presence of Si. Thus the $B_{12}(\text{CCC})$ polytype, leading to the premature failure in boron carbide, can be practically eliminated via incorporation of Si. In contrast, the force on the atoms and their derivatives only experience negligible variations, indicating that the elastic constants do not experience large modifications at sufficiently low Si doping. Therefore, experimental realization of Si-containing boron carbide could lead to the development of a material with a HEL exceeding 40 GPa. This presents exciting possibilities for protection against high energy impacts, for instance as a blast shield against high velocity threats or as ballistic armor in military applications or for increased protection when vehicles collide [57].

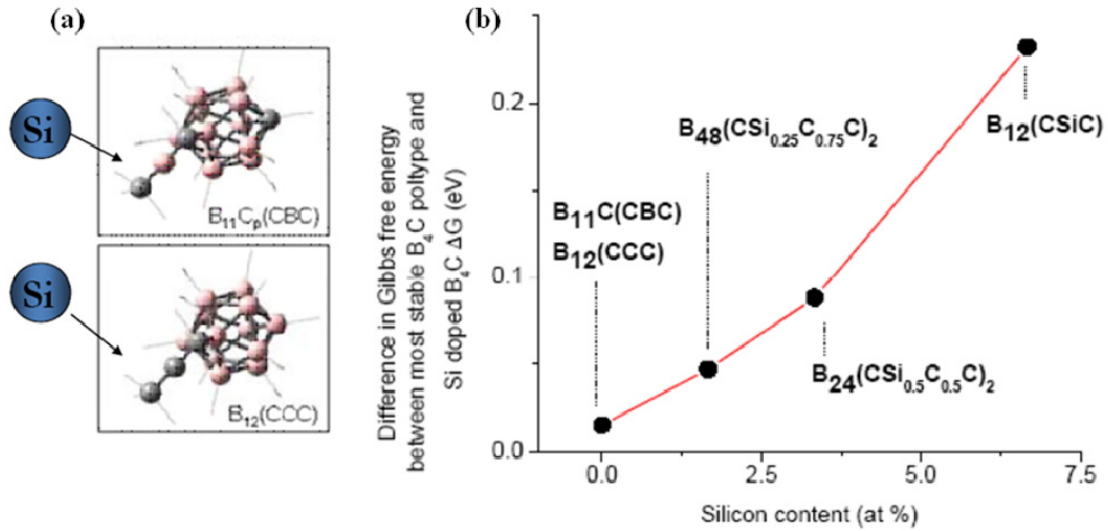


Figure 12. (a) Schematic of silicon (Si) doped B_4C and (b) Gibbs free energy of the $B_{11}C_p(\text{CBC})$ and $B_{12}(\text{CCC})$ polytypes as a function of silicon atom concentration. It can be observed that the difference in Gibbs free energy between the stable polytype, $B_{11}C_{(1-y,p)}\text{Si}_{(y,p)}(\text{CBC})$ and the most energetically favored minority polytype, $B_{12}(\text{CSi}_y\text{C}_{1-y})$ increase with the silicon content. Hence silicon-containing boron carbide is less affected by disorder than the undoped one [57].

| CHAPTER 3 | EXPERIMENTAL TECHNIQUES

Experimental techniques or characterization, when used in materials science, refers to the use of techniques to probe into the internal structure and properties of a material. Characterization can take the form of actual *in situ* materials testing, or analysis, for example in some form of microscopy or spectroscopy. These analysis techniques are used to magnify a specimen, visualize its internal structure, and gain knowledge as to the distribution of elements within the specimen and their physico-chemical interactions. In addition, these tools can be combined with each other to further probe the material and understand fundamental properties. In this chapter, various materials characterization and experimental techniques used in this research work are explored.

3.1 Indentation

In general, material deformation under indentation might involve such competing mechanisms as brittle macro- and microfracture, plasticity-dislocation and defect formation, and structural transformations in the material underneath the indenter (Figure 13). Although the first two mechanisms have been extensively studied and well understood in materials, the influence of a phase transformation's response to contact loading is largely underestimated due to the difficulties with structural characterization of the thin surface layer affected by contact interactions. Here, we are primarily concentrated on the deformation of boron carbide as a result of contact pressure induced solid-state phase transformation.

3.2 Nano-Indentation

Depth-sensing indentation, or nanoindentation for short, is a relatively new technique that allows *in situ* monitoring of indenter displacement as a function of applied force. Nanoindentation has proven to be a powerful technique in providing information on mechanical properties (hardness or elastic modulus) of the investigated materials, and variation of these properties with penetration depth, based on analysis of respective load-displacement curves. While diamond anvil experiments are capable of studying the mechanical deformation and phase transformation in bulk materials under hydrostatic pressure, the material behavior under nanoindentation is of more relevance to realistic contact or impact loading conditions. Moreover, the shape of nanoindentation load-displacement curves can often suggest structural changes that occur within the indented material during the test.

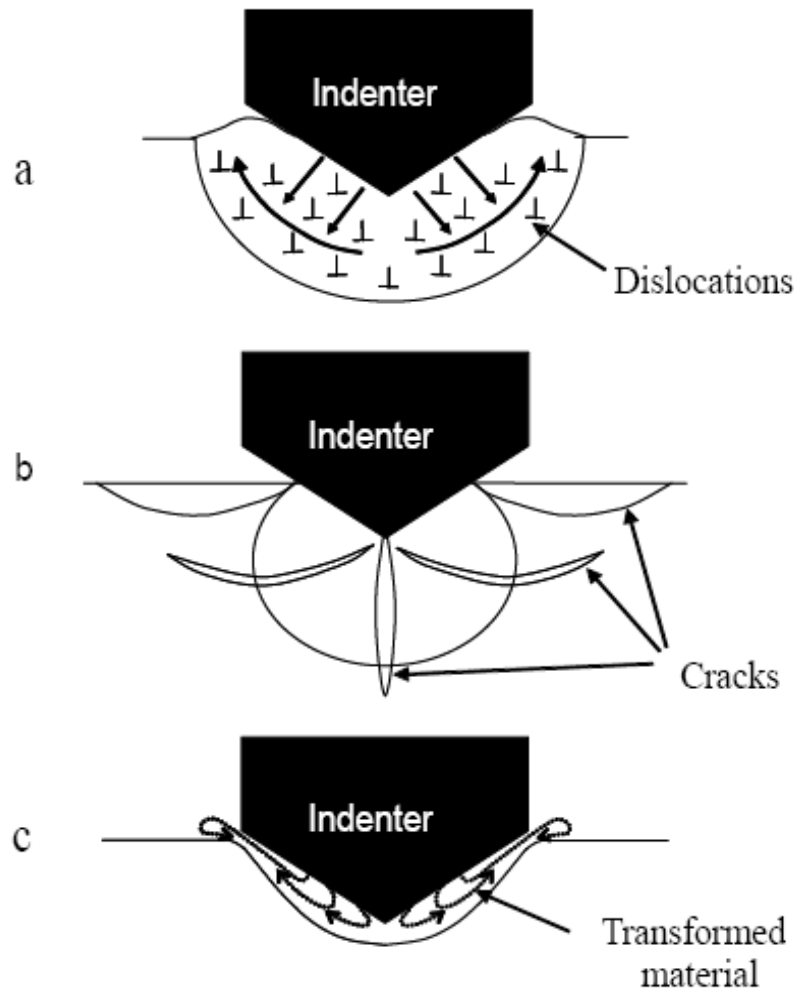


Figure 13. Schematic of deformation mechanism taking place during indentation: (a) dislocation-induced plastic flow, (b) brittle fracture, and (c) ductility induced by a high pressure phase transition into metallic state.

For this research, nanoindentation experiments were performed using a HysitronTriboindenter® along with a standard three-sided Berkovich pyramidal indenter tip. The imaging of the indents was carried out by the scanning probe microscopy (SPM) in the Triboindenter®. As shown in Figure 14, the system comprises the load application assembly, displacement sensor, and analysis tools. The loading column is made of stainless steel. The system is equipped with a motorized sample manipulation table with software control, an optical imaging system, a high-resolution video camera, a data

acquisition and control unit, a vibration isolation table, and an environmental isolation enclosure. The testing instrument has the three plate capacitive transducer that is used as both the actuator and sensor of the instrument. The force is applied electrostatically while the displacement is simultaneously measured by the change in capacitance. The indentation head assembly has the displacement resolution of 0.2 nm, and loading can be done up to maximum load of 100 nN, with a resolution of <1 nN. A standard three-sided Berkovich pyramidal indenter was used for this study. The total included angle of the indenter was close to 142.3° , with the tip radii around 70 nm

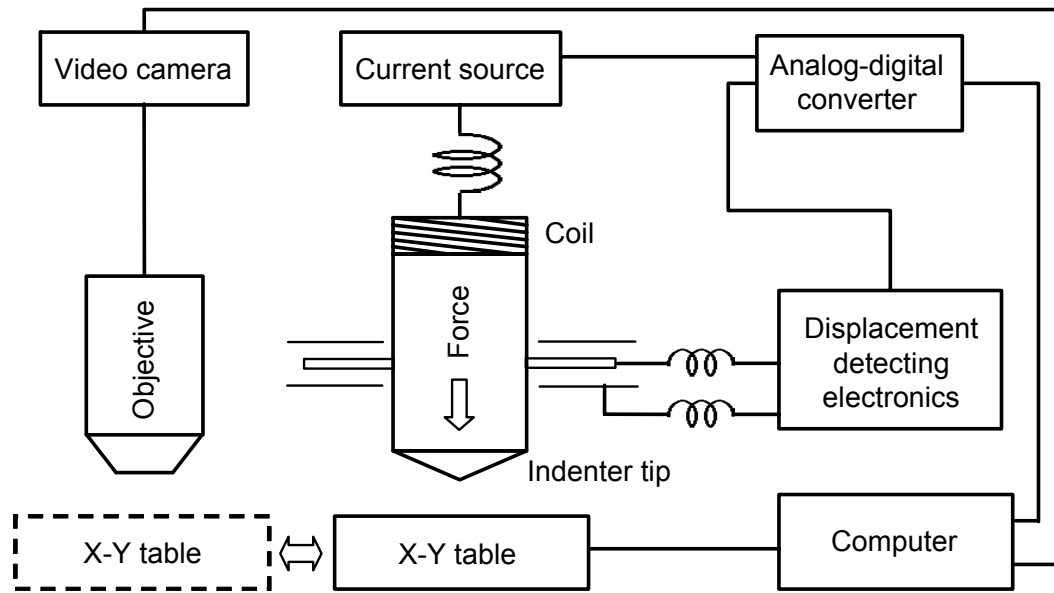


Figure 14. Schematic diagram of the nanoindentation experimental setup.

3.3 Raman Spectroscopy

The Raman effect is named after Nobel Laureate Dr. C. V. Raman. Raman spectroscopy has demonstrated its unique capability of identifying metastable phases of semiconductors and determining the residual stress on the surface subjected to contact loading. Raman spectroscopy is particularly useful for studies of phase transformation in boron carbide for several reasons. First, because Raman detects fundamental vibrations in materials, Raman bands normally have a good signal-to-noise ratio. This allows a Raman spectrum to be used for “fingerprinting” of different structures. Second, Raman analysis requires no special preparation of the targeted sample and is a non-destructive test. Third, a few seconds is efficient to acquire a high-quality Raman spectrum on B_4C . Thus, Raman Spectroscopy can be used to monitor phase transformation in real time. Moreover, due to the transparency of diamond anvils to laser beam, Raman spectroscopy can also be used for *in situ* investigation of high pressure phase transformations in DAC. Figure 15 shows a schematic of the device.

Typically, a Raman spectrometer consists of (i) a monochromatic light source for sample illumination, (ii) collection optics for redirection of the scattered light into (iii) the wavelength analyzer and (iv) the detector. The integration of a microscope makes a Raman spectrometer capable of performing analysis on very small regions of a sample, i.e. nano/microindentation. Figure 16 is a good example showing phase transformation in boron carbide indentation that has been identified by the use of Raman spectroscopy analysis.

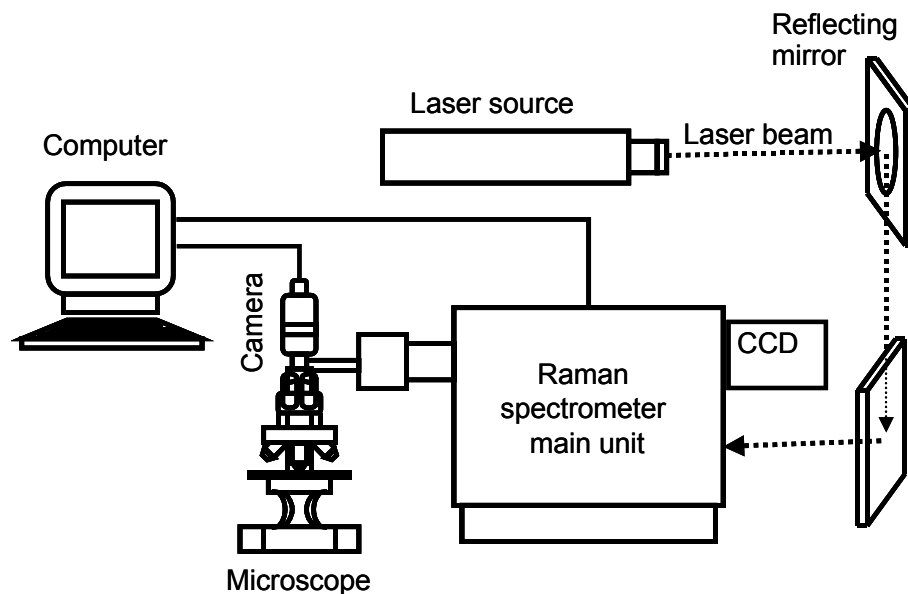


Figure 15. Schematic of a Raman microspectrometer. The monochromatic incident beam is redirected through a set of optical components into the microscope objective. The objective is used to illuminate the sample and to collect light scattered on the sample. Inelastically scattered light is then dispersed into a spectrum inside the main spectrometer unit. The computer collects the Raman signal from the charged coupled device (CCD) detector attached to the spectrometer and optical images from the video camera attached to the microscope.

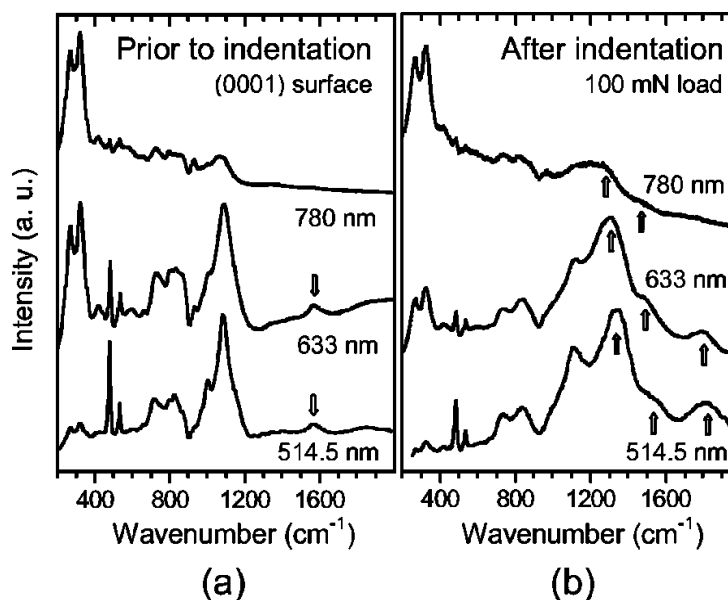


Figure 16. Raman spectra of pristine and indented boron carbide by a Ramascope 2000 (Reinshaw, UK). It shows that after nanoindentation, there is evolution different bands ~ 1320 and 1580 cm^{-1} , corresponding to D and G modes in carbon materials.

A Renishaw Raman microspectrometer was extensively used for phase analysis in this study. Three lasers, a 532 nm, a 633 nm He-Ne laser and a 785 nm diode laser, are used in this study. In addition, two other lasers, 488 nm and 514 nm Ar ion lasers, were also used to study the material (Jobin Yvon system). Three diffraction gratings (1200 grooves/mm for the 780 nm laser, 1800 grooves/mm for the 633 nm laser, and 2400 grooves/mm for the 514 nm laser) are available for dispersing scattered light into spectra, providing spectral resolution of approximately 1 cm^{-1} per pixel of the charge coupled device (CCD) camera. The spatial resolution is dependent upon the microscope objectives and can reach $1 \text{ }\mu\text{m}$ for a 100x objective. Origin 8 and Renishaw Wire software packages were used for analysis of collected single and multiple spectra.

3.3.1 Surface Enhanced Raman Spectroscopy (SERS)

Surface Enhanced Raman Spectroscopy (SERS) is a surface effect and is obtained by patterning the substrate, which significantly enhances the Raman scattering of the sample with up to 10 to 15 orders of magnitude, as shown in Figure 17 [58-60]. The exact mechanism behind SERS is not completely understood and is therefore still a subject of investigation and discussion. However, SERS is believed to be caused by an interaction of surface plasmons [61]. Surface plasmons are located in metals, so the typical choice of surface is either silver or gold [59]. For the scattering to occur, the plasmon oscillations must be perpendicular to the surface. This implies that the surface must have a certain roughness, which can either be a physical roughness or made up by the use of nano particles. Such a surface can be used to enhance the Raman scattering from e.g. a single molecule laying on the surface. SERS is believed to play an important role in detecting

phases which have low signal to noise ratio, hence it has been used in conjunction with indentation to analyse post indented samples.

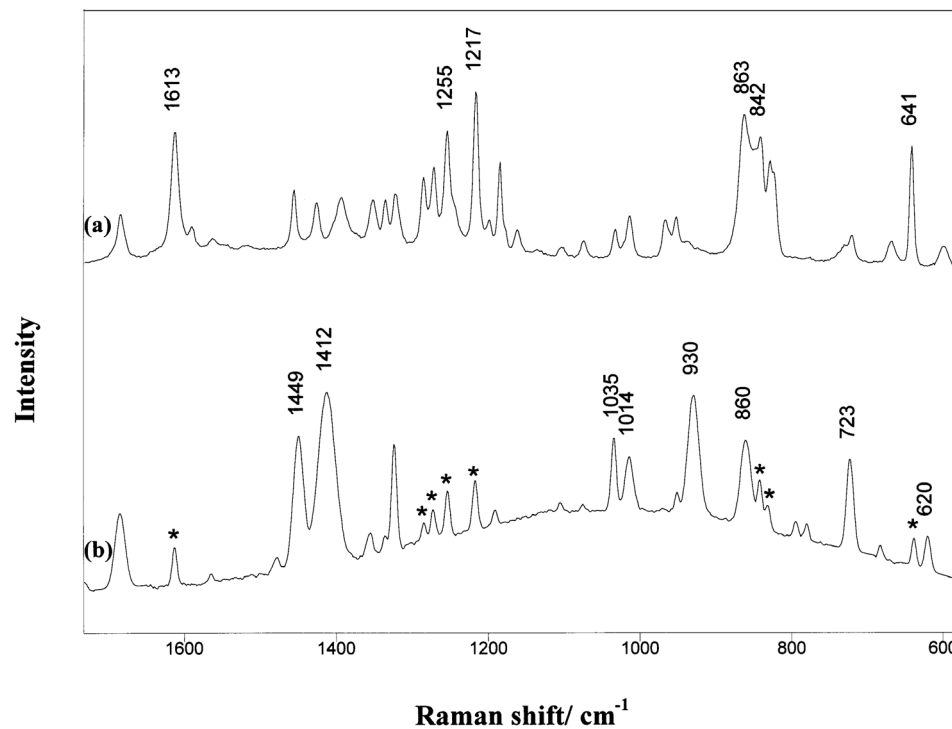


Figure 17. Comparison of (a) normal Raman and (b) SER spectra of tyr-gly molecule [60] showing the increase in the detection and intensity of the peaks.

3.4 Scanning Electron Microscopy (SEM) Characterization

Electron microscopy was first proposed and developed by German physicist and Nobel Laureate Ernst August Friedrich Ruska with his PhD advisor, Max Knoll, in the early 1930's [62]. In the scanning electron microscope (SEM), electrons are generated in an electron gun and focused into an electron beam, which then scans the surface of the material to generate an image. One of the most common sources for electron emission is the tungsten thermionic type, with Lanthanum hexaboride (LaB6) and field emission sources also in use today. In this work, an FEI XL30 SEM with a field emission gun was employed.

Once electrons are produced and emitted from the source, an anode with a high electrical potential is used to accelerate the electrons through a small hole and down the column towards the electromagnetic lenses. These lenses are used to control and optimize the electron beam as it travels down the column to the chamber [62]. The two types of lenses used in the SEM are the condenser lens and the objective lens as shown in Figure 18 [63]. The condenser lenses serve to focus the electron beam and reduce the electron beam crossover diameter to a final spot size of under 5 nm [62, 64]. The objective lens, with the aid of the stigmator and scanning coils, controls the scanning motion of the electron beam over the sample and serves to focus the image [62].

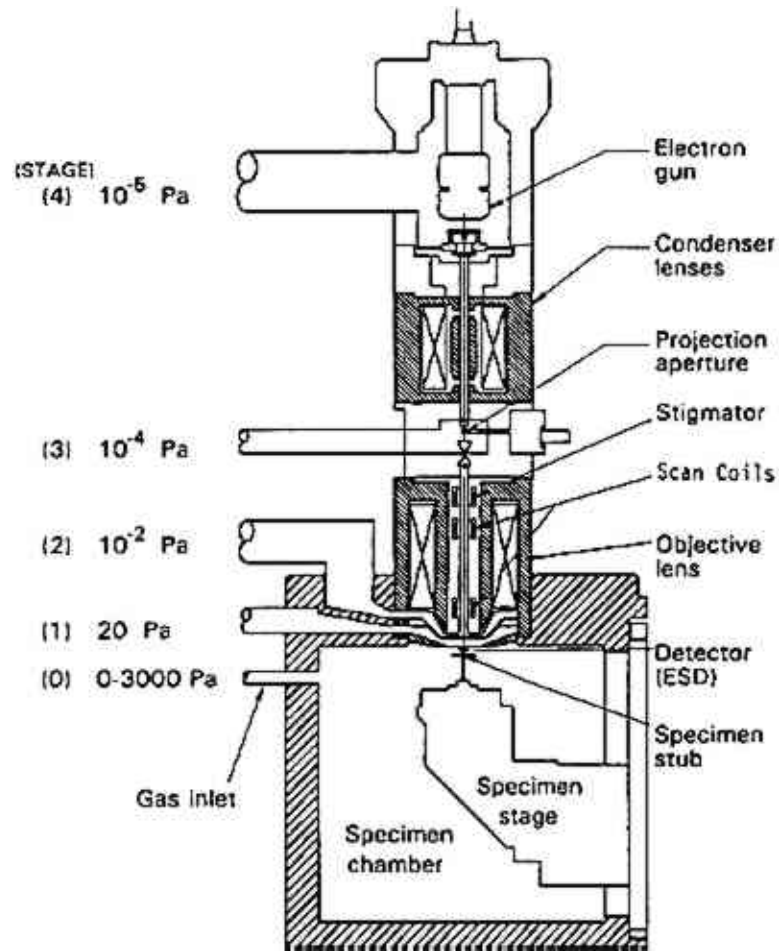


Figure 18. Schematic diagram of a scanning electron microscopy [63].

Once out in the chamber, the electron beam scans the sample in a raster fashion over a rectangular area. When an electron from the beam (known as the primary electron), interacts with the atoms of the specimen, two events can occur: elastic scattering or inelastic scattering [62, 65]. During elastic scattering, or Rutherford scattering, the primary electron is deflected by the positive nucleus of the specimen atom through Coulombic interactions so that its trajectory is deflected, but its kinetic energy remains constant [62].

It is important to note the dependence of elastic scattering on the atomic number of the material, as elastic scattering is also responsible for the phenomenon known as

backscattering. The backscattered electron signal results when the electron, after a single scattering event, deviates by more than 90° from its incident path [65]. Backscattered electrons are used to generate compositional images of a specimen consisting of two or more chemical phases, since backscattering increases with increasing atomic number of the specimen element.

In the case of inelastic scattering, an actual energy transfer occurs during the interaction between the primary electrons and the atoms of the specimen [62, 65]; from these collisions, low and high-energy secondary electrons, Auger electrons and x-rays, among other events, are generated. During these inelastic collisions, the kinetic energy of the primary electron decreases, but the deviation from its original trajectory is small in comparison to that in elastic scattering.

Inelastic scattering of the primary electron with the specimen atoms results in a promotion of loose valence electrons to the conduction band and subsequent motion of the atom's electron through the specimen [62]. Should these propagating electrons have enough energy when they reach the surface of the material, they will escape as secondary electrons (SEs). The energy transfer is usually relatively low, limiting low energy secondary electrons to those from atoms found in the surface (top 5 nm) of the sample. Fast secondary electrons, or those that are higher in energy, can also be generated at higher angles (nearly 90°) from the incident beam trajectory, but are not very common [65]. Because inelastic scattering usually results in low-energy electrons from the surface, secondary electrons serve to generate images of the topography of a sample.

3.5 Transmission Electron Microscopy (TEM) Characterization

TEM is the method of choice due to its unequalled capabilities of both dealing with the microstructure at high spatial resolution and providing crystallographic information. Therefore, as the primary characterization technique, TEM was extensively used throughout this research. TEM investigations were carried out on two different microscopes: a TOPCOM 002B TEM and a JOEL 2010F TEM/Scanning TEM. The TOPCOM 002B TEM works at 200 kV with a point-to-point resolution of 0.4 nm. Besides the attached PGT energy dispersive X – ray spectrometer (EDS), more important is its uniquely wide range of specimen tilting, $\pm 60^\circ$. The field-emission JOEL 2010F operates at 200 kV with a point-to-point resolution of 0.23 nm and a lattice resolution of 0.10 nm and has the Gatan electron energy loss spectrometer (EELS) which makes this microscope an ideal tool for high-resolution analytical and energy-filtering imaging. A variety of sample holders, including single tilt, double tilt, in situ hot stage (25 ~ 1000 °C) and cryo-stage (-175 ~ 50 °C), make the 2010F an instrument with full capabilities of various electron diffraction methods, bright/dark field and high resolution phase contrast imaging, and *in situ* experiments within a wide range of temperature.

To clearly understand the working principles and resultant advantages of TEM, the following sections describe the methodology and techniques used in TEM.

3.5.1 General Concept of Transmission Electron Microscopy

TEM was developed initially because of the limited image resolution in a light microscope, which is imposed by the wavelength of visible light ($\sim 0.5 \mu\text{m}$). The concept of resolution in an electron microscope is the same as that in conventional light

microscopy. Let us think of the image resolution in TEM in terms of classical Reyleigh criterion for light microscopy [66]

$$\delta = \frac{0.61\lambda}{\mu \sin \beta} \quad (3.1)$$

Here μ , the refractive index of the viewing medium can be approximated to be the unity; β , the semi-angle of collection of the magnifying lens, is generally very small (a few degrees); and λ , the wavelength of electron beam, is related to the accelerating voltage, E:

$$\lambda \sim \frac{1.22}{E^{1/2}} \quad (3.2)$$

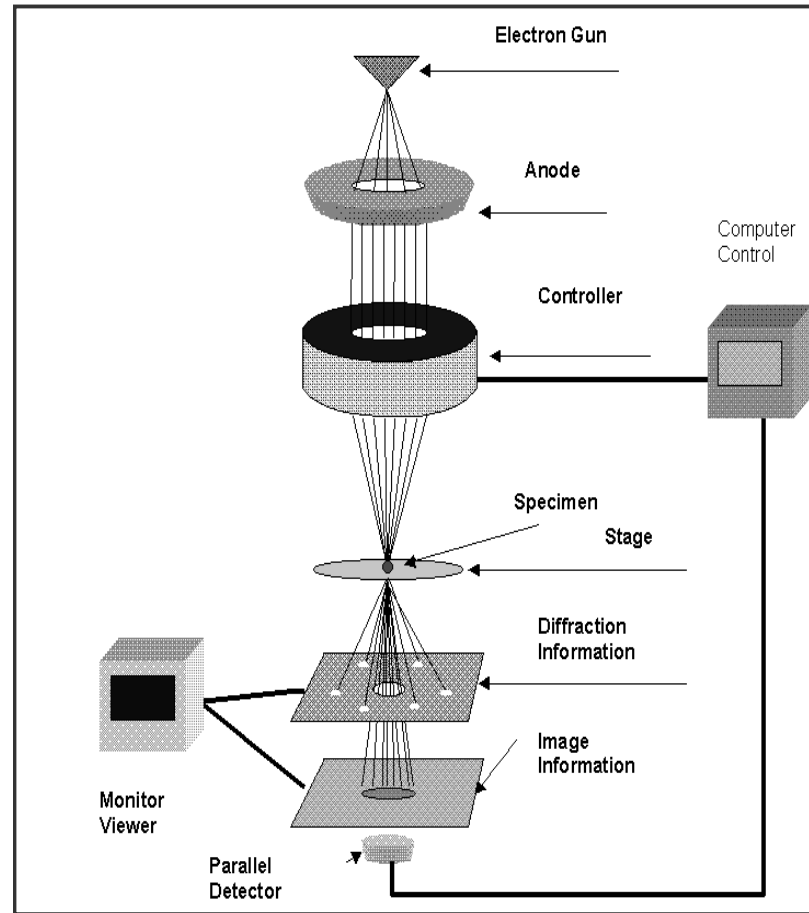


Figure 19. Schematic of a transmission electron microscope [67] .

Therefore, the above equations theoretically imply an electron wavelength of 0.004 nm and a resolution of 0.02 nm for a 100-keV electron. Unfortunately, such high resolution cannot be reached in TEM because of lens aberrations. State of the art TEMs can resolve two points about 0.2 nm apart. This is approximately the separation of atoms in solids. More recently, with successful incorporation of a spherical aberrations corrector (Cs corrector), a state-of-the-art high resolution TEM can even produce a sub-Ångstrom resolution. With its capability of extremely high resolution, TEM allows us to investigate detailed microstructural changes in materials subjected to localized contact loading, such as nanoindentation and nanoscratching.

In order to understand the way in which TEM works and the information it provides, it is necessary to consider the interaction between electrons and the specimen in more detail. As was discussed for SEM, when a high energy electron beam interacts with a thin specimen, many scattering processes, including elastic scattering, inelastic scattering and plasmon scattering, produce a wide range of secondary signals such as X-rays, secondary electrons, and backscattered electrons. Figure 19 shows a schematic diagram of a TEM. The electrons are produced by the electron gun, then accelerated through the anode plate and focused with a set of magnetic lenses. After traveling through the thin specimen, the electron beam forms images, or Diffraction Patterns (DPs) on a phosphorus screen and other imaging detectors. In this chapter, we focus on the direct beam and elastically scattered beams which form different contrast images and electron DPs.

3.5.2 Electron Diffraction

Using electron DPs produced by the elastically-scattered electrons, the arrangement of atoms (structural information) in a specimen can be deduced. By using either selected area aperture or a nano-sized (convergent) electron beam, a spatial resolution of electron diffraction from several microns to several nanometers can be reached in TEM. Thus, using electron diffraction in TEM, topics such as whether the material is crystalline or amorphous can be addressed, and if crystalline, then crystallographic characteristics such as the lattice parameter and crystal symmetry can be investigated. In this way, the occurrence of phase transformations (including

amorphization) upon contact loading can be clarified. More importantly, a new structure formed during contact loading can also be identified in TEM.

For elastically scattered electrons, the Bragg diffraction law states that

$$2d \sin \theta = n\lambda \quad (3.3)$$

where d is the interplanar spacing in the crystal, λ is the wavelength of the electron beam, θ is the Bragg angle and n can be any integer (Figure 20). In electron diffraction, only first order diffraction, i.e. $n=1$, is considered, and higher order diffraction is simply dealt with by using multiples of the Miller indices. In addition, the Bragg angle θ is typically so small that $\sin\theta$ can be approximated by θ . Hence the Bragg equation can be rewritten as

$$2d\theta = \lambda \quad (3.4)$$

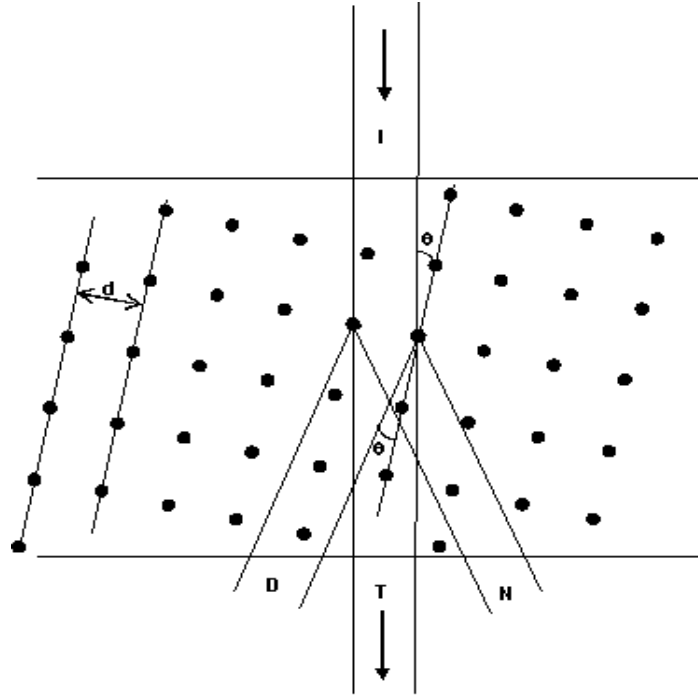


Figure 20. The scattering of an incident electron beam (I) by a crystal lattice. On the other side of the specimen, two kinds of intense beams can be found: the direct beam (T) and the diffracted beam (D). In other directions (e.g. N), no intense electron beam will be detected.

Figure 21 is a schematic diagram showing the formation of an electron DP in TEM. Thus, for a small diffracted angle, $r/L=2\theta$. Combining with the previous equation, we get

$$\frac{r}{L} = \frac{\lambda}{d}, \quad \text{or} \quad rd = L\lambda \quad (3.5)$$

$L\lambda$ is called as “camera constant” since it is independent from the specimen. If the camera length is known, then the interplanar d spacing can be determined by simply measuring r on the pattern. The most common electron diffraction in TEM is selected

area diffraction (SAD), in which a selected area aperture is inserted into the image plane of the objective lens to select a specific area in the specimen that will contribute to the DP. In addition to SAD pattern, there are other DPs, such as nanobeam electron microdiffraction, convergent beam electron diffraction (CBED) and Kikuchi lines. Further details on different diffraction techniques can be found in general TEM references [66-69] .

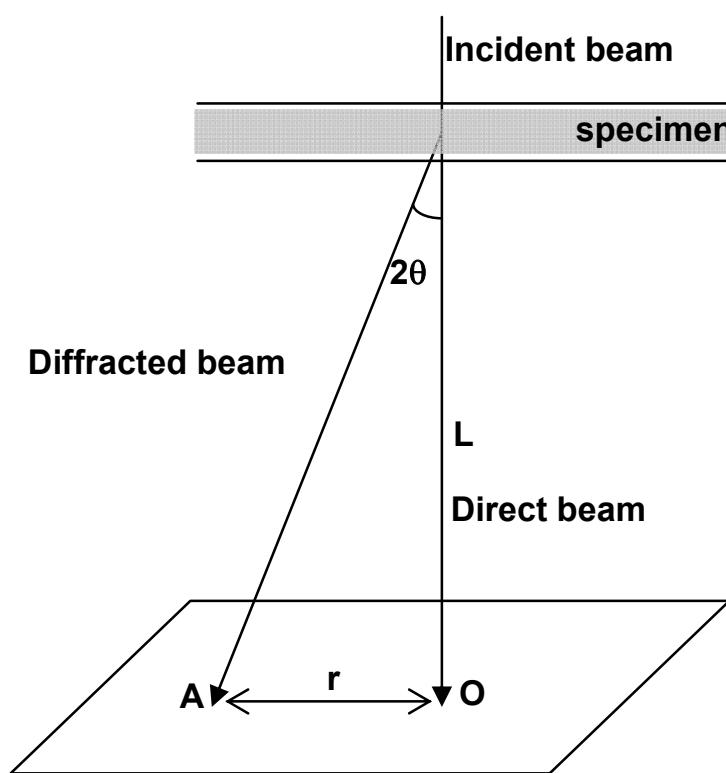


Figure 21. Schematic illustrating electron diffraction in TEM.

It is important to note that the actual TEM contrast of images and sample preparation procedures are complicated and have only been briefly stated here. To get a more comprehensive coverage of TEM principles, readers are referred to the general TEM literature.

| CHAPTER 4 | STATIC INDENTATION STUDIES

A detailed investigation of armor-grade boron carbide (B_4C) samples by Raman spectroscopy is discussed in this chapter. The results show that the samples are spatially inhomogeneous and contain sp^2 carbon inclusions. Specifically, Raman investigation has been performed on: i) as-synthesized boron carbide powders ii) hot pressed samples, and iii) regions on the hot pressed samples damaged by micro-indentation. Unlike the other Raman-active vibrations in boron carbide, the peak at $\sim 1700\text{-}1800\text{ cm}^{-1}$ changes its frequency at different Raman excitation wavelengths, as frequently observed for the G-peak in amorphous carbons. This suggests that such a peak is in resonance with localized π -electrons in graphitic domains under compressive stress, rather than arising from B-C bonds in amorphous boron carbide. Comparison of bulk and surface-enhanced Raman scattering (SERS) allowed us to carry out a cross-sectional analysis of the sample regions damaged by microindentation. In such regions, the surface is generally more disordered and less affected by residual compressive stress than the bulk.

4.1 Introduction

Owing to its high dynamic elasticity and low density, hot pressed boron carbide (B_4C) is the material of choice for lightweight ceramic armor applications. Its crystallographic structure characterized by a 15-atomic unit cell [26] is typical of a number of boron-rich solids. More specifically, 12 atoms form an almost regular icosahedron while the remaining 3 atoms are in linear chains. Boron carbide is peculiar in that the exact location of the boron and carbon atoms in the unit cell is affected by a certain degree of substitutional disorder [2, 26].

The factors limiting the ballistic performance of B_4C have been the subject of numerous studies [1, 2, 26, 45, 48]. It has been theoretically demonstrated [2] that the failure of B_4C at high shock impact is related to the segregation of amorphized sp^2 carbon clusters along the (113) crystallographic plane. The observation of amorphous bands in this plane was correlated to the presence of the B_{12} (CCC) polytype in boron carbide [2].

The occurrence of numerous stable polytypes in boron carbide has been attributed to substitutional disorder. In addition to the thermodynamically unavoidable substitutional disorder, Chen *et al.* [70] demonstrated that specimens produced by hot pressing B_4C powders from different commercial sources may lead to variable amounts of inter- and intra-granular sp^2 carbon inclusions. This makes the detection and characterization of graphite an important issue for evaluating the quality of boron carbide powders and the subsequent hot pressed components. Furthermore, although the existence of substitutional disorder in boron carbide is widely accepted [23, 26, 71], it is not clear whether this is determined by the hot pressing procedures or by intrinsic properties of the starting powder resulting from the synthesis parameters. In addition to

the determination of the amount and characteristics of the carbon phase in boron carbide powder and dense samples, several studies on the segregation of sp^2 clustered carbon from boron carbide upon static and dynamic indentation have been reported [46].

Understanding the mechanism for the segregation and the characteristics of the sp^2 carbon would be useful in understanding the failure mechanism in boron carbide. Raman spectroscopy is a widely used non-destructive technique for characterizing sp^2 bonded amorphous carbon and related materials [46, 72-77]. Also, the Raman spectrum of B_4C has been thoroughly studied using a variety of excitation wavelengths [21, 51, 77-79], although some details on the interpretation vary [21, 79]. In addition to bulk analysis using multi-wavelength Raman, surface-enhanced Raman scattering (SERS) is useful for exploring the properties of surfaces. SERS exploits the electric field enhancement provided by metallic nanoparticles [80]. The comparison of bulk and SERS Raman spectra could provide significant information regarding the depth of transformations occurring in boron carbide upon indentation or shock damage. It is therefore possible, via the use of Raman maps, to characterize the homogeneity, purity and amount of sp^2 bonded amorphous carbon inclusions in armor-grade boron carbide specimens. A commercially available B_4C powder has been investigated in detail. A similar investigation has been carried on a hot-pressed sample prepared from the same powder. In addition, Raman has been repeated on the same region before and after micro-indentation of the hot-pressed sample.

Finally, SERS spectra were recorded before and after indentation, showing higher degree of disorder (amorphization) and relaxation on the surface than in the bulk of the samples. Although the results demonstrated in the following sections refer to powder and

hot pressed samples produced by material from one supplier, we have verified them to be at least qualitatively valid for a number of samples provided by a range of different manufacturers.

4.2 Experimental Details

Boron carbide powders and microcrystalline hot-pressed samples were provided by the same supplier. The supplier also provided samples for ballistic tests at the US Army Research Laboratory (Aberdeen, MD). The powder sample discussed here was synthesized at 1400 °C from boron oxide and graphite powder in an arc furnace. Typical grain size was 10 µm or more. The microcrystalline sample was densified by hot-pressing at 2000 °C to achieve a density close to the theoretical one for B₄C (2.51 g/cm³). The exact stoichiometry was about B_{4.2}C, and the average free carbon content, as measured with a carbon analyzer, was ~0.5%. The sample for Raman investigation was obtained by cutting a 2 mm thick slice in the middle of the 2 cm thick hot-pressed tile. Figure 22a and 22b show scanning electron micrographs (SEM) from the powder and the corresponding hot pressed sample, respectively. The distribution of grain sizes in the powder, and their coalescence after hot-pressing, can be readily observed. The absence of obvious pores or other defects suggests that a high density sample (> 99 %) was achieved after hot pressing. Surface impurities, which appear to be bright in the SEM, are also visible in Figure 22a and 22b. Indentations were performed using a Vickers micro-indenter at 100 g, 200 g and 300 g loads on B₄C surfaces mechanically polished to an optical finish. The Raman maps were recorded at 1 mW laser power by a Renishaw InVia Raman spectrometer coupled with an x-y computer controlled sample positioning stage (1 µm accuracy) and the WIRE-2TM mapping software. 15 x 16 mesh grids at 2.5 µm spacing

where used in order to investigate the regions subjected to indentation while coarser sampling (50 random points at more than 100 μm distance each) was used to map the powders, in order to sample a suitable number of grains. Sp^2 rich amorphous carbon materials, being semimetals, are highly responsive to low photon energies, while the optical absorption of B_4C , which is a semiconductor, increases at higher photon energies. Therefore, in order to improve the sensitivity of Raman for the lowest concentrations of sp^2 carbon inclusions, we carried out most of our investigations at low, near-infrared excitation energy (1.57 eV, $\lambda = 785 \text{ nm}$) with a semiconductor laser. The relatively low absorption coefficient of boron carbide at 785 nm [$\alpha(785 \text{ nm}) \sim 10^3 \text{ cm}^{-1}$, as measured by ellipsometry, Figure 22c] allows depth sensitivity of Raman of about $1/\alpha \sim 10 \mu\text{m}$, while, at visible Raman excitation, $\alpha(\lambda_{\text{vis}}) \geq 10^4 \text{ cm}^{-1}$ and the depth sensitivity is much lower, below 1 μm . This is a second, important reason for using low excitation energy, since the grain sizes of our B_4C specimens (about 10-50 μm in radius, as shown in Figure 22a) make near-infrared Raman a bulk-sensitive technique, while visible Raman is surface-sensitive. Additional visible Raman spectra were recorded at 633 nm (Renishaw InVia spectrometer), 532 nm, 515 nm, and 457 nm (Jobin-Yvon U-1000 and Aramis spectrometers) to obtain additional information about the nature of the sp^2 carbon phase [72, 73].

Surface-enhancement of the Raman signal was obtained at 785 nm excitation by dropcasting a colloidal suspension ($250 \mu\text{l} / \text{mm}^2$) of gold nanoparticles (Aldrich Inc.) on the sample surface. In this case, the Raman sensitivity at the surface is about 10^2 - 10^5 times stronger than that of the bulk [80] since the used excitation energy (1.57 eV) is close to the plasmon of gold. The cross-sectional depth can be estimated to be the size of

the Au particles, ~ 5 nm. Deposition of the nanoparticles was carried on *in-situ*, without removing the sample from the x-y positioning stage, so that the measurements positions could be exactly correlated between the bulk and SERS maps before and after the treatment.

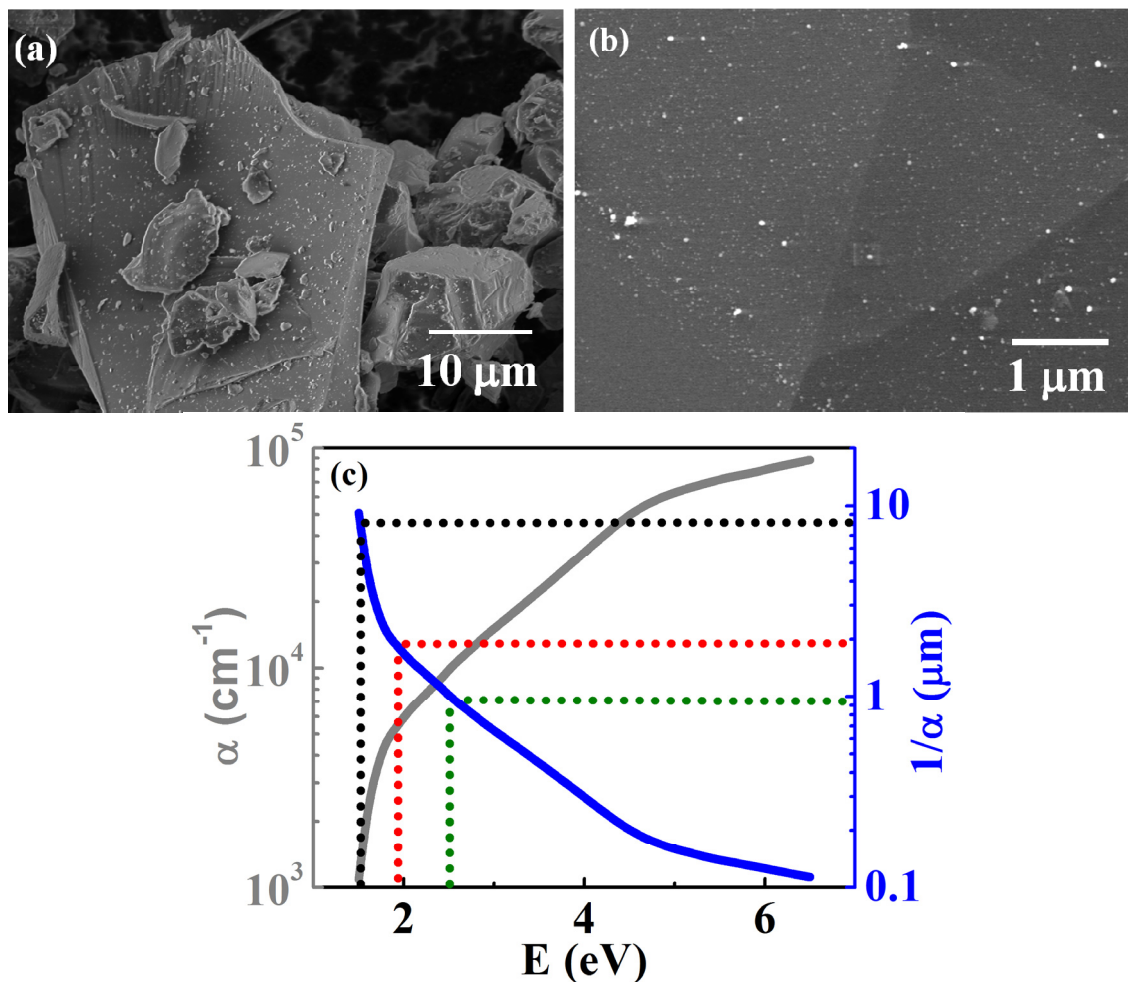


Figure 22. Scanning electron micrographs (SEM) of the samples analyzed in the present work: (a) Powder sample in which the distribution of grain sizes can be recognized. (b) Hot pressed sample from the same powder type reported in panel a, where brighter, presumably more conducting, grains (presumably intergranular graphitic islands) can be recognized. Inset in panel b reports the optical absorption coefficient of the sample, as inferred by spectroscopic ellipsometry data (Jobin-Yvon UVISSEL ellipsometer) assuming a semi-infinite medium for the air-sample system. Vertical bars indicate the used Raman excitation energies.

4.2.1 Size of the sp^2 aromatic domains

The first-order Raman spectrum of graphite single crystals shows only one peak at 1589 cm^{-1} (G-peak), which is the fingerprint of stretching vibrations of double, $C=C$, bonds [72, 73]. In the presence of graphitic domains of finite size [46, 74], amorphization of the graphene layer [73], or defects [75] a second peak appears at about $1300\text{-}1360\text{ cm}^{-1}$ (D-peak) (Figure 23). Such peak can be assigned to breathing vibrations of aromatic 6-fold rings in finite graphitic domains. In particular, it has been shown that at visible or near infrared excitation wavelength, λ , the diameter, L , of the sp^2 domain is related to the D/G intensity ratio by the following relationships [72, 73, 76]:

$$L = C(\lambda) \cdot [I(D) / I(G)]^{-1} \quad L \geq L_c \approx 20 \text{ \AA} \quad (4.1a)$$

$$L = C'(\lambda) \cdot [I(D) / I(G)]^{1/2} \quad L \leq L_c \approx 20 \text{ \AA} \quad (4.1b)$$

The Tuinstra-Konig relationship (4.1a) [76] is suitable for micro- and nano-crystalline graphite-like clusters, where the cross-section of the D-peak is controlled by the increasing electron confinement at smaller L . Relationship (4.1b), introduced by Ferrari and Robertson, holds at the smallest values of L where the increasing structural disorder affects the probability of finding regular 6-fold rings responsible to the D vibration mode in such small sp^2 carbon domains. In the case of small L , the half widths at half-maxima (HWHM) of the G- and D-peaks are much broader, since they are strongly affected by phonon confinement.

In regime (4.1a), the sum of the HWHMs of the G and D peaks is smaller than the difference between the peak positions $[\Omega(G) - \Omega(D)]$. Therefore, in such regimes a “dip” [73] (i.e. a local minimum) between the two bands is present, while in regime (4.1b) the two peaks are convoluted. Thus, a rule of thumb to distinguish regime (4.1a) from (4.1b) [73] is the fulfillment of the condition:

$$\text{HWHM}(G) + \text{HWHM}(D) < \Omega(G) - \Omega(D) \quad (4.2)$$

The frequency of the D-peak [11] and its intensity $I(D)$ [76] are strongly dependent on the laser excitation wavelength. Therefore, constants $C(\lambda)$ and $C'(\lambda)$ in eq. (4.1a) depend on λ [72]. Matthews *et al.* [75] showed that $C(\lambda) = C_0 + \lambda \cdot C_1$ ($C_0 = -126$ Å and $C_1 = 0.033$) so that $C(785 \text{ nm}) \approx 133$ Å and, imposing the continuity at $L = L_c$ [72], it can be obtained that $C'(785 \text{ nm}) \approx 8$ Å.

4.2.2 Concentration of the inclusions

Raman has also been widely used to characterize B_4C which, owing to its complex crystallographic structure, gives rise to a number of Raman-active vibrations at and below 1150 cm^{-1} [21]. Thus, Raman contributions of B_4C are easily distinguishable from the modes of the aromatic sp^2 clusters found at higher frequencies. Although some controversy remains on the origin of some B_4C peaks [21, 77, 79, 81], all the studies performed to date agree that the strong peak at $\sim 1100 \text{ cm}^{-1}$ can be assigned to the icosahedron breathing mode (IBM) (Figure 23). The other B_4C modes are found at 275-325 cm^{-1} (origin of which will be discussed elsewhere), at 480 cm^{-1} (attributed to C-B-C

chainstretching mode [81]), and at 525 cm^{-1} (the icosahedral libration mode [81]). The latter two peaks are strongly dependent on the orientation of the B_4C microcrystals with respect to the Raman laser beam, but they generally scale in intensity with the IBM mode (e.g. Figure 24) in all of our measurements. A similar scaling behavior is also observed for the other B_4C modes at $650\text{-}1000\text{ cm}^{-1}$.

We will use the IBM of B_4C as the control peak to normalize the relative amounts of graphitic and amorphous carbon inclusions to eliminate variations in Raman cross section, due to slight change in roughness and reflectivity of the grains for example. Furthermore, the Raman cross section of the D-peak varies strongly with the aromatic cluster size, the amount of disorder and, possibly, the concentration of defects. The cross-section of the G-peak at a given excitation wavelength is almost independent of all such factors. Thus, the G-peak intensity is proportional to the local concentration of π -electrons and, hence, the amount of sp^2 carbon sites (Csp^2) in the sample. Therefore, using the IBM peak intensity $[I(\text{IBM})]$ as a reference we can assume that:

$$\text{Csp2(at \%)} = K(\lambda) \cdot I(\text{G}) / I(\text{IBM}) \quad (4.3)$$

where $K(\lambda)$ is a proportionality factor to be determined. Below, we will use eqs.(4.1a and 4.1b) and (4.3) to obtain information about the size and the amount of sp^2 aromatic carbon clusters in the B_4C samples.

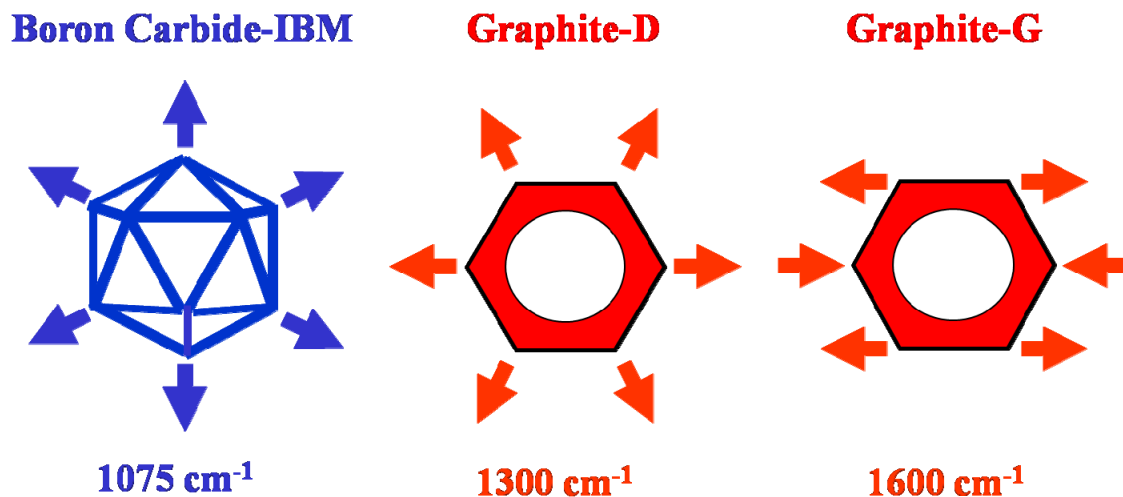


Figure 23. Raman active modes in typical boron carbide spectrum are shown. The three Raman vibrations used for our statistical analysis: the icosahedral breathing (IBM) mode of boron carbide at $\sim 1075 \text{ cm}^{-1}$ and the D and G peaks of graphite and a-C ($1250\text{-}1350 \text{ cm}^{-1}$ and $1500\text{-}1600 \text{ cm}^{-1}$ respectively) [26, 72, 73].

4.3 Results and Discussion

4.3.1 Powder samples

Raman spectra recorded from the powder sample at three different excitation wavelengths (785 nm, 633 nm, 532 nm) are plotted in Figure 24. The IBM at about 1100 cm^{-1} can be observed in all the spectra. The two strong low frequency modes at $275\text{-}325 \text{ cm}^{-1}$ are features present in infrared Raman, but suppressed in the visible Raman spectra of our B_4C samples. The sharp peaks at 480 cm^{-1} and 525 cm^{-1} are also seen in Figure 24a. Raman spectra recorded on three different powder grains are shown in Figure 24b. We observed that, although the Raman peaks related to the B_4C phase are similar, the characteristics of the D and G peaks can differ substantially from grain to grain, indicating different amounts of sp^2 carbon and disorder. More significantly, the D/G intensity ratio is also strongly dependent on the grain probed, suggesting that the distribution and size of sp^2 clusters is very inhomogeneous in the powder sample.

These conclusions are quantified in Figure 25, which summarizes the results of a statistical analysis of the $I(D)/I(G)$ ratio and the $I(G)/I(IBM)$ ratio from fifty Raman spectra (785 nm) recorded on random grains. Fig. 25a reports the statistical distributions of $I(D)/I(G)$. In all spectra, G and D peaks were distinct and, thus, although broadened by disorder, they were sufficiently narrow to fulfill eq. (4.2). Hence, from Figure 25a, the sp^2 aromatic island sizes can be directly determined via eq.(4.1a) and estimated to range between 50 and 250 Å. Curiously, the island size distribution in Figure 25a exhibits a bimodal character, with two distinct maxima at $L_{(a)} \approx 100$ Å and $L_{(b)} \approx 65$ Å, respectively. Similarly, the distribution of the $I(G)/I(IBM)$ ratio, reflecting the statistical distribution of the amount of aromatic inclusions in the material, shows two maxima [at approximately $I(G)/I(IBM)_{(a)} \approx 0.2$ and $I(G)/I(IBM)_{(a)} \approx 0.7$, see Figure 25b]. Furthermore, as shown in Figure 25c, clear correlation is observed between low $I(G)/I(IBM)$ ratios and high $I(D)/I(G)$ ratios [region (a)] or between high $I(G)/I(IBM)$ ratios and low $I(D)/I(G)$ ratios [region (b)]. We can therefore conclude that two different aromatic inclusions are present in the sample, “type 1” and “type 2”. The first being larger and more abundant inclusions while the second being smaller and present in lower amount. These results agree very well with the current assessment on the distribution of aromatic inclusions in commercial boron carbide samples. TEM analysis by Chen *et al.* [70], have indeed shown that graphite-like domains can be found in B_4C in two distinct forms: smaller intra-granular inclusions, which may correspond to “type 2” Raman spectra, and larger inter-granular precipitates, consistent in size with “type 1”.

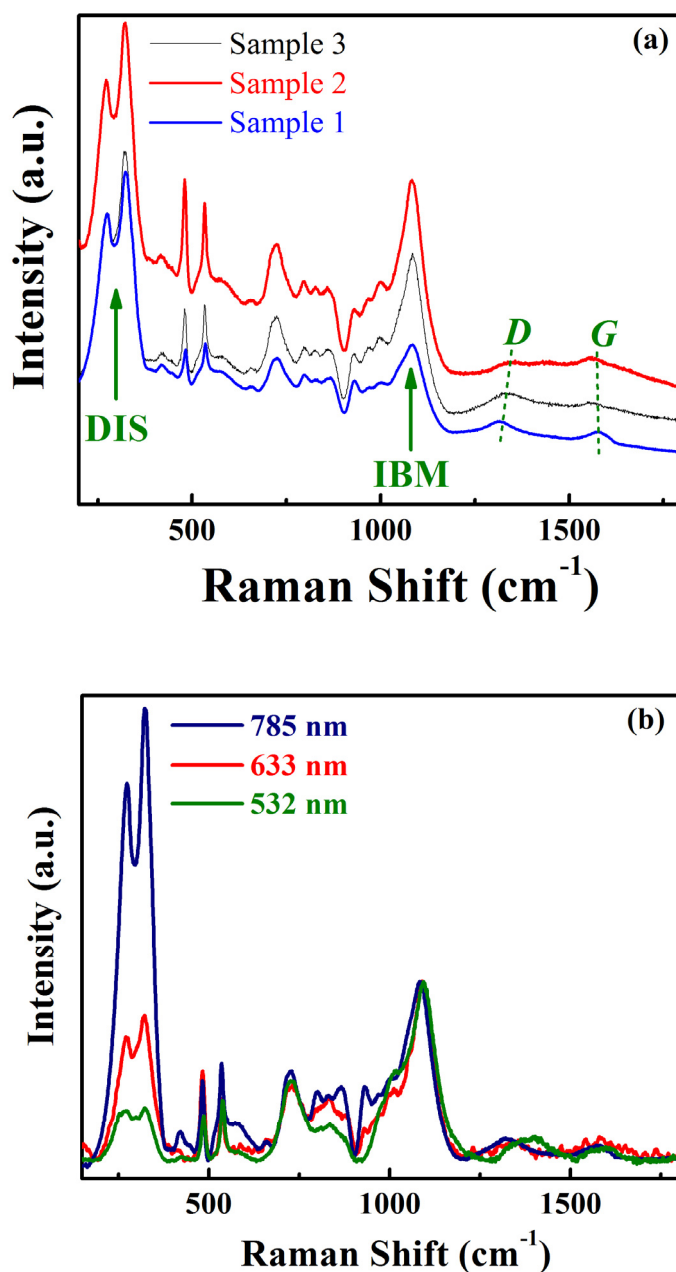


Figure 24. (a) Example of B₄C powder spectra at three different excitation wavelengths spanning from near-infrared (785 nm, 1.57 eV) to visible wavelength (532 nm, 2.34 eV). The steady decrease of the low frequency modes (275 cm⁻¹ and 325 cm⁻¹) and the reduced sensitivity to the D and G sp² carbon modes at increasing excitation energy can be observed. (b) Example of four B₄C powder spectra on different powder grains at constant excitation energy (785 nm, 1.57 eV).

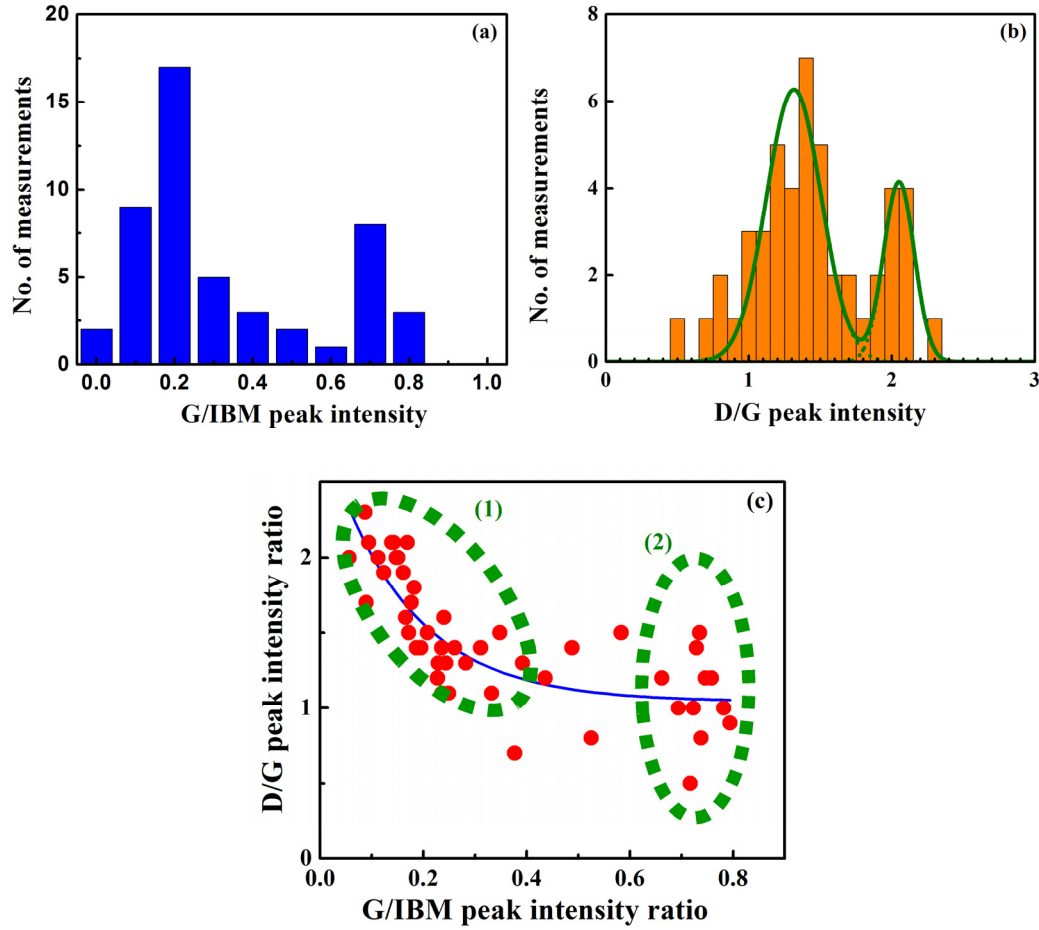


Figure 25. (a) Statistical distribution of the $I(G) / I(D)$ ratio in the 48 of 50 stochastically recorded Raman spectra on powder in which these modes could be detected (b) Statistical distribution of the $I(IBM) / I(G)$ ratio in the stochastically recorded Raman spectra on powder. It can be seen that in both cases (panel a and b) the distributions are bimodal. (c) correlations between the statistical distributions of $I(IBM) / I(G)$ and $I(G) / I(D)$ ratios, revealing two different groups of Raman spectra, “type 1” and “type 2” corresponding to intra- and intergranular graphitic inclusions in the powder.

4.3.2 As prepared hot-pressed sample

As shown in Figure 26, the Raman spectra of the hot pressed sample do not substantially differ from those of the powder. Specifically, Figure 26a shows that there is little or no difference between the boron-carbide related peaks of the powder and of the solid sample both in relative intensity and or frequency positions. Similarly, the peaks

arising from the sp^2 carbon phase of the hot pressed sample approximately undergo the same statistical fluctuations observed for the powder. Thus, the average carbon portion of the Raman spectra is also comparable for the powder and the densified sample, as shown in Figure 26b where two low-resolution Raman spectra from powder and hot-pressed samples are compared. This indicates that neither hot pressing nor sample cutting introduced significant amount of carbon inclusions in the densified sample. In addition, since our surface has been cut through the center of the tile, we may rule out that the observed sp^2 carbon clusters arise from surface carbon contamination.

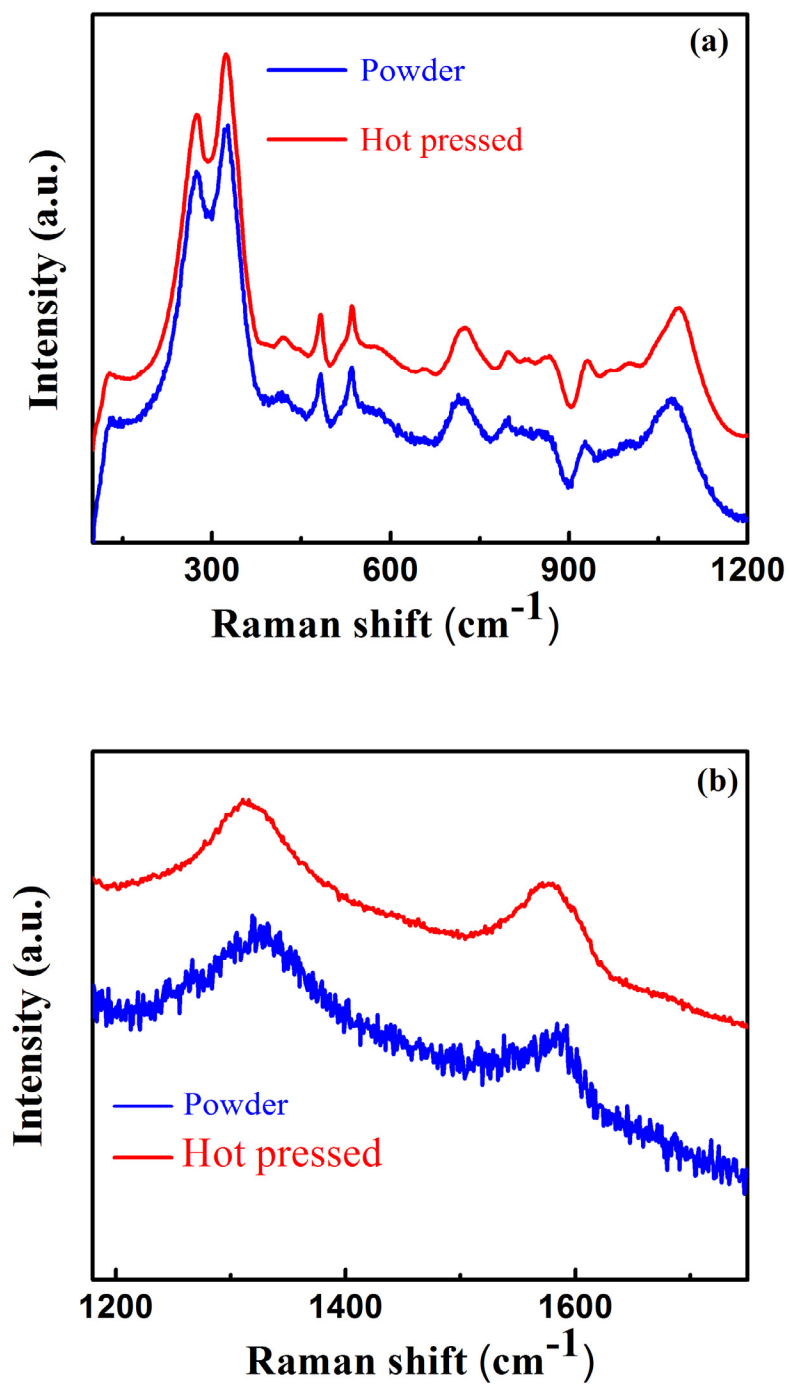


Figure 26. Micro Raman spectrum (a) Comparison of substantially identical 785 nm Raman spectra from powder and hot pressed sample. (b) The similarity in D and G modes is also evident.

4.3.3 Indented hot-pressed sample

Vickers indentations at 100 – 300 g loads were performed on hot pressed samples. The scanning probe micrographs (SPM) of three indents at 100g (Figure 27a), 200g (Figure 27b) and 300 g (Figure 27c), from different regions are shown in Figure 27. The damage for the 100g and 200g loads is relatively lower than the 300g indent. More significantly, we found that the indent damage varied from region to region on the sample at a load of 300g as highlighted by the images shown in Figure 27c. Such variability in the indent features is presumably dependent on the quality of the indented grain. Raman spectra recorded on the untouched region near the indent reveal that indentations in panel Figure 27b and 27c are indeed on two grains with very different G and D peaks. The Raman spectra of the two regions broadly correspond to “type 1” and “type 2” described in Figure 22. We observed that the indentations on “type 1” regions (Figure 27c) exhibit median cracks departing from the corners. In contrast, more extensive damage with high amount of displaced matter was observed for indentation on “type 2” regions. In order to understand the mechanisms leading to the extensive damage by indentation in “type 2” samples, Raman mapping of indented regions, was performed. The 15 x 14 Raman mapping grid with 2.5 μm steps is shown in Figure 28. More specifically, the image in Figure 28a is the indented region used for bulk Raman mapping while the image in Figure 28b is the same indent coated with Au nanoparticles for SERS analysis.

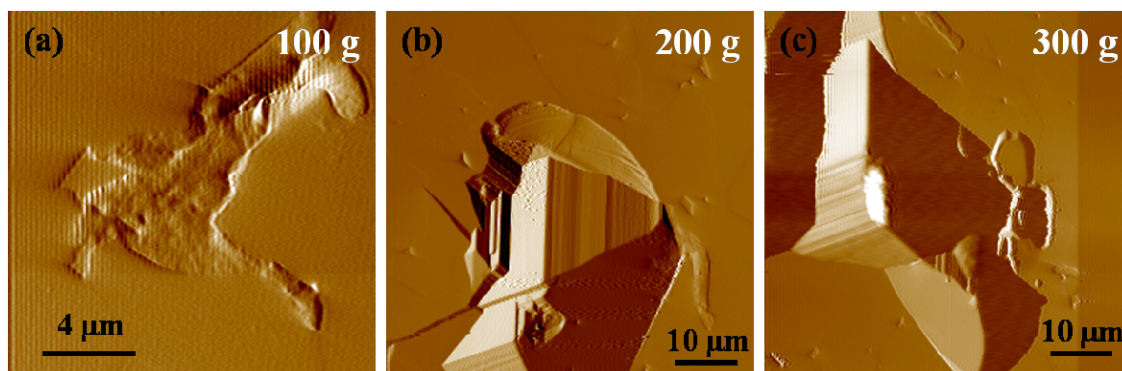


Figure 27. SPM images of indents on the B₄C hot pressed sample at increasing load: (a) 100 g, (b) 200 g and (c) 300g.

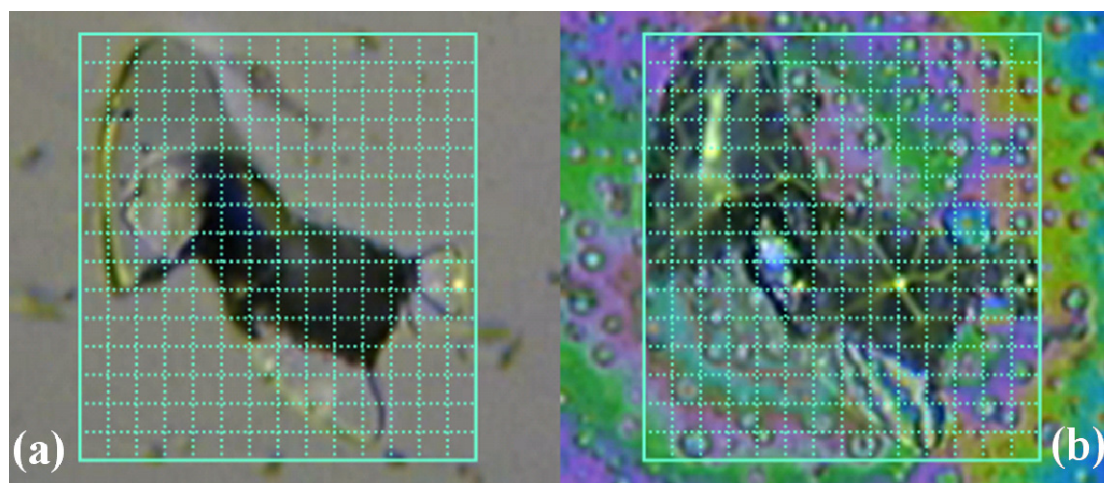


Figure 28. Raman Mapping grid on the optical images of the “type b” indentation at 300 mg load used for our considerations (a) before and (b) after dispersion of the gold particles. The grids used for Raman-mapping of the indentation are also evidenced. Each grid has a 2.5 μm step.

The results of the Raman mapping are shown in Figure 29. Below, we discuss the four different types of bulk and SERS Raman spectra we observed in specific regions on the indent from our mapping study. Black lines in Figure 29(a-d) indicate bulk Raman spectra from four regions on the map. The region in Figure 29a corresponds to displaced material resting on the sample surface in the proximity of the indentation. This region shows very sharp Raman D and G peaks, indicating relatively ordered sp^2 carbon material. This is intriguing because in all of our measurements, we were never able to

detect such sharp Raman peaks in the undamaged material. The results appear to indicate that the indent has affected the medium-range order in the material. An alternative explanation of the phenomenon is that an unusually large sub-superficial graphitic grain moved to the surface during the indent tip penetration but this is unlikely because we never observed such highly ordered aromatic islands in the undamaged material. In Figure 29b, the bulk Raman spectrum of a large crack departing almost from the middle of the indentation print is shown. Within such a crack, Raman spectra with unusually low D/G ratio were recorded. This may indicate very large graphitic islands. However, it should also be observed that the G-peak in this region is strongly blue-shifted (above 1600 cm^{-1}). Similar upshifts have been frequently observed in amorphous carbon when a significant proportion of the sp^2 sites form olefinic ($\text{C}=\text{C}$) bonds instead of aromatic rings [72]. Olefinic chains might also explain the absence of the D-peak, a signature of aromatic sp^2 carbon [72].

In Figure 29c, the Raman mapping results from a large region within the indent is shown. In this region, no relevant change in the G/D ratio or G-peak position is observed. This suggests that the nature of the sp^2 carbon phase is not substantially modified by the indent loading, at the atomistic or at the medium-range (i.e. at the nanoscale) level. However, the amount of graphitic material in this region is strongly increased upon indentation, as indicated by the increase in the I(G)/I(IBM) ratio. We are therefore inclined to conclude that sp^2 carbon is produced from the indented B_4C grains. Finally, the bulk Raman spectra from another indented region corresponding to the lower right corner of the indentation imprint is shown in Figure 29d. Although the D-peak is still present in this region, no real G-peak is present, but a peak above 1700 cm^{-1} is observed.

This peak has been previously reported by others but its origin has been the subject of debate [10, 20-24] [46, 51, 53, 78, 80, 82]. La Salvia *et al.* demonstrated it to be related to the failure of B₄C under ballistic impact. We will discuss this peak below after our discussion of the SERS results.

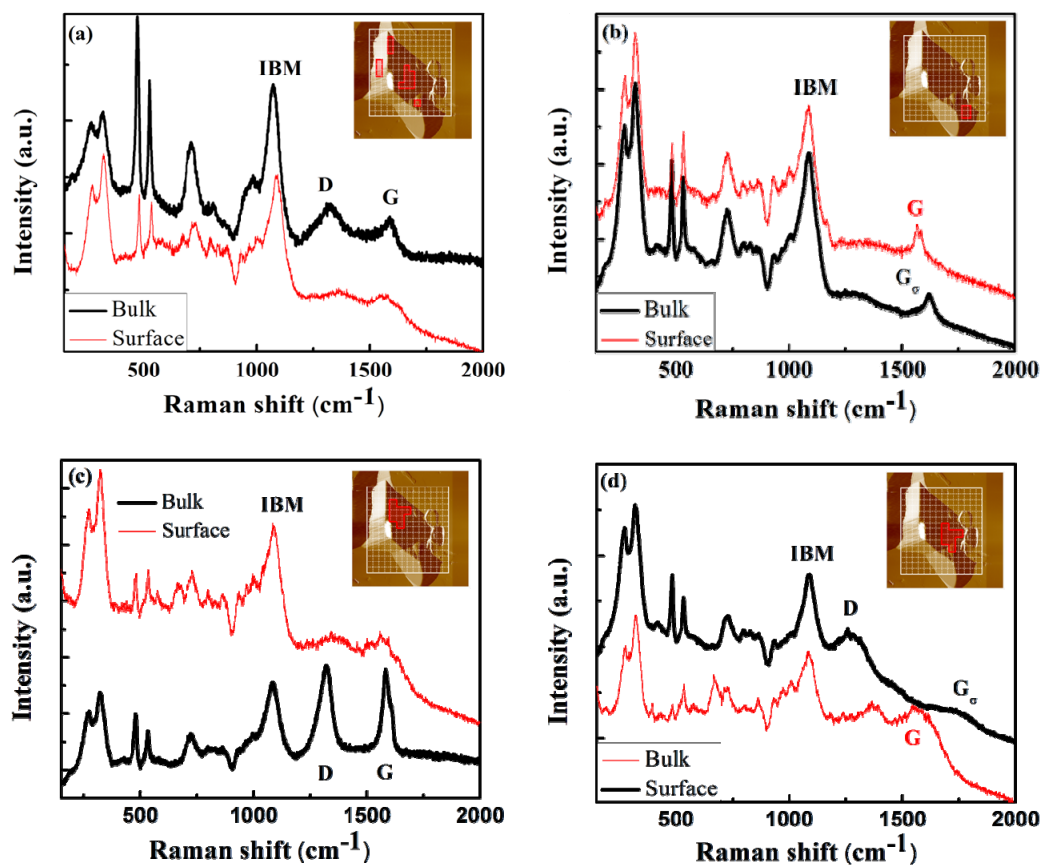


Figure 29. Results from bulk and surface-Raman mapping the “type b” indentation at 300 mg load, with the identification of four broadly homogeneous characteristic regions: (a) region where load produced medium-range ordered nanocrystalline graphite (b) region of medium-range disordered and strongly amorphized graphitic islands (c) large cracks where medium-range disordered olefinic C=C chains are produced (d) comminuted cracks presenting region of medium-range disordered, strongly amorphized graphitic islands under residual stress.

4.3.4 Surface-enhanced Raman spectroscopy (SERS) on the hot-pressed indented sample

In order to contrast the differences between the carbon features in the bulk and surface of the damaged regions, we correlated our bulk Raman results with SERS measurements. Relatively uniform deposition of gold particles on the indented surface (see Figure 28b) as done by simply drop casting. The thin layer of Au nanoparticles strongly changes the appearance of the sample in the optical microscope, emphasizing several surface features, both on pristine and indented regions. No significant difference between the bulk and SERS spectra of the undamaged material was detected. Furthermore, the B_4C peaks from the SERS and bulk spectra also appeared similar. In contrast, dramatic differences in the carbon Raman features can be observed in the indented region, as shown in Figure 29a – 29d. The SERS and bulk spectra highlighting the carbon D and G peaks have been replotted in Figure 30a – 30d for clarification. As discussed above, the bulk spectra shown in black should provide information up to a depth of $\sim 20\ \mu\text{m}$ while the SERS measurements should probe $\sim 5\ \text{nm}$ from the surface. The Raman signal from gold and dispersing agents was generally below the detection limits. Thus, the differences between Raman features detected on the same point before and after deposition of the Au nanoparticles can be attributed to cross-sectional differences in B_4C . The difference between the surface and the bulk is especially clear in Figure 30a, where the SERS shows broad D and G peaks while the bulk spectrum shows reasonably well resolved D and G peaks. This suggests that the bulk sp^2 phase is reasonably well ordered while the surface is amorphous. More specifically, the dimension of the sp^2 aromatic clusters as inferred by eq.(4.1b) on the surface is a few tens of angstroms. It is unlikely that the surface amorphization is a consequence of the cutting or

polishing processes because we observed it only in correspondence of the micro-indentations, while the effect is absent in the undamaged areas of the sample.

Another interesting difference between bulk and SERS spectra is noticeable in Figure 30c and 30d. In both cases, there is a reasonable similarity between surface and bulk spectra but in the latter, the G-peaks are significantly more blue-shifted, indicating olefinic C=C bonds (panel c) and graphitic islands under residual stress (panel d). Curiously, from Figure 30d we can observe that the D-peak significantly blue shifts near the surface, while the G-peak is red shifted. This is consistent with surface-induced stress relaxation. In contrast to the G-peak, which is a zone-center optically allowed Raman feature, the D-peak is an optically-forbidden zone-boundary feature [83] that is double-resonantly enhanced by the electronic structure. The electronic π - π^* interband energies in small aromatic sp^2 clusters are expected to decrease with pressure, as generally happens in semiconductors [84] and recently demonstrated in anthracene [85]. Therefore, the effect of pressure on the frequency of the D-peak is equivalent to the effect of decreasing the Raman excitation energy. Subsequently, the D-peak position is expected to decrease at increasing residual internal stress. This is what we suggest happens when going from surface to bulk Raman spectra in Figure 30d. We conclude that the downshift of the D-peak might further suggest that in these regions the sp^2 carbon domains experience residual stress.

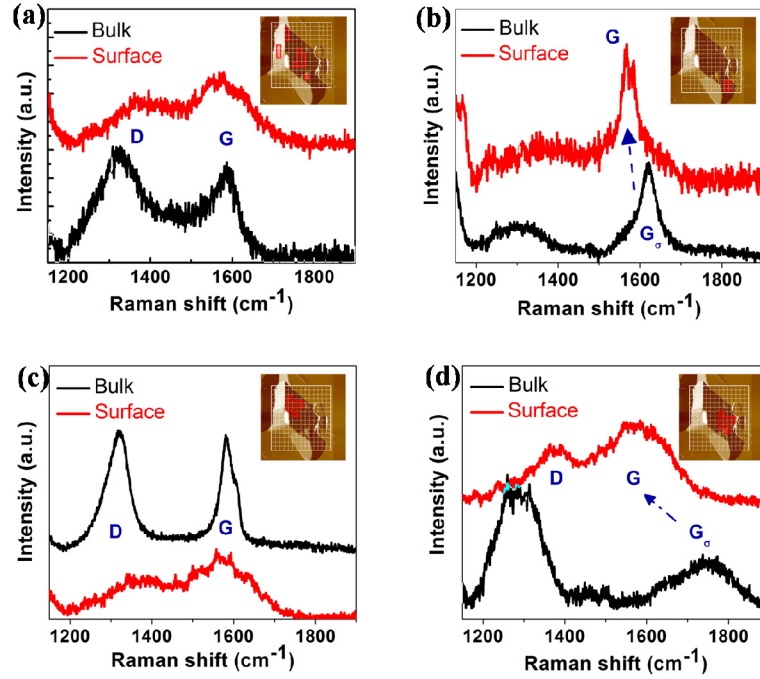


Figure 30. Red lines: results from SERS mapping the “type 2” indentation at 300 mg load, with comparison with the baseline-corrected bulk Raman spectra reported in Figures 29(a-d) (grey lines). In panels a-b, the stronger amorphization of the surface, leading to broader D and G peaks, can be observed. In panels c-d we can observe the stress release on the surface, leading the SERS G_{σ} peaks to recover their ‘usual’ position below 1600 cm^{-1} .

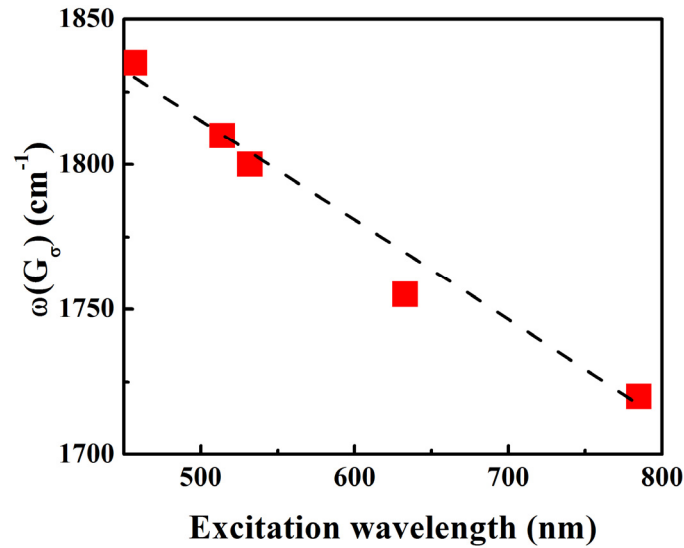


Figure 31. Dispersion for the G-mode under residual stress (G_{σ}) as a function of the excitation wavelength for the map point investigated in Figure 29d and 30d. The mode dispersivity ($\sim 0.5 \text{ cm}^{-1} / \text{nm}$) coincides with that reported in the literature for the G-mode of diamond-like amorphous carbon.

4.3.5 Origin of the dispersive peak between 1700 – 1800 cm^{-1}

The position of the high wavenumber peak as a function of the excitation wavelength was monitored to pinpoint its origin. The peak position as a function the excitation wavelength is shown in Figure 31. It can be clearly seen that the peak is dispersive and the variation of the peak position with excitation energy is generally attributed to the presence of resonant localized π -electronic states in a sp^2 carbon [73]. A similar trend is observed for the G-peak in diamond-like carbon [73]. Indeed, the dispersion of this peak ($\sim 0.5 \text{ cm}^{-1}/\text{nm}$) is similar to that reported in the literature for the G-mode of diamond-like a-C [73]. In contrast, single C-C bonds in diamond [86] and/or amorphous carbon [73] do not exhibit dispersive behavior of the Raman frequencies with the excitation wavelength because they are excited in resonance with extended σ -electronic states [87]. Raman active vibrations from boron carbide are non-dispersive for the same reason since boron carbide does not involve localized π -electrons. Another point strongly suggesting the assignment of the 1700 cm^{-1} peak to π -bonded sp^2 carbons is its disappearance at ultraviolet (UV) Raman excitation, as observed by Ghosh *et al.* [53]. In fact, the intensity of the π - π^* electronic transitions strongly decreases in the UV. The dispersivity of the 1700 cm^{-1} peak suggests that its recent assignment to stretching vibrations of B-C bonds in amorphous boron carbide is unlikely [51]. Therefore other explanations for the origin of the 1700 cm^{-1} peak in damaged B_4C should be explored.

4.4 Summary and Conclusions

We have demonstrated that boron-carbide powder shows microscopically inhomogeneous composition, with variable degrees of two different forms of sp^2 carbon clusters: small inclusions probably localized within the B_4C grains; larger domains, probably located on the grain boundaries. We have demonstrated that both these types of inclusions are present in the starting powders and in the hot pressed samples. Thus, they cannot be the result of hot pressing additives. We have also demonstrated that the behavior of these hot pressed samples under load suggests that they are inhomogeneous at the microscale. In addition, by comparing bulk and SERS Raman spectra recorded at different excitation wavelengths, we were able to show that the $\sim 1700\text{ cm}^{-1}$ peak frequently observed under such conditions is dispersive and maybe related to sp^2 clusters under compression.

| CHAPTER 5 | *IN-SITU* MONITORING OF STRUCTURAL CHANGES UNDER ELECTRICAL FIELDS

In-situ monitoring of the transformation of B₄C under electric field using Raman spectroscopy is reported in this chapter as non-destructive method to evaluate boron carbide samples. Application of electric fields up to 5000 V/cm leads to local segregation of carbon, indicated by the appearance of Raman D and G peaks. At low electric fields (< 3000 V/cm), the segregated carbon is amorphous while at higher fields, aromatic sp² clustering is observed. Electrical measurements as a function of temperature are used to compliment the Raman measurements. The results demonstrate that it is possible to induce transformations in boron carbide using electric fields that are comparable to those obtained under shock and nanoindentation.

5.1 Phase Transformations of Boron Carbide

The high hardness (~ 30 GPa) and Hugniot elastic limit (HEL $\sim 17 - 20$ GPa), along with low density, of hot pressed boron carbide (nominally B_4C) [4] make it an ideal material for ballistic armor applications. In addition, boron carbide possesses the highest dynamic elasticity of ceramic materials [88]. Although these properties would suggest that boron carbide could withstand high velocity impacts, this has not been observed. The absence of residual plastic strength above the HEL, a compulsory requirement for armor survival upon damage, is thought to be the primary reasons for failure of boron carbide at lower than expected impact rates and pressures. This behavior is unique in dynamically elastic materials finding counterparts only at much lower stress values (<1 GPa) in dynamically inelastic ionic insulators, such as quartz and glasses [42, 48]. TEM investigation by Chen *et al.* revealed 2–3 nm shock induced amorphization bands along the (113) crystallographic plane in impact tested boron carbide [1]. However, no explanation for the origin of these amorphous bands was offered in that report [1]. Our theoretical study revealed that the failure of B_4C is commensurate with the segregation of boron icosahedra embedded in amorphous carbon in 2–3 nm wide amorphous bands along the (113) crystallographic plane [2].

In impact studies [1], postmortem analysis of failed material is usually conducted. Alternatively, Domnich *et al.* [46] utilized *ex-situ* Raman measurements to characterize local amorphization induced by nanoindentation. Ge *et al.* [89] demonstrated similar effects in scratch debris on boron carbide. It was also shown in Ref. [89] that annealing of the scratch debris led to D and G features that were similar to sp^2 rich amorphous carbon (a-C), suggesting clustering. Recent work has suggested that these clusters may also

contain boron (i.e. the material is actually a-C:B) [53]. In addition, Ge *et al.* [89] detected π -bonded electrons by electron-energy loss spectroscopy, an indication of the presence of sp^2 bonding. In addition to the D and G features, a number of papers [46, 51, 53, 89] also reveal a Raman feature at ~ 1800 - 1850 cm^{-1} under pressure or after indentation. The peak has been identified at 1810 cm^{-1} by Domnich *et al.* [46] when using 514.5 nm Raman excitation.

Recently, La Salvia *et al.* [78] demonstrated that impacted boron carbide samples exhibited peaks at 1330 cm^{-1} , 1580 cm^{-1} and $\sim 1750\text{ cm}^{-1}$ using a 785 nm Raman laser. The position of the high-frequency peak on impacted samples was lower than in indented samples (i.e. $> 1800\text{ cm}^{-1}$). However, the discrepancy can be explained by the fact that La Salvia *et al.* used an infrared (785 nm) laser for the Raman measurements while the indent-induced peak at $\sim 1800\text{ cm}^{-1}$ has been generally observed at shorter (i.e. visible-light) excitation wavelengths. In fact, Raman measurements on micro-indented samples recently performed by our group [90] show that the indent-induced feature observed at ~ 1810 - 1830 cm^{-1} at blue-green excitation is dispersive and strongly downshifts (to 1700 cm^{-1}) at longer excitation wavelengths.

Real time Raman characterization could provide valuable insight into why B_4C fails prematurely in dynamic tests. In this work, we show that amorphization in B_4C occurs by the application of relatively low electric fields. By applying pulses of increasing voltage and simultaneously monitoring changes with Raman spectroscopy (Figure 32A), it is possible to observe not only the onset but also the degree of sp^2 clustering in real time. Furthermore, through electrical measurements as a function of temperature in conjunction with Raman spectroscopy, we are able to determine that

above a critical electrical field, amorphization leads to partial collapse of the B_4C structure.

5.2 Experimental Details of the samples

Highly polished hot pressed boron carbide with a density close to 100% provided by an industrial supplier was used in this study. The samples were obtained by cross-sectioning a 1 mm-thick central section of a 2.5 by 2.5 cm hot-pressed tile. The sample surface was further polished until graphite from the surface was eliminated. There was no significant difference in the Raman spectra obtained from the starting powder (B_4C stoichiometry) and the samples. In addition, there was no contribution to the Raman spectra from the additives used during hot pressing.

The electrical Raman measurements were performed on a Renishaw InVia Raman spectrometer at an excitation wavelength of 785 nm. Gold electrodes (width 1 mm, channel lengths of 20 μm) were defined on each substrate using a shadow mask. External voltage pulses of 0-10 V (leading to electric fields, E_{ext} , from 0 – 5000 V/cm) were applied for 120s to the electrodes during the Raman measurements using a GW GPS-1850D stabilized power supply. Each series of Raman spectra at varying voltage were recorded on the same spot in order to obtain comparable signal intensities. In order to eliminate the possibility of Raman laser induced transformation, we performed similar measurements in the absence of an electric field which did not show a variation of the spectra with time. The results discussed here are representative of what is observed on a large number of B_4C samples.

5.3 Results and Discussion

The Raman spectra of hot pressed B₄C, recorded *in-situ* during application of increasing electric field pulses are shown in Figure 32B and 32C. Two primary effects on the Raman spectra with increasing electric fields are evident. First, the decrease in the intensity of the B₄C related Raman modes (frequencies ranging from 275 cm⁻¹ to 1100 cm⁻¹ [21, 79]) can be seen; Second, the strong increase of the D (~1300 cm⁻¹) and G (~1600 cm⁻¹) carbon modes under voltage pulses can be observed in Figure 32C. It is also clear in Figure 32C that very weak carbon D and G modes are present in the sample even before electric field is applied. We attribute this to the precipitation of carbon in grain boundaries during densification or to the presence of disordered carbon in as-synthesized powder, as recently reported [70].

In Figure 32C, the Raman modes in the 1200-1700 cm⁻¹ range strongly increase in intensity with electric field strength, especially between 1500 and 3500 V/cm where the intensity of the B₄C modes (Figure 32B) was observed to decrease. Furthermore, the broad line widths of the peaks indicate the presence of disordered or amorphous carbon domains, rather than ordered graphite [73]. If we tentatively assign the two features at ~1350 and 1580 cm⁻¹ to the D and G peaks related to sp² clusters of a-C(:B), then the data in Figure 32C reveals that the D peak increases faster in area and intensity than the G-peak, leading to an increase in the D/G ratio. Since the D/G intensity ratios in amorphous carbon are proportional to the size, L, of the sp² cluster domains through the relationship $I_D/I_G \sim L^2$ [73], it can be inferred that the island sizes increase with electric field. As these clusters are aromatic, a similar model valid for amorphous carbon nitride [91] should also apply to boron-containing a-C as we have observed in a separate study

[90]. In addition, Figure 32D shows the ratio of $I(D)/I(G)$ vs. applied electric field. As the D peak arises from aromatic rings so that for a fixed wavelength, $I(D)/I(G)$ should increase with increasing disorder [73].

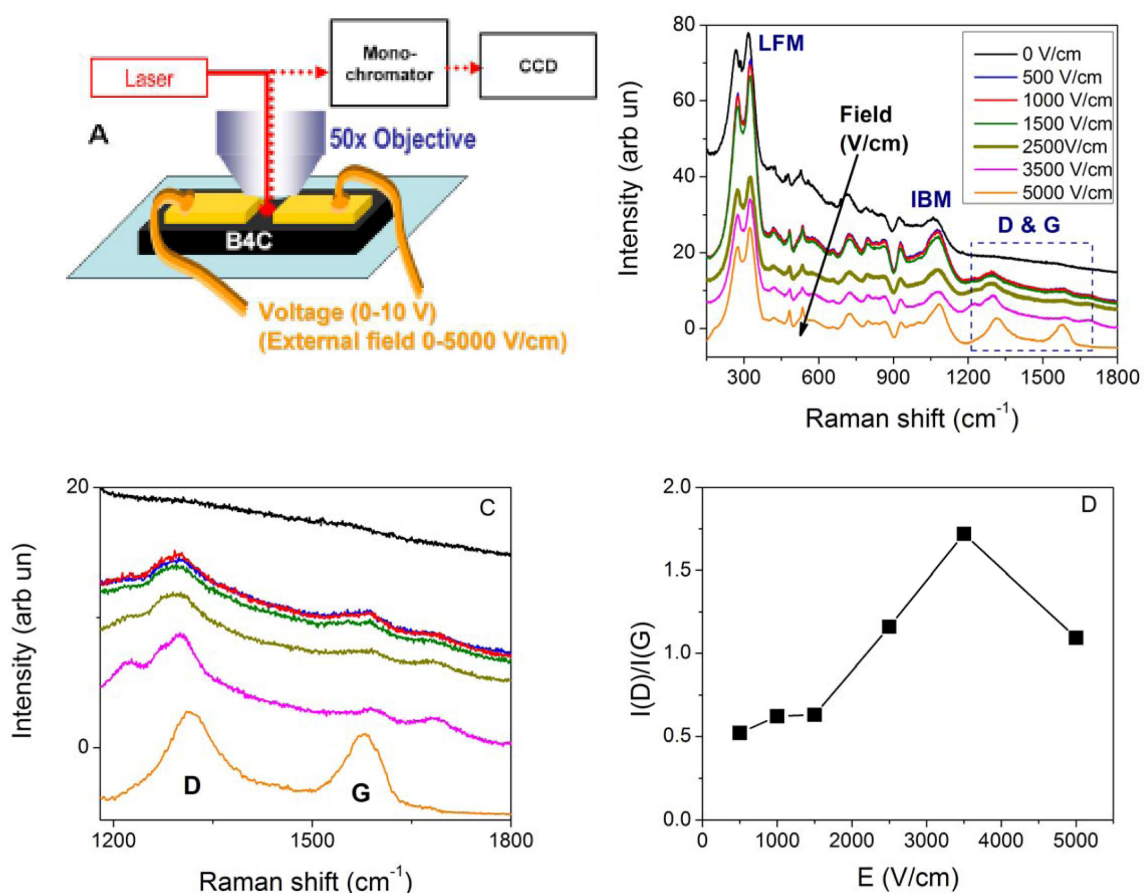


Figure 32. (A) Schematic of the apparatus used for in-situ Raman investigation of boron carbide under electric field. Raman spectra as a function of the electrical field showing the (B) entire frequency range, including the boron carbide modes and (C) detailed plot of the frequency region where the carbon D and G peaks are present and (D) the ratio of $I(D)/I(G)$ vs. applied electric field.

In addition to the D and G modes, supplementary peaks at approximately 1250 cm^{-1} and 1700 cm^{-1} are also present in Figure 32C. Yan *et al.* [51], using a shorter Raman excitation wavelength ($\lambda = 514.5 \text{ nm}$), observed a similar feature at higher frequency ($>1800 \text{ cm}^{-1}$). Also a feature at similar position was also detected by Ghosh *et al.* [53]

who suggested that it may be related to a mixed amorphous carbon-boron phase. Using infrared excitation wavelength, La Salvia *et al.* [78] noticed a peak at $\sim 1750\text{ cm}^{-1}$ after the failure of B_4C under ballistic impact. No G-peak or other peaks at $1580\text{-}1600\text{ cm}^{-1}$ was present, although a peak at $\sim 1300\text{-}1350\text{ cm}^{-1}$ (i.e. close in frequency to the carbon D-peak) was detected [78]. We will further clarify the origin of this peak in future work [90]. However, the detection of the high frequency feature between 1700 cm^{-1} and 1850 cm^{-1} may suggest that failure by nanoindentation, ballistic impact, and electric field pulses are due to related mechanisms.

At the maximum applied electric field (5000 V/cm), narrow D and G bands indicative of highly sp^2 rich amorphous carbon with relatively large aromatic clusters appear [73]. The presence of the G and D peaks and the disappearance of the subsidiary bands at 1250 and 1700 cm^{-1} indicate that aromatic amorphous carbon clusters are present. Indeed, the spectra at 5000 V/cm resemble those obtained by Ge *et al.* [89] after annealing the scratch debris from boron carbide single crystals. We therefore conclude that application of sufficiently large electric fields leads to carbon segregation and onset of aromatic sp^2 clustering in boron carbide.

In order to further analyze the structural changes in B_4C observed with Raman spectroscopy, electrical measurements at room and higher temperatures were performed by applying $1 - 10\text{ V}$ pulses across $20\text{ }\mu\text{m}$ Au gap cells using a GW GPS-1850D stabilized power supply. A programmable HP 4140B Picoammeter / Voltage source was used to measure its sheet conductance. The sample was heated in air by means of a Bayz Thermopad microheater. A thermocouple on the sample surface was used to record the temperature.

The room-temperature sheet conductance measured *in-situ* while recording the Raman spectra is shown in Figure 33A. The increase in conductance is an indicator of sp^2 clustering in B_4C , as confirmed by electrical measurements at higher temperatures. Typical electrical data as a function of temperature of the B_4C samples are shown in Figure 33B. The temperature behavior of electrical conductivity in B_4C at $T = 300-600$ K has been explained by Emin and coworkers [92, 93] in terms of bipolaronic hopping between charged icosahedra (i.e. tunneling of both positive and negative charges through the icosahedra, activated by lattice vibrations). The expression of the conductance is therefore [92, 93]:

$$S = A/T \cdot \exp(-E_{act}/k_B T) \quad (5.1)$$

where the prefactor A in high purity $B_{4+x}C_{1-x}$ is found to depend on the carbon content, $1-x$. Emin and coworkers found that A decreases by approximately one order of magnitude when going from B_4C to B_9C [92]. Furthermore, since the theory indicates that the prefactor is related to the average distance r between charged icosahedra ($A \sim r^{-1}$ [92]), any decrease of A reflects a lower icosahedron-icosahedron distance. At increasing boron content, this occurs because the chains connecting the icosahedra are progressively suppressed and the structure approaches that of boron, where icosahedra are closer.

In our case, the activation energy E_{act} depends on the size β of the potential well occupied by the polaron [92] according to

$$E_{act} \sim \beta^{-6} \quad (5.2)$$

In the absence of lattice degradation β can be envisaged as the diameter of the icosahedra. In such a case, the E_{act} is independent of the composition ranging from B_4C to B_9C . Rather, it has been suggested that the activation energy for electronic conduction is more closely related to the presence of impurities and imperfections which act as further hopping sites [92].

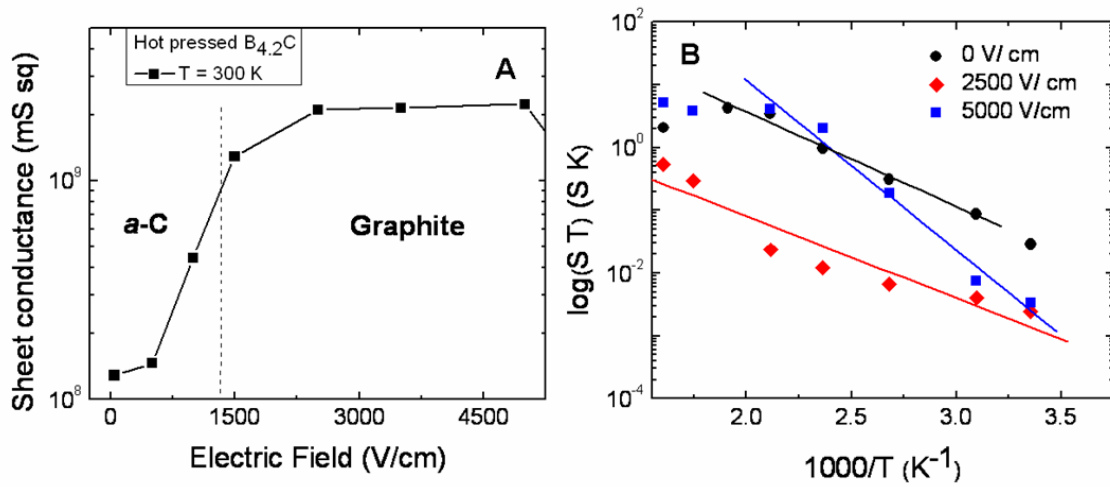


Figure 33. (A) Sheet conductance of the boron carbide sample as a function of the applied electric field at room temperature. At low fields (below 3000 V/cm), the increase in conductance is attributed to the formation of an amorphous a-C(:B) phase while at higher fields significant sp^2 clustering leads to a substantial increase of the aromatic cluster size. (B) Arrhenius plot of sheet conductance as a function of temperature at three different electric fields.

The prefactor and activation energy values (A and E_{act}) obtained in our work are plotted in Figure 34A and 34B. It can be observed that, for pulses below 3000 V/cm (corresponding to the regime of small or moderate segregation of amorphous carbon as detected by Raman), the prefactor decreases only slightly. This can be due to amorphization which could be responsible for the observed changes in the Raman spectra. Within this regime, we find that the activation energy remains constant at

approximately $E_{\text{act}} \approx -0.15 \pm 0.03$ eV. This value is very similar to that found by Emin and coworkers [92, 93], irrespective of the stoichiometry of the $B_{4+x}C_{1-x}$ samples hot pressed in vacuum (10^{-5} - 10^{-6} Torr) at 2400K from high purity boron and carbon powders (B impurities below 30 ppm and C impurities below 10 ppm). This suggests that at electric fields below 3000 V/cm, the electrical transport mainly occurs through the boron carbide phase even though the Raman indicates the presence of free carbon.

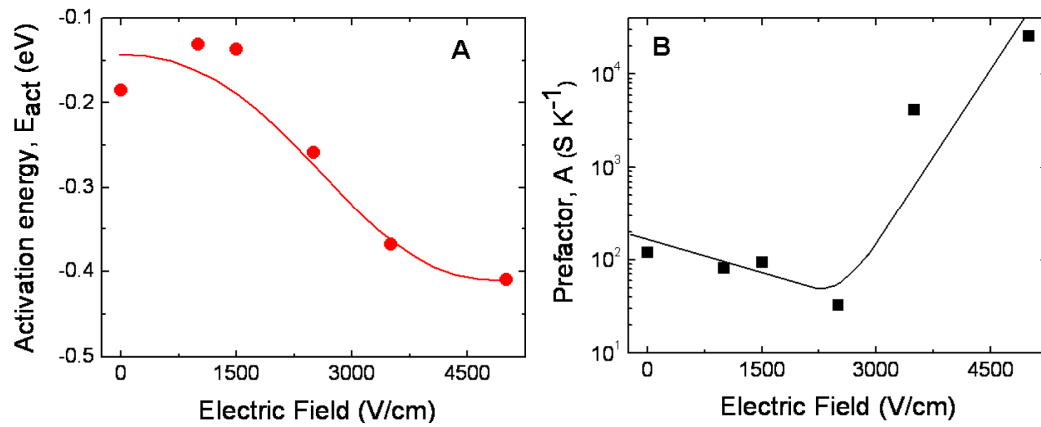


Figure 34. Plot of (A) activation energy and (B) prefactor as a function of the electric field strength.

For electric fields above 3000 V/cm, corresponding to significant formation and/or segregation of amorphous carbon clusters, the prefactor A increases with electric field strength. The activation energy trend is similar. The maximum E_{act} was measured to be -0.41 eV, an unexpectedly high value for boron carbide [92, 93], but consistent with hopping processes between nearest neighbor sp^2 cluster islands in amorphous carbon [94]. In amorphous carbon, the conductivity can be described by eq. (1), albeit the physical meaning of the activation energy and the prefactor are different [94]. E_{act} now represents the energy difference, with respect to the Fermi level of the defective

electronic levels related to the presence of sevenfold or fivefold rings in the sp^2 cluster domains, while the prefactor assumes the form

$$A' \sim r'^2 \exp(-2r' / L) \quad (5.3)$$

Where L is the sp^2 domain size and r' is the hopping distance between nearest neighbor sp^2 cluster domains. Hence, a strong increase of the prefactor occurs when sp^2 clusters are generated and/or they increase in size and tend to coalesce.

This is exactly what we have observed in our *in-situ* structural analysis with Raman spectroscopy. The charge transport mechanism obtained from conductivity versus temperature measurements is consistent with the fact that the application of voltage pulses of increasing electric field leads to the collapse of the B_4C structure. The transformation appears to occur sharply above a critical field of 3000 V/cm. Below this electric field value, Raman indicate the formation of amorphous phase but the prefactor (A) and the activation energy of charge transport show that the B_4C structure is essentially preserved. This suggests that the enhancement in conductivity and the D/G ratio may be due to intra-granular segregation of carbon. Above 3000 V/cm, substantial segregation of amorphous carbon via an increase of the D/G ratio and the conductance can be inferred. Furthermore, at the maximum applied electric field of 5000 V/cm, relatively large size of the segregated sp^2 clusters can be inferred from Raman. In addition to the Raman data, the continuous increase in the activation energy and a sharp rise in the prefactor above 3000 V/cm indicate a dramatic change in the transport properties. The high prefactor and activation energy measured at the maximum applied field are consistent with the formation of large number and bigger sp^2 clusters and

increased hopping between them, respectively. Thus, the structural changes obtained by Raman and transport data (prefactor and activation energy) are consistent with the local amorphization of B_4C with the application of electric fields. Since the presence of free carbon in our pristine samples was low, we believe that electric-field induced amorphization is an intrinsic effect of B_4C . However, we cannot rule out the possibility that pristine intra-granular carbon (which is a general feature of virtually all armor-grade B_4C samples [70]) locally acts as a “seed” for aggregation and clustering for the electric-field induced sp^2 amorphous phase.

5.4 Conclusion

In summary, we observed that electrical field pulses in boron carbide produce effects that appear to be similar to those induced by mechanical stress or shock impact. Specifically, amorphization and eventually large amorphous carbon clusters were detected using Raman spectroscopy during the application of pulses. The Raman features we measured as a function of the electric field could be similar to those obtained under shock or nanoindentation, although more detailed work is needed for confirmation. We have correlated our *in-situ* Raman analysis with charge transport measurements which are consistent with disruption of the boron carbide structure and production of sp^2 amorphous carbon clusters.

| CHAPTER 6 | SYNTHESIS AND SILICON DOPING OF BORON CARBIDE NANOWIRES

The growth of Boron Carbide (B_4C) nanowires and nanostructures using solid-liquid-solid synthesis method is reported in this chapter. A systematic study to investigate the influence of growth parameters such as boron to carbon (B:C) ratio, temperature, catalyst composition and Si-doping on the types of nanostructures formed has been conducted. Specifically, growth at three different temperatures (1000, 1150 and 1250°C), was studied. The diameter of the nanostructures varied widely, ranging from 5 nm to 2 μ m. The lengths of the nanowires were found to vary from several microns up to a few millimeters. In addition to pristine B_4C nanostructures, influence of Si-doping on the growth characteristics of the nanostructures was investigated. Based on our detailed study using scanning electron microscopy, transmission electron microscopy, electron energy loss spectroscopy, energy dispersive spectroscopy and thermal gravimetric analysis, we propose a preliminary model for the growth mechanism of B_4C nanostructures.

6.1 Nanowires and Nanostructures of Boron Carbide

Boron carbide (B_xC) is a unique material consisting of phases with carbon concentrations ranging from 8 to ~20 atomic percent [26]. Despite this broad variation in carbon content, the stoichiometry of boron carbide has a negligible effect on its crystallographic structure. The unit cell of boron carbide consists of a twelve atom icosahedron linked to a three-atom chain with negligible variations in lattice and translation vectors. Differences in composition can be explained by the three-center nature of icosahedral bonds involving boron, which allows for the substitution with carbon atoms [1, 95]. Since boron has one less electron, changes in stoichiometry can significantly influence material properties such as hardness and electrical conductivity [1, 26, 95]. These peculiar features of boron carbide make it useful for a variety of applications. For example, boron carbide possesses high hardness, low density and a high Hugoniot elastic limit, which make it ideal for personnel ballistic armor applications. Boron-rich boron carbide is also potentially useful for thermoelectric and other electronic applications [1, 4, 9, 26, 95, 96].

A similar range of properties can also be expected in boron carbide nanostructures at different carbon contents. Nanowires (NWs) with fixed B_4C stoichiometry have been synthesized using several methods such as plasma enhanced chemical vapor deposition (PE-CVD), thermal evaporation of C/B/ B_2O_3 powder and reaction of carbon nanotubes with boron oxide vapor [22, 97-99]. Other methods include carbothermal synthesis through the vapor-liquid-solid (VLS) growth mechanism and pyrolysis of organic precursors [100-103]. A more recent report by Han *et al.* involves the synthesis of Si-doped B_4C NWs by solid-liquid-solid mechanism (SLS) [104].

Despite this large variety of synthesis mechanisms, nanostructures of B_xC have not been widely reported and a systematic study of their characteristics upon deposition at different carbon content is still lacking. The aim of this work is to understand the phenomena underlying the synthesis of B_xC NWs as a function of the relevant growth parameters: boron to carbon ratio in the precursors and temperature, with emphasis on growth rate, quality of growth products and characteristics of the nanowires. The effect of the addition of small amounts of silicon will also be explored since recently silicon addition has been shown to influence the growth of B_4C nanowires [104].

6.2 Synthesis Method and Characterization Techniques

6.2.1 Synthesis

Different ratios ($B:C = 1:0.25, 1, 4$ and 8) of sub micron boron (Sigma Aldrich, purity $\sim 99\%$, initial particle size $0.82\ \mu m$) and activated carbon (Norit America Inc., purity $\sim 99\%$, initial particle size $5\ \mu m$) were used as the starting materials for the growth of boron carbide (B_4C) NWs. For Si-doped B_4C NWs, Si powder (2 wt. %, Sigma Aldrich, purity $>99\%$, initial particle size $4.27\ \mu m$) was added. A mixture (1 wt. %) of Nickel Boride (NiB , Alfa Aesar, purity 99%, initial particle size $500\ \mu m$), Nickel Diboride (NiB_2 , Alfa Aesar, purity 99%, initial particle size $500\ \mu m$) and Cobalt (Co, Alfa Aesar, purity 99.8%, initial particle size $1.6\ \mu m$) was used as catalyst for the formation of NWs [105]. The metal borides have significantly lower melting temperatures and subsequently result in large growth of B_4C NWs at relatively low temperatures. The components and catalyst were mixed together and thoroughly grounded using an agate mortar and pestle. The reactant mixture was placed in a 10 mL

alumina combustion boat which was inserted into a 99.8 % dense alumina tube (length = 70 cm, inner diameter = 6.35 cm) in a clam furnace. The powder mixture was heated to different temperatures (1000, 1150 and 1250 °C) and held for 1 hour in argon at a pressure of 1 atm.

6.2.2 Characterization

Subsequent to the synthesis of the nanostructures, a suite of analytical techniques was used to characterize them. The amount of residual carbon and other volatiles were estimated using a thermal gravimetric analyzer (TGA 7, Perkin Elmer) by heating the collected powder at a rate of 10 °C/min in air. The morphology of the various as-synthesized structures was also observed by scanning electron microscopy (FESEM, FEI XL-30). The elemental composition of the nanostructures and the overall product was obtained by energy-dispersive x-ray spectroscopy (EDS, EVEX) and electron energy loss spectroscopy (EELS). EELS spectrum imaging was conducted using Philips CM200 FEG-TEM/STEM equipped with Gatan Imaging Filter (GIF) operating at 200 kV. All spectra were collected and processed with Emispec Vision and also exported to further analysis with Gatan EL/P software. Finally, high resolution transmission electron microscope (TEM, TOPCON 002B operated at 200 kV equipped with EDS attachment) was utilized to confirm the existence, crystal structure, morphology and chemistry of the NWs and nanostructures.

6.3 Parametric Study for the Growth of Boron Carbide Nanowires

6.3.1 *Effect of Boron to Carbon Ratio*

The effect of the B to C ratio at a constant temperature of 1250 °C on the as synthesized structures is demonstrated in Figure 35. For each composition, a low magnification along with a high magnification SEM images in the inset are shown. Boron carbide wires with a distribution of diameters produced from low B to C ratio (1:0.25) are shown in Figure 35a. The large wires are up to a micron in diameter and tend to be bamboo-shaped with visible circumferential stacked struts around the diameter. Within the space between these large wires, smaller diameter (20-100 nm) and shorter curly nanostructures (100-500 nm) can be seen. The origin of the bamboo-like structure and the structure of the smaller nanowires will be discussed later. An advantage of using low carbon composition precursor is that it lowers the amount of residual carbon in the end product. When the ratio was increased to 1:1 the wires appear to be straighter and there was some evidence of the formation of nanobelts, as shown in Figure 35b. The diameter of these wires was ~100 nm with lengths of 10-100 μm . In Figure 35c, for B:C ratio of 1:4 the structures are comparable to other compositions except the fact that some of the large wires appear to be decorated with nanostructures. There was no evidence of such decorations for lower boron to carbon ratio. As the amount of B:C ratio was increased to 1:8, long wires (up to 100 μm) with diameter ranging from 100 nm to 1 μm were observed, as shown in Figure 35d, consistent with previous works on metal carbide whiskers which reported that the increase in carbon content tends to make the whiskers and wires grow longer [106, 107]. In order to confirm the presence of B_4C nanowires and

distinguish them from carbon nanotubes that might have formed at high B:C ratios, the samples were subjected to TGA in air with temperatures in excess of 600 °C. No decomposition of the nanowires was observed indicating the presence of B:C structures. It is well known that carbon nanostructures begin to oxidize at 300-400 °C; the lack of decomposition of B:C product indicates that the structures shown in Figure 35 are unlikely to be carbon nanotubes [108]. Furthermore, it was confirmed by EDS that the wires and nanostructures consisted of boron and carbon.

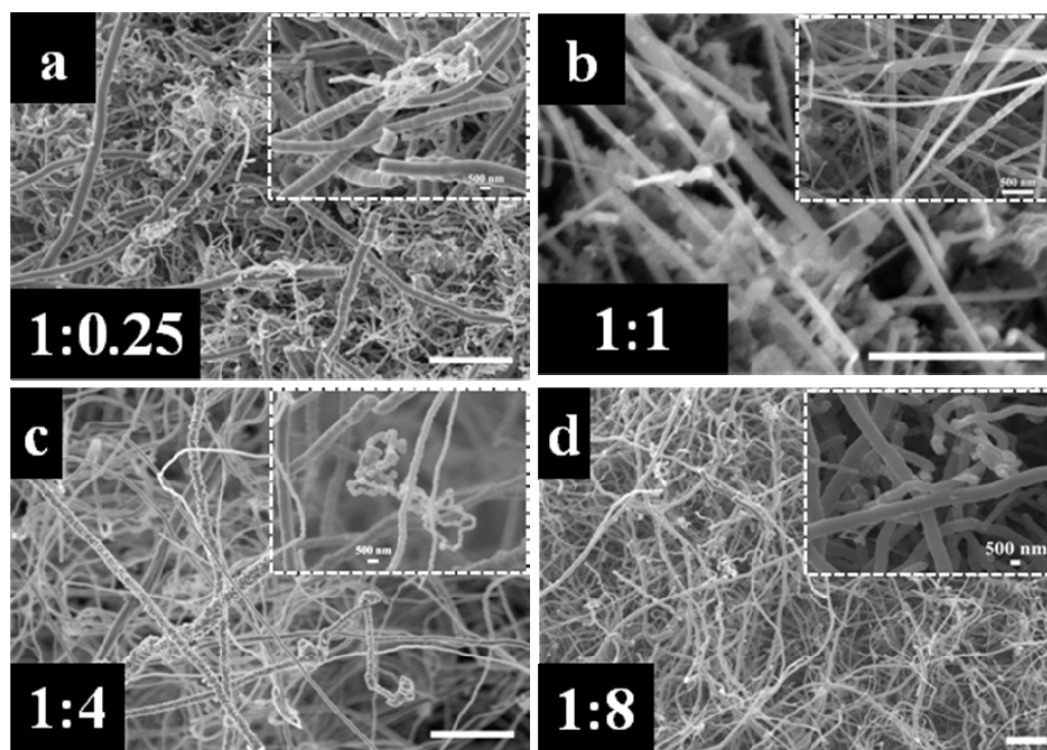


Figure 35. SEM images of the B_4C nanostructures with varying B to C ratio along with diameter distribution of B_4C NWs and nanostructures. Figures a to d correspond to different B to C ratio i.e. a) 1:0.25, b) 1:1, c) 1:4, and d) 1:8 and temperature of 1250 °C (Scale bar 10 μ m).

6.3.2 *Effect of Temperature*

The temperature of synthesis was chosen based on the eutectics of B and C with NiB, NiB₂, Si and Co [109-111]. The effect of the growth temperature on the morphology and yield of boron carbide nanostructures is demonstrated in Figure 36. Figure 36 a-d represent growth at 1150 °C while Figure 36 e-h correspond to 1250 °C. No significant growth of the nanostructures was obtained for temperatures under 1000°C. An increase in the amount of nanostructures was observed when the growth temperature was raised to 1150°C and 1250 °C.

A low synthesis temperature of 1150°C, along with a low boron to carbon ratio (1:0.25 and 1:1) resulted in little nanostructure growth, as shown in the Figures 36a and 36b. Although the nanowire content was low, clear evidence of the tip growth of small diameter (20 to 100 nm) and short lengths (200 to 800 nm) can be seen in Figure 36b. However, when the synthesis temperature was increased to 1250°C while keeping the B:C ratio at 1:0.25, increased amounts of wires with diameters ranging from 20-500 nm were obtained. The 1250°C growth for these two B:C ratios are shown in Figure 36e and 36f. The distribution of the lengths of the nanostructures was variable, ranging from tens of nanometers to several microns. At higher B:C ratios of 1:4 and 1:8, the growth at 1150°C resulted in the synthesis of more uniform wires, as shown in Figure 36c and 3d. Specifically, the wires are more uniform in diameter (~300 nm for Figure 36c and ~2 µm in Figure 36d) although the distribution is still large for the B:C ratio of 1:4 compared to B:C ratio of 1:8. Furthermore, NWs grown at 1150°C and B:C ratio of 1:4 (Figure 36c) appear to be curly and disordered in contrast to the NWs grown at a B:C ratio of 1:8

(Figure 36d), which are straight. At the higher temperature of 1250°C, the B:C ratio of 1:4 yields nanostructures with decorations, as mentioned previously in Figure 35. It can be seen from Figure 36g that the synthesized product consists of long decorated wires along with thin wires (diameter ~500 nm). At 1250°C and B:C ratio of 1:8, wires of diameters of 2 to 4 μm can be clearly seen (Figure 36h) but in contrast to the growth at 1150°C, the wires are less straight and consist of a wider diameter distribution. To summarize, the best wires in terms of the yield and crystallinity were obtained at 1150°C and B:C ratio of 1:8 (Figure 36d).

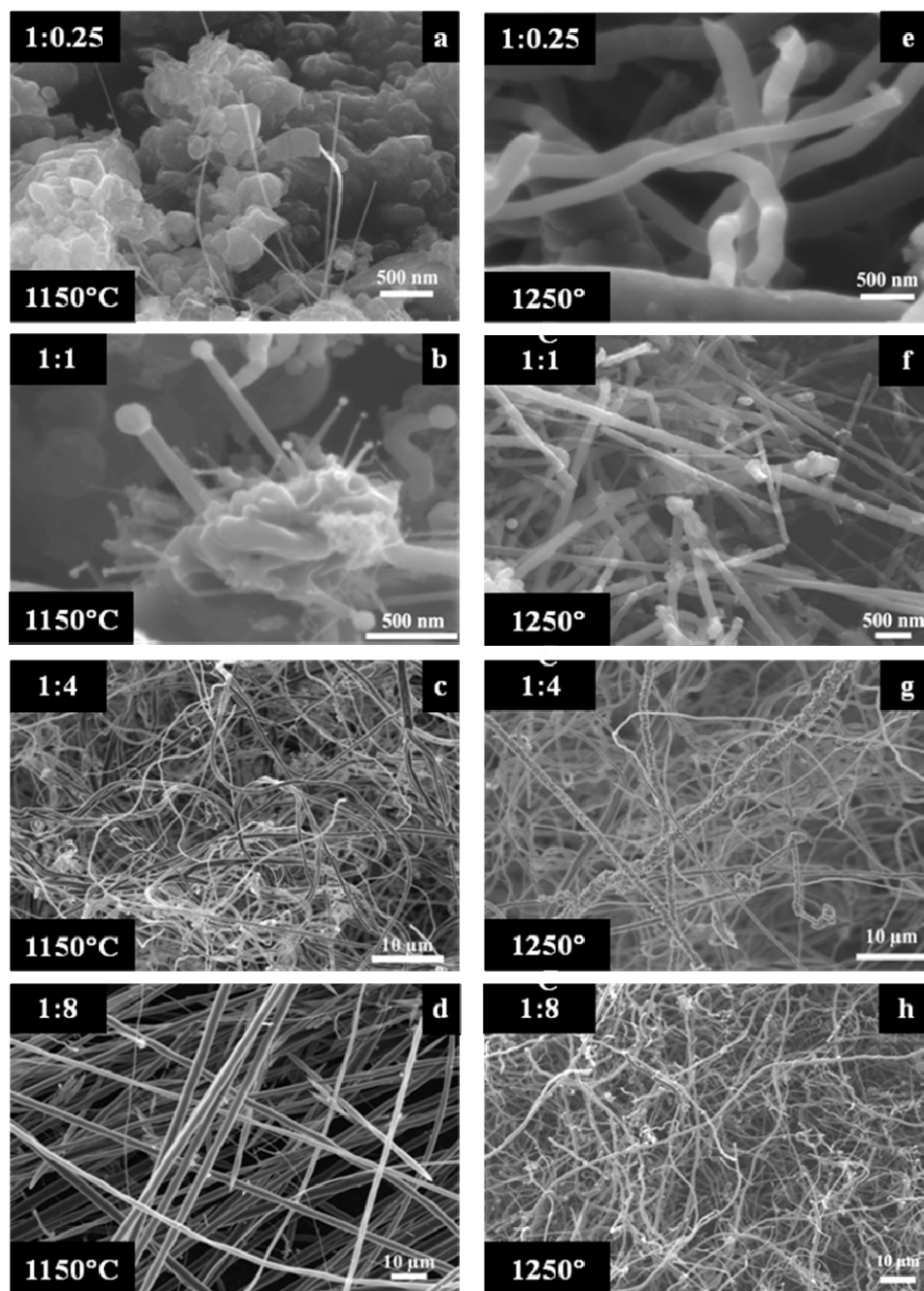


Figure 36. SEM images showing the effect of temperature on the growth and morphology of nanostructures when the temperature was varied from 1000 °C (during which no growth was observed) to 1250 °C. Figure a, b, c and d correspond to a temperature 1150 °C and e, f, g and h to 1250 °C. More specifically (a) B:C ratio = 1:0.25 at 1150°C, (b) B:C ratio = 1:1 at 1150°C, (c) B:C ratio = 1:4 at 1150 °C, (d) B:C ratio = 1:8 at 1150 °C and (e) B:C ratio = 1:0.25 at 1250°C, (f) B:C ratio = 1:1 at 1250 °C, (g) B:C ratio = 1:4 at 1250 °C, (h) B:C ratio = 1:8 at 1250 °C.

In order to obtain more insight into the structure of boron carbide nanowires, especially the origin of the bamboo structure in Figure 35a and the decorations observed on some structures (see example in Figure 35c and 36g), we performed high resolution TEM of boron carbide NWs, as shown in Figure 37. Firstly, the TEM analysis reveals that nanowires of B_4C are synthesized along with larger structures which are seen more predominantly in SEM images. The distribution of diameters can be readily observed in Figure 37a, where small nanowires of ~ 10 nm in diameter can be seen at the bottom left and right corners of the image along with a larger NW of diameter of ~ 120 nm for growth at B:C ratio of 1:1 at 1150°C . The presence of the catalyst nanoparticles at the tips of the NWs is marked by arrows in all images containing nanowires. Examples of single, straight nanowires indicating tip growth are shown in Figure 37b.

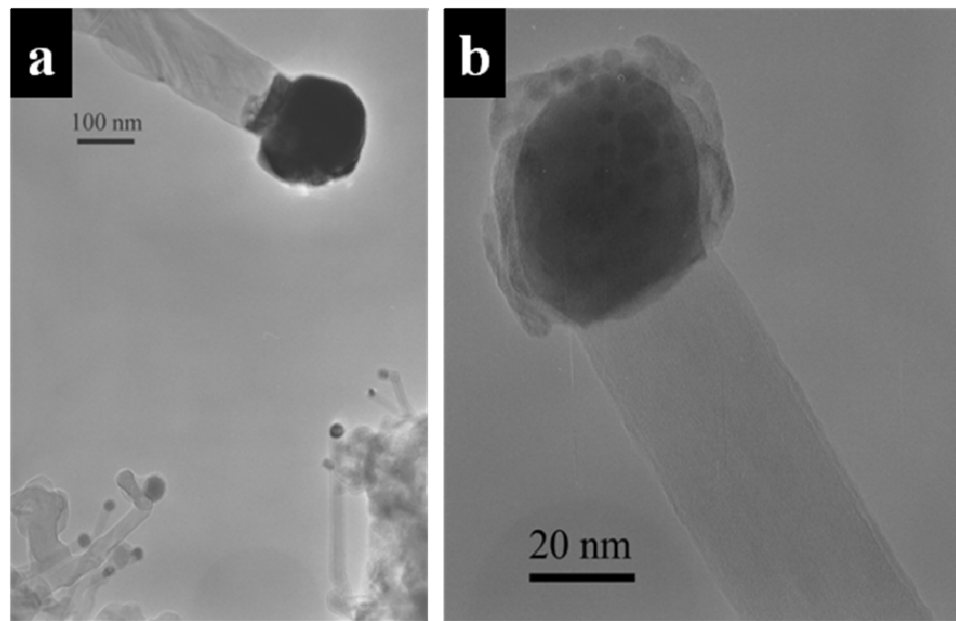


Figure 37. TEM images showing morphology, size and presence of catalyst particles (arrows) in different boron carbide nanowires and nanostructures. a) Indicates the presence of different diameters and b) shows an example of a long, straight nanowire along with a diffraction pattern indicating the single crystalline nature. The growth condition for a) and b) B:C ratio = 1:1 at 1150°C .

6.3.3 Effect of addition of Silicon

2 wt. % Si was added to the precursors for different B:C ratios and temperatures to evaluate the effect of Si on B_xC NWs. The various structures obtained with Si addition are shown in Figure 38. The insets are higher magnification versions of the larger images. We found that at a lower B to C ratio of 1:0.25 at 1250°C with silicon favors the formation of long and straight wires (diameter of $\sim 1\ \mu\text{m}$) as shown in the Figure 38a. An increase in the B to C ratio resulted in the formation of belts and strips (dimensions = 300-500 nm) as shown in Figure 38b. A further increase in the B:C ratio resulted in the formation of nanowires decorated with beads which are likely to be catalyst particles (refer TEM analysis shown above), as shown in Figure 38c. Our EDS analysis shows that the beads contain excess Si which moves the composition of the catalyst away from the eutectic point so that the particles are not involved in the growth process and simply decorate the sidewalls of the grown structures. At high B:C ratio of 1:8, long wires (up to 200 μm in length and $\sim 1\ \mu\text{m}$ in diameter) surrounded by disordered and curly nanostructures (diameter 500-600 nm) are formed, as shown in Figure 38d.

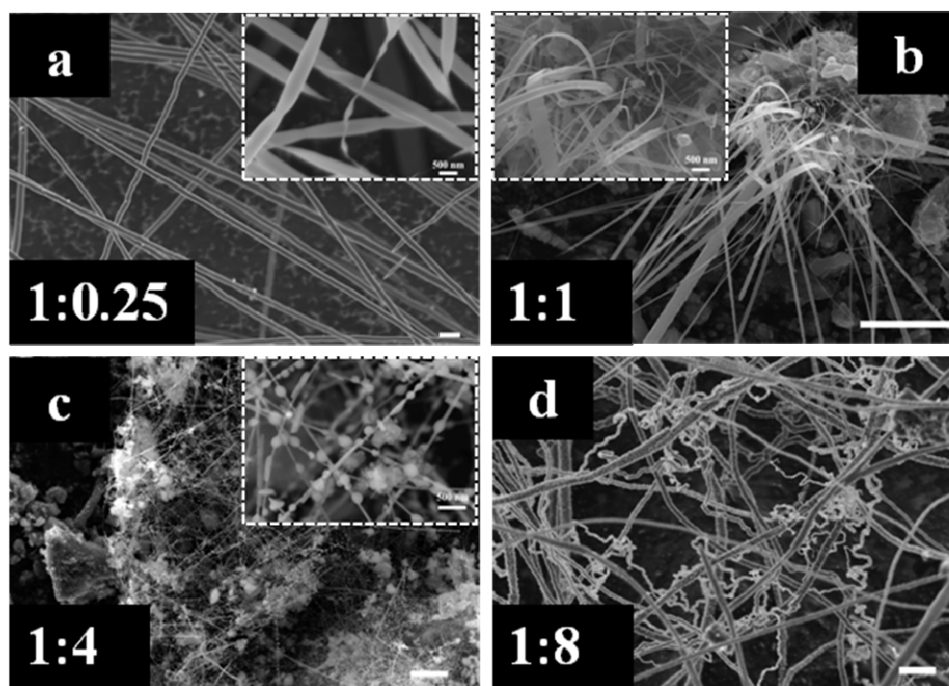


Figure 38. SEM images of Si-doped BC NWs at various B to C ratio of 1: a) 0.25, b) 1, c) 4 and d) 8 at 1250°C. The scale bar corresponds to 5 μm .

The SEM images of structures obtained from the growths at 1150°C and 1250°C at different B:C ratios with Si are shown in Figure 39a-d and 39e-h, respectively. As with the pristine B_4C nanostructures, there was no significant growth when the synthesis temperature was below 1000°C. As the temperature was increased from 1150°C to 1250°C there was more growth, and the formation of the same wool-like material that also resulted without the presence of Si was found in the alumina boat. The wires appeared in bunches, resulting in different morphologies that were not previously observed with pristine B_4C structures. When the synthesis temperature was 1150°C and the B to C ratio was low (1:0.25 and 1:1), the wires were short and appeared to sprout around large amounts of unreacted material, as shown in Figure 39a and 39b. The growth at 1150 °C and 1:1 ratio was heterogeneous as indicated by the presence of long NWs in

Figure 39b. However, when the temperature was increased to 1250°C while keeping the B to C ratio same, an increase in the growth of nanostructures was observed, as shown in Figure 39e. Some very large wires along with high density of small diameter wires can be seen in Figure 39e. However, the yield of structures is dramatically reduced when the B:C ratio is increased from 1:1 as shown in Figure 39f. Furthermore, when the synthesis temperature was 1150°C and the B to C carbon ratio was increased to 1:4, curly structures began to appear along with straight NWs. Figure 39c shows very thin (~200 nm) and curly wires entangled together. When temperature of synthesis was increased to 1250°C, there was an appearance of beads trapped between the wires, as shown in the Figure 39g. As explained previously, these beads could possibly be the silicon and catalyst particles trapped within the wires. When the ratio was increased to 1:8, the density of structures was dramatically low once again with only a few long, straight wires with catalyst tips were found, as shown in Figure 39d. The nanostructures and nanowires showed a large increase in yield when the synthesis temperature was changed to 1250°C while keeping the ratio at 1:8. Overall the best growth conditions for Si-doped wires along with nanostructures were observed for a B to C ratio of 1:8 and a temperature of 1250°C. However, the results in Figure 39 indicate that the growth of structures in the presence of Si is sensitive and unpredictable, which makes trends in terms of the B:C ratio and temperature difficult to identify.

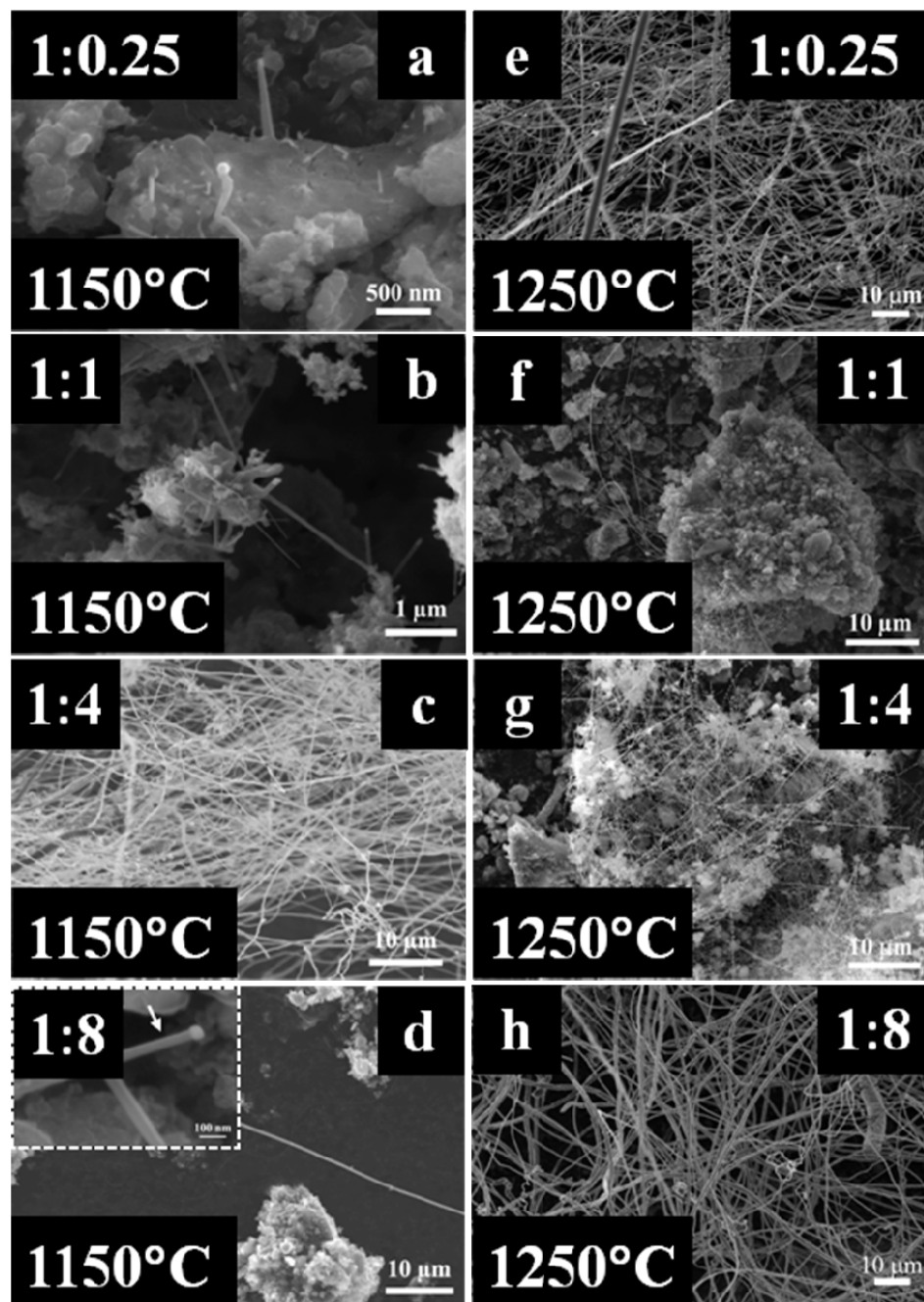


Figure 39. SEM images of Si-doped BC NWs at various growth temperatures: a-d) correspond to 1150 °C and e- h) to 1250 °C. More specifically (a) B:C ratio = 1:0.25 at 1150 °C, (b) B:C ratio = 1:1 at 1150 °C, (c) B:C ratio = 1:4 at 1150 °C, (d) B:C ratio = 1:8 at 1150 °C and (e) B:C ratio = 1:0.25 at 1250 °C, (f) B:C ratio = 1:1 at 1250 °C, (g) B:C ratio = 1:4 at 1250 °C, (h) B:C ratio = 1:8 at 1250 °C. The arrows in the inset of figure 39d corresponds to nanowires with a visible catalyst tip.

Transmission electron microscopy (TEM) and high resolution transmission electron microscopy (HRTEM) images of Si-doped boron carbide NWs are shown in Figure 40. A single long nanowire of ~ 25 nm in diameter is shown in Figure 40a. The nanowire is marked by the presence of a catalyst particle at the tip. The single crystalline nature of the nanowire is confirmed by the lattice imaging shown in the inset in Figure 40b. Together with the HRTEM image shown in Figure 40b, we confirmed that the nanowires are single crystalline in nature and the calculated d-spacing corresponds to B_4C . The elemental composition of the nanowires was confirmed by EDS and EELS analysis. The parts of the wire from which the EDS, HRTEM image and the diffraction pattern were taken are indicated by squares in Figure 40a. The EDS spectrum indicated the presence of silicon in the head of the nanowire along with other elements such Co and Ni, which were used in the synthesis process. In addition, EELS, along with elemental mapping, provided the proof of silicon doping in the boron carbide nanowires as shown in the Figure 41. A STEM image of a single nanowire with a catalyst particle at the top is shown in Figure 41a. A representative EELS spectrum taken from this nanowire region (x) marked by the red shading is shown in the STEM image in Figure 41b. The red shaded windows show two distinct absorption features, one starting at 185 eV and another at 285 eV corresponding to the known boron and carbon K edges, which were used in extracting intensity maps of these elements.

The evidence of silicon doping is also shown by the elemental mapping of a silicon doped boron carbide nanowire. The elemental maps were collected from a 50 nm by 100 nm region of the nanowire indicated in Figure 41a. The elemental maps of boron, carbon, nickel, cobalt and silicon are shown in Figure 41c to g. The head of the nanowire

is predominantly nickel, cobalt and silicon while the tail comprises of boron, carbon and silicon. The silicon seems to be well distributed throughout the whole body of the nanowire but primarily concentrated along the edges of the nanowire. However, thus far, the formation of SiC at the edges of B₄C has not been detected. A more detailed TEM analysis is presently being carried out to investigate the mechanism for Si segregation to the edges.

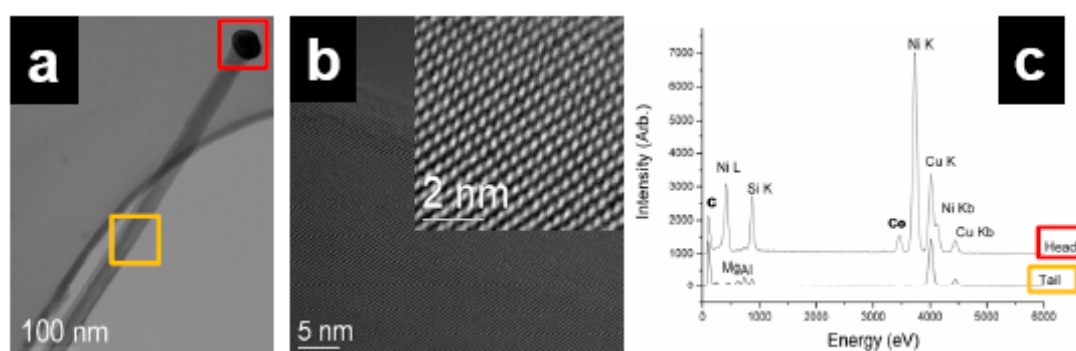


Figure 40. (a) TEM images showing the single crystalline nature and elemental composition of Boron Carbide nanowires. a) TEM image of a single long Si-doped boron carbide nanowire b) HRTEM image along with a FFT pattern confirming boron carbide NWs and c) EDS spectrum (tail and head of NW) indicating the elemental composition. All the images correspond to growth condition with B:C ratio = 1:1 and 2 wt. % Si at 1150 °C.

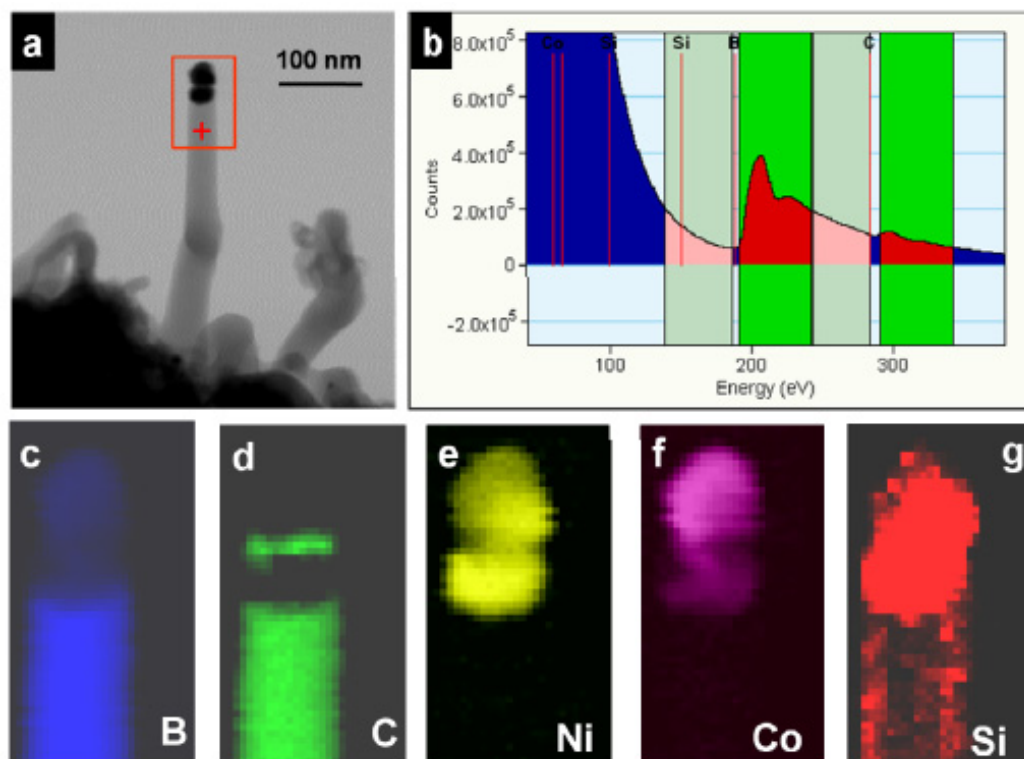


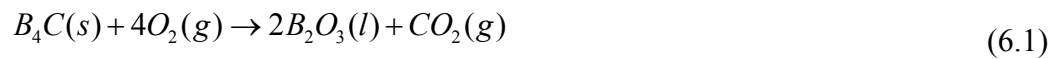
Figure 41. STEM image and EELS compositional maps of a single Si-doped boron carbide nanowire indicating the presence of catalyst at the top. a) STEM image of the mapped wire, b) a representative EELS spectrum with the characteristic boron and carbon K-edges used in elemental mapping, and c-g) the elemental maps of various elements present in the nanowire, c) Boron (B), d) Carbon (C), e) Nickel (Ni), f) Cobalt (Co) and g) Silicon (Si). Each map was collected over a region of 50 nm by 100 nm with different colors corresponding to different elements.

6.3.4 Thermo Gravimetric Analysis (TGA)

TGA was performed in order to obtain insight into the various products present in the as synthesized material. The TGA curves for several samples along with a commercial boron carbide powder are shown in Figure 42. Multiple reactions were found to take place during TGA of the B_4C and Si-doped nanostructures, resulting in weight losses of varying magnitudes. First, a small weight loss was found to occur in all samples between 100 and 350°C due to the release of adsorbed species and, presumably, of hydroxyl groups present on the B_4C surface. Second, the oxidation of amorphous carbon

in air is likely to be responsible for weight loss up to 600 °C. Furthermore, the oxidation of B₄C at 550 °C-600 °C and continuing up to 1200 °C is expected to increase the weight of the sample [30].

It can be observed from Figure 42 that after the initial weight loss in some samples B₄C NW oxidation initiates at about 550-600°C and continues up to 1150°C under a constant heating rate of 10°C/min. It results in a mass gain in these samples near 550°C and a progressive increase of the thermogravimetric curves is observed up to 1200°C. The curves in Figure 42 can be divided into two categories. The top part of Figure 42 contains curves with low boron to carbon ratios of 1:0.25 and 1:1 and the bottom part consisting of higher boron to carbon ratios of 1:4 and 1:8. Curves 1 to 4 contain a lower amount of carbon and consequently show pronounced oxidation in comparison to curves 5 to 8, which contain higher amount of carbon. A large weight loss up to 600°C in curves 5 to 8 is associated with the large amount of unreacted precursor carbon or amorphous carbon in the product. At temperatures greater than 600°C, the possible reactions between boron carbide and oxygen in air could be:



The formation of a liquid-B₂O₃ layer as a result of oxidation was confirmed by imaging NWs before and after TGA. The oxidation on B₄C has been studied by several investigators who found that the oxidation rate of the B₄C increases with temperature and is limited by the diffusion of B and C from the bulk to the surface [4, 30, 32, 112, 113].

Several authors have confirmed that the primary oxidation product is a film of B_2O_3 [30, 114]. Gogotsi *et al.* found that the oxidation of boron carbide started at about 550°C in oxygen and resulted in the formation of a thin transparent B_2O_3 film [112]. The oxidation film formed at the surface can also consist of species like HBO_2 or H_3BO_3 , including B_2O_3 [115].

TGA of Si-doped NWs is distinctly different from the pristine B_4C material and the bulk B_4C powder. The oxidation of NWs with Si shows different behavior depending on the B to C ratio. The curves (1 and 3) obtained in Figure 42 containing Si are very similar to those described by Gogotsi *et al.* for B_4C with a smaller content of Al and Si causing additional oxidation [31, 113]. Curves 1 and 3, with low carbon content and containing Si show additional oxidation in comparison to curves 2 and 4 with no Si. This effect was not observed for the curves with higher carbon content. The addition of Si causes further oxidation and weight gain of boron carbide NWs by the following reaction which seems to compound the oxidation of B_4C :



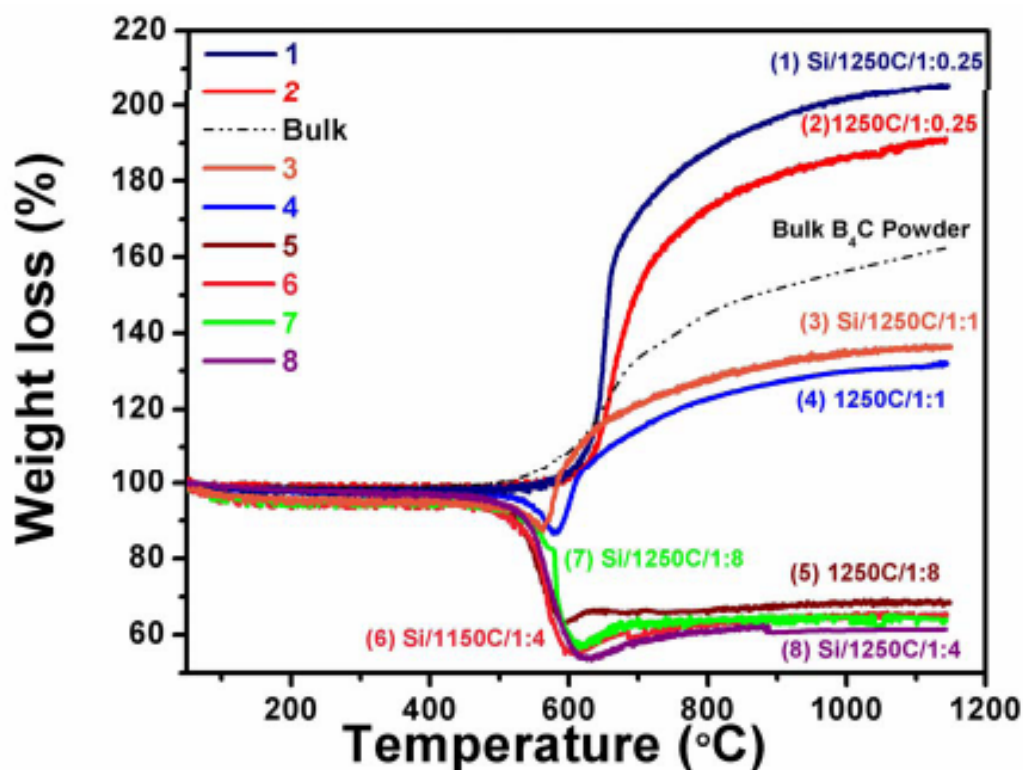


Figure 42. Thermo-grams comparing the weight loss and weight gain for different temperatures and different B to C ratios in the B_4C /Si-doped B_4C NWs and bulk boron carbide.

6.3.5 Summary of the diameter and length distributions

Figure 43 and 44 elucidate the distributions in diameter and length of our nanowires as a function of the growth parameters. The experimental data was derived by means of commercially available software for image analysis (Adobe PhotoshopTM CS3). For each specific growth condition, statistical analysis of a number of randomly taken SEM micrographs, representative of a different portion of the deposit, was carried out. The diameter of each nanowire was determined by cross-sectioning it on multiple points, in order to average the variations along the wire axis. The length of curved nanowires was estimated by interpolating their axis with a b-spline line, whose length was then calculated by the program using the numeric line integration. Despite the fact that both

length and diameter distributions are rather broad, two quite different behaviors at 1150°C and 1250°C can be observed. The average diameter at the two different temperatures of pristine and Si-doped boron carbide nanowires are shown in Figure 43 specifically, the data is presented as histograms and summarized in Figure 43c and 43f. Similarly, the length distribution at the two temperatures of B_xC and Si-doped B_xC are summarized in Figure 44. The summary of the statistical analysis is plotted in Figure 44c and 44f.

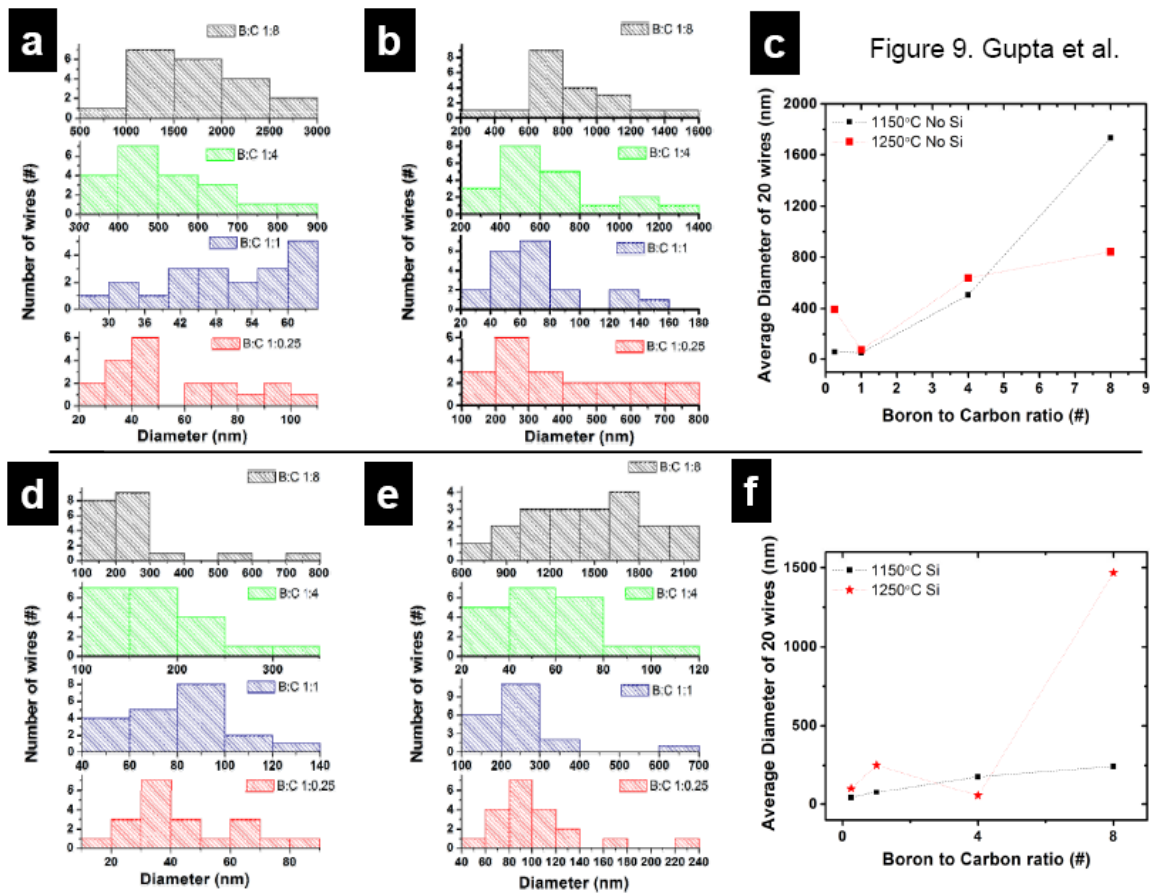


Figure 43. Experimental distribution of the nanowire diameters in the various examined growth conditions. With the exception of one point (B/C = 0.25, 1250°C, in the presence of Si) the trends predicted by the model in the text are fulfilled.

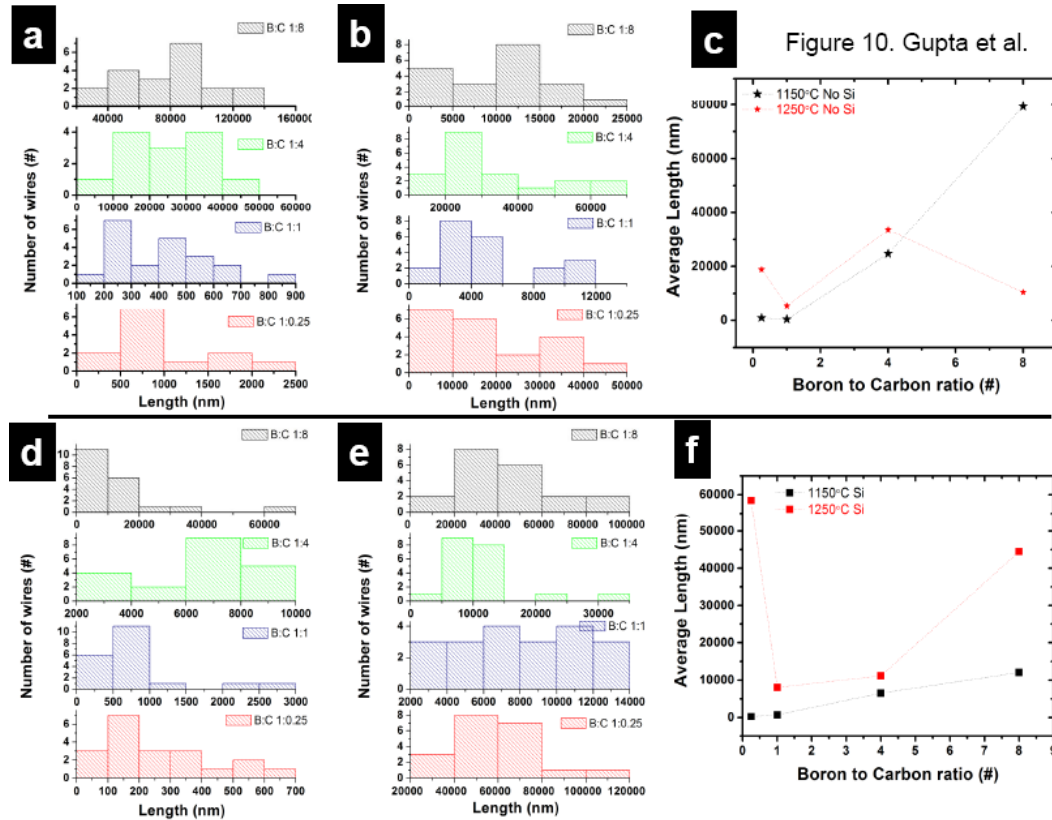


Figure 44. Experimental distribution of the nanowire lengths. The length of nanowires grown at $T_1 \approx 1250^\circ\text{C}$ undergoes a non-monotonic behavior as a function of the B/C ratio.

Analyzing the data more closely, it can be seen that at 1250°C growth, both the average diameter and length decrease initially at low B/C ratios and increase at higher B/C ratios (with the only exception being synthesis at $\text{B/C} = 8$ in the presence of Si where the distribution was exceptionally broad, making it difficult to obtain a mean value). In contrast, at 1150°C , the diameter and lengths were found to increase with B/C ratio, and little growth occurred at low B/C concentrations. The broad distribution of length and diameter is likely to be related to the relatively large size of the powder grains of boron and carbon precursors. Although the powders were ground to reduce the particle size prior to synthesis, their size still remained microscopic so that diameters ranging from

tens to hundreds of nanometers resulted. The distributions in diameter may also indicate variations in composition.

6.3.6 Discussion of the growth mechanism

Growth of the nanowires by the vapor-liquid-solid (VLS) and SLS mechanisms occurs from catalyst droplets of supersaturated liquid, as first suggested by Wagner and Ellis [116]. Thus, the catalyst particles consist of, in this case, Ni and/or Co mixed with the other precursors which decrease the melting temperature of the mixture without forming a stable compound. Subsequently, since the sticking coefficient of a liquid is much larger than the solid phase, diffusion of precursors into the liquid droplet is higher, which leads to supersaturation. As the process is continued, precipitation of excess products occurs from the liquid droplet in the form of nanowires [117]. Although this process is similar to VLS, the broad distributions of length and diameter add substantial complexity to the defining mechanisms responsible for boron carbide nanowire growth by SLS.

Nevertheless, in order to understand the effects of temperature, composition and Si addition on the B_xC nanowire formation by SLS, we have developed a simple, semi-quantitative model that captures the salient features of the synthesis process. The three simple assumptions on which the model is based are:

- 1) Composition and the supersaturation of the liquid phase is determined, under quasi-static conditions, by the B-C phase diagram where Co, Ni, and Si act as solubilizing agents or impurities;

2) The liquid phase arranges in nanosized droplets where the minimum diameters are governed by nucleation theory;

3) Nanowire growth occurs under stationary conditions from supersaturated liquid droplets. The droplet size is reasonably close to the minimum size predicted by nucleation theory.

The foundation of the model rests on the boron-carbon phase diagram. The temperature versus boron/carbon concentration phase diagram of boron carbide is shown in Figure 45a. Regions labeled x_a and x_c represent the temperature and composition where B_xC solid and liquid coexist. Examining the two regions in the phase diagram closely, it can be seen that the solidification temperature for the carbon-rich phase is higher than the boron-rich phase. This suggests that the B/C composition should influence the optimal temperature where growth occurs. The temperatures of the two regions (x_a and x_c) are well in excess of our growth process. We assume that the incorporation of Ni, Co (and Si) changes the eutectic and peritectic points to lower the temperatures without significantly affecting the conditions at which these phases occur. Furthermore, since the experimental results show no nanowire growth at 900 °C, while significant growth occurs above 1100 °C, we estimate the eutectic temperature of the $B(Co, Ni, Si)_y$ mixture to be above 1100 °C. This value is in agreement with the B-Ni and B-Co phase diagrams reported in the literature [118]. Also, since no growth was observed above 1400 °C, we estimate this temperature to be the upper limit at which liquid phase catalyst and solid B_xC phases coexist.

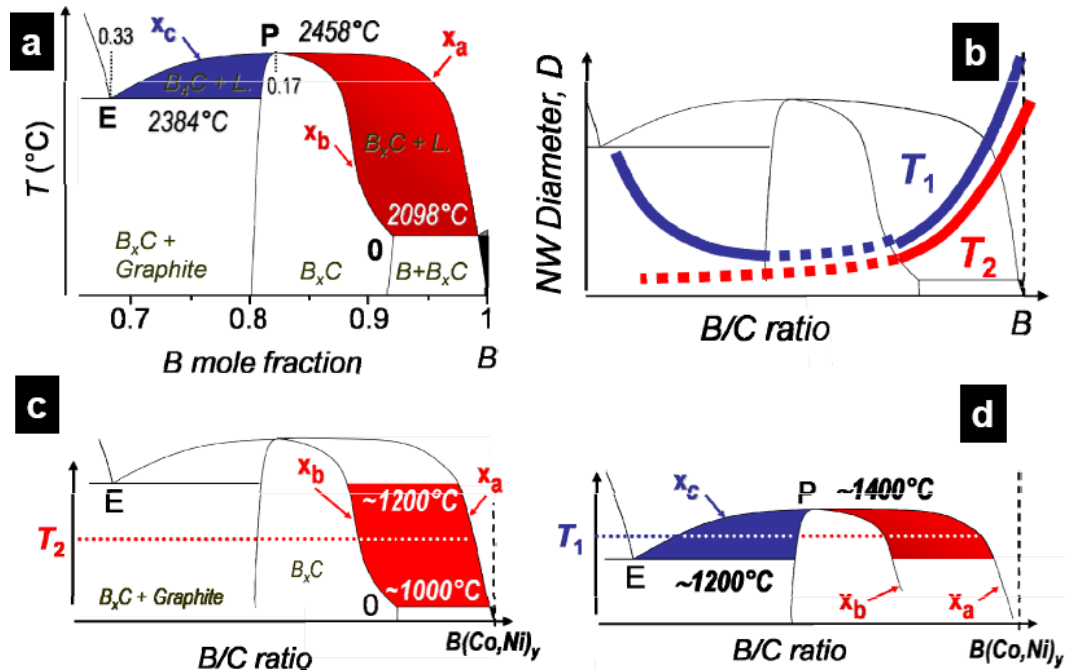


Figure 45. (a) Schematic of the boron-rich end of the B-C phase diagram . Areas involving supersaturated liquid are highlighted in blue (C-rich liquid and B_4C crystallites) or red (B-rich liquid and crystallites at variable B_xC composition). (b) Consequently at $T_1 \approx 1250^{\circ}\text{C}$, the critical catalyst diameter d_c (hence the nanowire diameter $D \sim d_c$), first decreases with B/C ratio and then increases. In contrast, at $T_2 \approx 1150^{\circ}\text{C}$, the behavior described Figure 45c leads d_c and D to increase with B/C ratio. Dotted lines are regions of the phase diagram where the liquid phase does not exist, but may locally appear due to inhomogeneities in precursors (B and C powders), as described in the text. (c) According to the lever's rule, at $T_1 \approx 1250^{\circ}\text{C}$, the degree of supersaturation of the catalyst particles first decreases with the B/C ratio (in the region involving carbon-rich liquid) and then increases (in the region involving boron-rich liquid), while (d) At $T_2 \approx 1150^{\circ}\text{C}$, only B-rich liquid exists, thus supersaturation increases.

Assuming the above, the degree of supersaturation (σ) of the catalyst particles will depend not only on the B/C ratio in the precursors but also on the synthesis temperature. That is, according to the phase diagram, in the boron-rich compositions the degree of supersaturation at a given composition will occur at a lower composition than in the carbon-rich phase and thus σ will depend on B/C ratio. This is critical since the degree of supersaturation and the critical diameter (d_c) of the catalyst particles are related according to [20]:

$$d_c = \frac{4\gamma(T)}{-k_B T \cdot \ln(\sigma)} \quad (6.4)$$

where $\gamma(T)$ is the vapor tension at the droplet surface which increases as a function of temperature and is assumed to be independent of the B/C ratio and the Si content. d_c can be seen to be an increasing function of σ , since $0 \leq \sigma \leq 1$. In order to establish a preliminary model, it is hypothesized that all droplets are close to the minimum (critical) diameter allowed by eq. (4). In addition, as the nanowire diameter (D) is determined by the catalyst size, D is assumed to be close to d_c .

Eq. (6.4), coupled with the assumption $D \sim d_c$, shows that D strongly depends on σ and hence on the B/C ratio. Based on this, it is possible to calculate the trend of the nanowire diameter as a function of B/C ratio for different temperatures. The variation of the nanowire diameters with composition on the B-C phase diagram for two different temperatures is sketched in Figure 45b. The trend in Figure 45b was determined by obtaining the degree of supersaturation according to the lever rule and assuming that the B/C ratio can vary locally due to heterogeneous precursor particle size distribution and variation in composition due to poor mixing. From the schematic in Figure 45b, it can be seen that at low temperature ($T_2 = 1150$ °C) only boron-rich supersaturated liquid is present for growth (see Figure 45c). The degree of supersaturation (σ) therefore increases at low B/C ratios. However, if the B/C ratio is further increased, the 1150 °C is not sufficiently high to create B_xC + liquid eutectic (Figure 45c) and the growth of nanowires is suppressed.

In contrast, at higher temperatures ($T_1 \approx 1250^\circ\text{C}$) carbon-rich supersaturated liquid is present when the B/C ratio is in the x_c compositional range, as indicated in Figure 45d. Furthermore, the boron-rich region also contributes to the growth of nanowires because 1250°C is sufficiently high for the formation of B_xC solid and liquid phases (Figure 45d). Thus, σ decreases with B/C ratio at low values but increases at higher ratios. This trend of diameter with temperature is summarized for the two temperatures (T_1 and T_2) in Figure 45b.

The droplet diameter also influences the nanowire growth rate (dL/dt) and the nanowire length (L). In case of SLS process, incorporation of the precursors inside the droplet may occur either by direct dissolution in the liquid from solid phase, diffusion along the walls of the growing nanowire, or sublimation and subsequent condensation. The processes that contribute to the nanowire length are presented schematically in Figure 46 a-c. In general, growth can be represented by the rate equation [119]:

$$\frac{dN}{dt} = \rho \cdot \frac{\pi}{4} D^2 \cdot \frac{dL}{dt} = \Phi(p, T, x, D) \quad (6.5)$$

where N is the number of atoms incorporated into the nanowire per unit time and is related to the increase of length with time (dL/dt) of the wire diameter D and the nanowire density, ρ (varying relatively slowly for the B_xC single phase). The total number of atoms diffusing into the liquid catalyst per unit time (Φ) can be determined and related to the wire diameter.

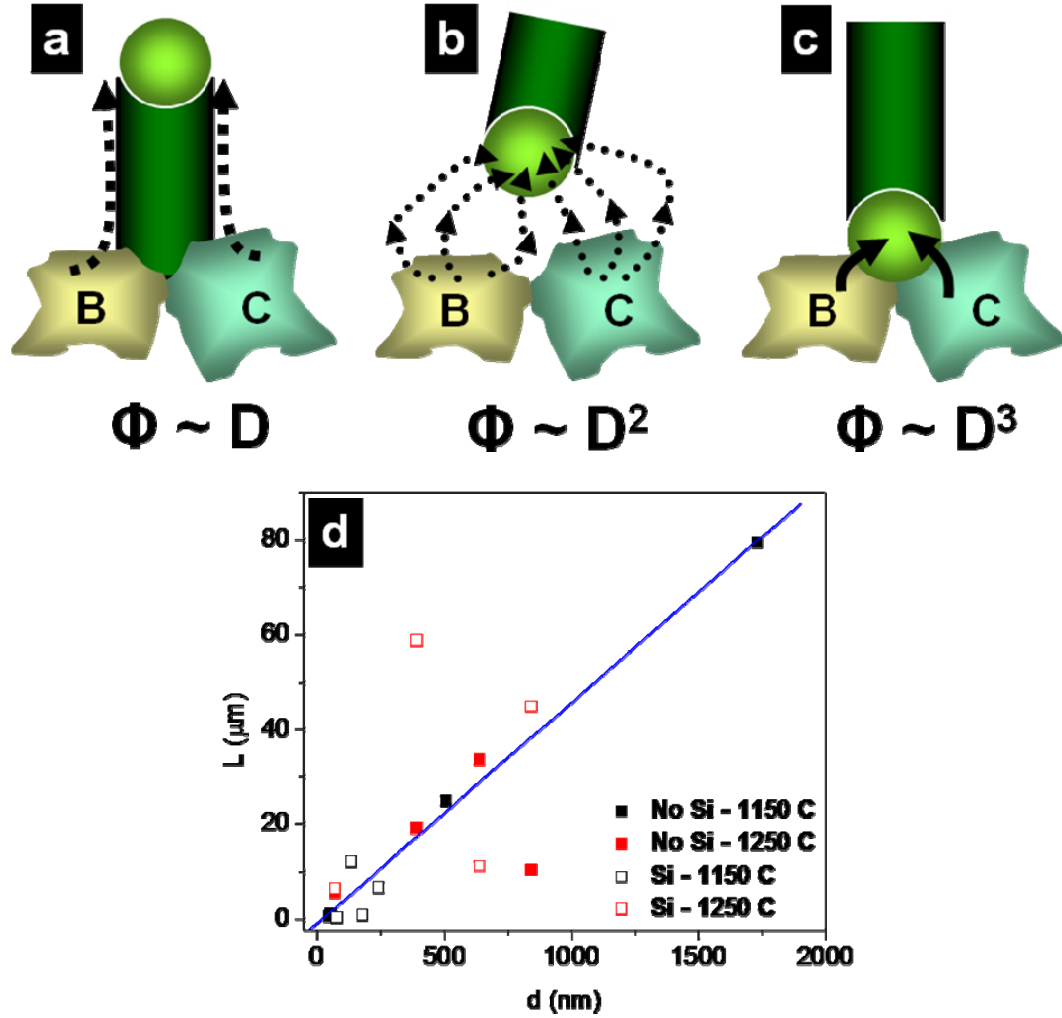


Figure 46. Schematic of three different mechanisms examined for the incorporation of B and C in the supersaturated liquid catalyst particles: (a) Incorporation from superficial diffusion along the sidewalls of the wire (b) sublimation driving growth and (c) direct dissolution into the droplets from solid precursors. The crude trends of the growth rate (and the nanowire L) in the three cases are shown and (d) since L is proportional to D in our case, we suggest that the growth mainly occurs by direct dissolution of the precursors into the catalyst droplet.

For the case of diffusion of reactants along the nanowire sidewall (Figure 46a), Φ can be assumed to be proportional to a superficial diffusion coefficient independent of the diameter and related to the circumference of the wire, πD . Therefore, the axial growth rate can be represented as $dL/dt \sim 1/D$, which is what is obtained in VLS [120] and demonstrates that the length decreases with diameter. In case of sublimation of the

precursors and their subsequent condensation on the surface of the liquid catalyst (Figure 46b), Φ will depend on the flux of atoms impinging the particle (J , which is a function of pressure) and on the surface (\sim hemisphere) exposed to the vapors. Thus, $\Phi = J \cdot \pi D^2 / 2$. Finally, if the flux of precursors entering the liquid catalyst is controlled by their direct dissolution in a finite volume [121], Φ will be controlled by the droplet volume and, thus Φ will be proportional to $\pi D^3 / 6$ (Figure 46c). These three schemes sketched in Figure 46a-c can then be explained in the following manner.

Since the synthesis time was kept constant for all the depositions the above results can be used to summarize the relationship of length (L) to diameter (D) according to:

$$L \sim 1/D \quad \text{for sidewall diffusion}$$

$$L \sim \text{const}(D) \quad \text{for sublimation-condensation}$$

$$L \sim D \quad \text{for dissolution from solid phase}$$

The experimental results plotted in Figure 46d, clearly reveal a linear relationship between the length and diameter of the nanowires, irrespective of the deposition temperature and B/C ratio. Therefore, we suggest a deposition mechanism involving direct melting and dissolution of the solid boron and carbon powders into supersaturated liquid droplets as the most likely growth process in the SLS method.

In summary, a simple SLS model is developed for the growth of nanowires based on the B-C phase diagram. The B/C ratio was found to determine the minimum diameter of the supersaturated catalyst particles in the framework of the nucleation theory. In principle, our model is not able to explain why experimentally some nanowire growth

occurs for precursor proportions of $B/C \sim 4$ (Figure 45b where the D vs. composition trend is reported with red dotted lines), where the reagent mixture should remain solid and no growth should be observed. However, this can be explained by realizing that the particle size of the precursors (B and C powders) used was larger than d_c , which creates a strong local inhomogeneity in the composition of the reagents. In addition, the limited amount of silicon does not alter the growth mechanism of boron carbide nanowires. This is in general agreement with ternary B-C-Si phase diagrams available in the literature [122] that predict the possibility of solid solutions of Si in B_xC up to 5-6 atomic percent. Therefore Si addition is a viable choice for doping B_xC nanowires.

6.4 Summary

A systematic way to synthesize boron carbide/Si-doped boron carbide nanowires and structures has been demonstrated. The growth takes place by a solid-liquid-solid mechanism at temperatures ranging from 1150 to 1250°C. The dimensions of the wires have a large distribution with lengths varying up to 500 μm and diameters ranging from 5 nm to 2 μm . An increase in the ratio of boron to carbon from 1:0.25 to 1:8, led to the formation of thicker and longer wires. Boron carbide nanowires were also doped with silicon. Taking into account the detailed analysis of the diameter and length distributions as well as the B/C ratio and temperature, we have proposed a preliminary model for the growth of boron carbide nanowires. The model is limited but captures most of the salient features of the SLS growth mechanism for B_xC nanowires.

| CHAPTER 7 | NANOCOMPOSITES FROM ULTRA-LONG BORON CARBIDE NANOWIRES AND POLY(METHYL METHACRYLATE)

Continuous development towards high performance organic devices on large area, flexible platforms holds promise for inexpensive electronics [123-126]. Integrating organic materials with nanostructures also allows the fabrication of transparent and flexible devices [127-129]. The realization of high performance integrated devices that are flexible and transparent will require the peripheral electronics components to also meet these criteria. That is, organic electronics will require power dissipation using materials that can be integrated into flexible and transparent platforms. Here we report thermally conducting nanocomposites that are also transparent from direct solution blending of ultra-long boron carbide (B_4C) nanowires (NWs) with poly(methyl methacrylate) (PMMA). Introduction of just 0.025 wt% of B_4C NWs into PMMA leads to an almost one order of magnitude increase in the thermal conductivity and diffusivity (from 0.176 W/m-K and $1.26 \times 10^{-3} \text{ cm}^2/\text{sec}$, respectively, for PMMA to 1.11 W/mK and $8.538 \times 10^{-3} \text{ cm}^2/\text{sec}$, respectively, for the nanocomposite) along with a substantial increase (by $\sim 40^\circ\text{C}$) in the glass transition temperature. The exceptionally low loading of B_4C NWs into PMMA at which these properties are achieved in comparison to other filler materials is attributed to the very high aspect ratio (10^4 – 10^5) of the ultra-long NWs. Thus, unlike other thermal management composites, the very low loading makes B_4C NW/PMMA transparent.

7.1 Introduction

The reliability of electronic devices is exponentially dependent on the operating temperature, whereby a small difference ($\sim 10^\circ\text{C}$) can result in lifespan reduction by a factor of two [130]. Although all-organic devices are unlikely to dissipate the same amount of power as inorganic circuits, thermal management will be essential in organic electronics because the active components consist of materials that are highly temperature sensitive. Due to the moderate power dissipation, thermal conductors in organic electronics may not require materials with highest thermal conductivities. Instead, moderate thermal conductivity materials possessing other important properties such as flexibility, transparency and processing that allow integration onto plastic substrates could be attractive for thermal management applications in organic electronics. A recent patent discloses that transparent and flexible materials with thermal conductivity values ranging from 0.25 – 1.0 W/m-K are suitable for thermal management in high performance organic light emitting diodes (OLEDs) [131]. Commercially available adhesives such as OmegaBond™, 3M 9885 [59, 61], AP-2 and TC350 [132] widely used for heat dissipation have thermal conductivity values of 1.04, 0.60, 0.5, and 1.0 W/m-K, respectively.

Polymers could be advantageous in thermal management applications because they are lightweight and easily processable. However, their low thermal conductivity (~ 0.2 W/m-K) [133-135] limits their use in heat generating environments. To improve their thermal properties, fillers are added to form composites. The physical characteristics (aspect ratio, orientation, dispersion, and conductivity) of fillers along with phonon scattering at the filler/polymer interface can result in a wide range of thermal

conductivities [136-141]. However, this approach requires filler concentrations of 50 – 60 vol% to achieve thermal conductivities of $\sim 2 - 10$ W/mK [133, 134, 142]. These loading concentrations are not technologically feasible because of the increase in weight, cost and viscosity of the blend, which limits processability.

Nanocomposites contain nanoscale fillers that can dramatically improve the polymer properties at very low loadings (< 2 vol%) [143]. Single and multi walled carbon nanotubes (SWNTs and MWNTs) have been widely investigated as fillers in nanocomposites for thermal management because of their extraordinary thermal conductivities, which range from 3000 – 3500 W/mK [144, 145]. However, the thermal conductivity value reported for SWNT nanocomposites is 0.85 W/mK at a loading concentration of 7.5 vol.% in epoxy resin. The lower than expected thermal conductivities of nanotube nanocomposites are attributed to substantial phonon scattering at the SWNT/polymer interface. Furthermore, the high loading fraction dramatically reduces the transparency of the SWNT/polymer nanocomposites.

7.2 Method and Experimental Details

The boron carbide nanowires were synthesized by the solid-liquid-solid method in which submicron boron powder (Sigma Aldrich, purity $\sim 99\%$, initial particle size 0.82 μm) and activated carbon (Norit America Inc., purity $\sim 99\%$, initial particle size 5 μm) were used as the starting materials. A mixture (1 wt. %) of Nickel Boride (NiB, Alfa Aesar, purity 99%, initial particle size 500 μm), Nickel Diboride (NiB₂, Alfa Aesar, purity 99%, initial particle size 500 μm) and Cobalt (Co, Alfa Aesar, purity 99.8%, initial particle size 1.6 μm) was used as catalyst for the formation of NWs. The components and catalyst were mixed together and thoroughly ground using an agate mortar and pestle.

The reactant mixture was placed in a 10 mL alumina combustion boat, which was inserted into a 99.8 % dense alumina tube (length = 70 cm, inner diameter = 6.35 cm) in a clam furnace. The powder mixture was heated to 1150 °C and held for 1 hour in argon at a pressure of 1 atm.

Polymethyl methacrylate (PMMA) (LG Chem, Grade: LG PMMA EH910) was chosen as a polymer matrix because of its high transparency and glass transition temperature. Prior to composite preparation, PMMA was first dried for 2 hours at 100°C in a vacuum oven. 2 g of PMMA pellets were dissolved and magnetically stirred in 20 ml of 1,2-dichloroethane (DCE) for 2 h and ultra-long B₄C NWs were added to the solution. The solution was sonicated for 9 h (Branson 1510, 90 W) to improve the micro-scale dispersion of the NWs within the polymer so that they are encapsulated within the matrix after evaporation of the solvent. After sonication, a transparent well dispersed B₄C NWs in PMMA solution was obtained. After 7 days of drying at room temperature, the polymer became rigid and was ground into a polymer disc with a thickness of ~ 1 mm and diameter of ~ 10 mm to measure thermal diffusivity.

Thermal diffusivity (α) of pure PMMA and the B₄C NWs/PMMA nanocomposites were measured by the laser flash method (ULVAC Co., Model: TC-7000). Thermal conductivity (κ) is given by $\kappa = \alpha C_p \rho$, in which the heat capacity (C_p) and the density (ρ) of the nanocomposites were measured by differential scanning calorimeter and densitometer, respectively. Graphite based coatings were sprayed on the both side of disc for accurate measurement of thermal diffusivity. Both ends of the graphite sprayed disc samples were connected during current-voltage (I-V) measurements. The I-V

sweeping indicated the contact was Ohmic. The electrical conductance was then obtained by the slope of the I-V curve.

7.3 Results and Discussion

In this section, the realization of a thermally conducting nanocomposite that is also transparent using ultra-long boron carbide nanowires (B_4C NWs) as filler in poly(methyl methacrylate) (PMMA) is reported. The ultra-long B_4C NWs were synthesized by solid liquid solid (SLS) growth process [146] (see Chapter 6 for details). Optical, scanning and transmission electron microscopy (SEM and TEM) images of typical NWs are shown in Figure 47. The lengths of the NWs ranged from 1 – 5 μm (see Figure 47a) while the diameter varied from 50 – 100 nm. High-resolution TEM imaging and analyses (Figure 47d) reveal that the NWs are single crystals. A fast Fourier transform (FFT) pattern shown as the bottom inset in Figure 47d corresponds to the B_4C or $B_{13}C_2$ lattice viewed along the [010] zone axis. The atomic resolution image in the top inset of Figure 47d shows spacing of 0.39 nm, corresponding to the distance between (003) planes. The Raman spectrum (Figure 47e) from NWs agrees closely with the spectra of bulk B_4C powder [81].

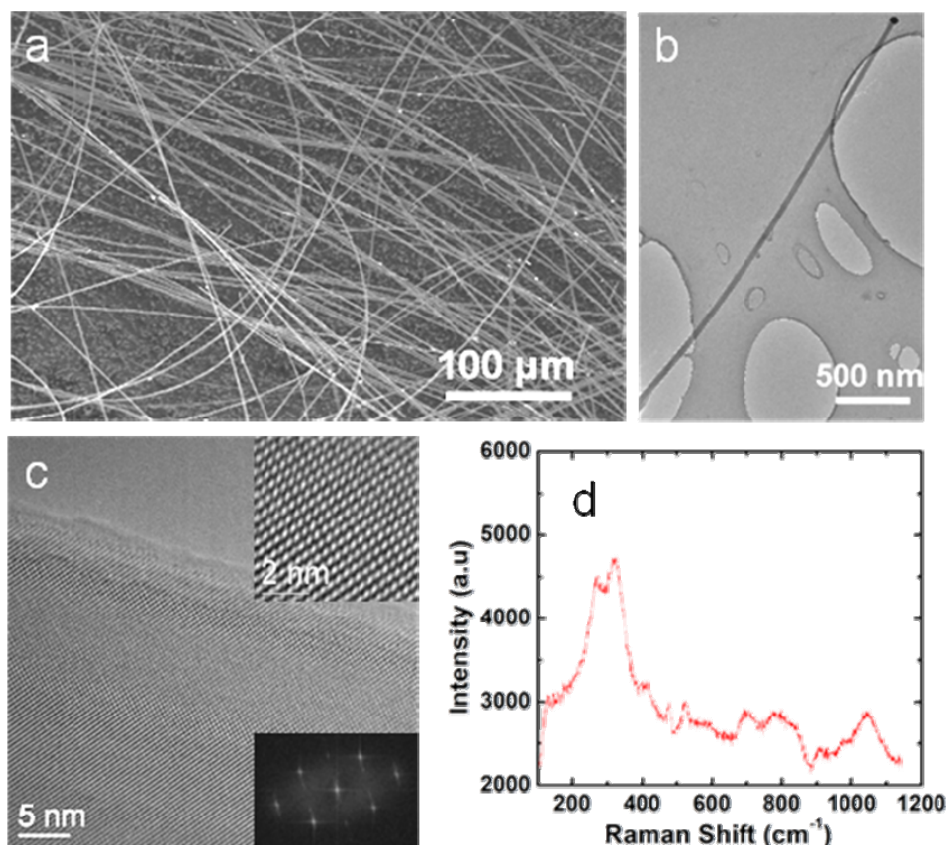


Figure 47. (a) Characterization of ultra-long B_4C nanowires. (a) scanning electron microscopy (SEM, FEI XL30 was used at an operating voltage of 5 kV and a working distance of 6mm) and (b), (c) transmission electron microscopy (TEM, Topcon 002, 200 kV) images of typical NWs. The lengths of the NWs ranged from 1 – 5 mm while the diameter varied from 50 – 100 nm. (c) High-resolution TEM imaging reveals the single crystalline nature of the NWs. A fast Fourier transform (FFT, Gatan Image Acquisition and Processing Software: Digital MicrographTM) pattern shown at the bottom inset corresponds to the B_4C or $B_{13}C_2$ lattice viewed along the [010] zone axis. The atomic resolution image in the top inset of shows the spacing of 0.39 nm, corresponding to the distance between (003) planes and (d) Raman (Renishaw InVia Raman microscope equipped with a 100X objective) was used. The excitation source wavelength was 785 nm) spectra of the B_4C NWs.

The blend was prepared by thoroughly dissolving the polymer in 1,2-dichloroethane (DCE) to create a uniform solution before adding the ultra-long B_4C NWs to obtain a stable dispersion. The solution was dried to obtain disc samples with thicknesses of 1 mm and diameters of 10 mm. The uniformity of the nanocomposite and reproducibility of the results were monitored by extensive SEM imaging and

measurements on numerous samples. Typical morphology of nanocomposites examined using SEM is shown in Figure 48a-d, clearly revealing the presence of B₄C NWs in the PMMA matrix. Qualitative SEM observations of numerous samples also indicate that the NWs are uniformly dispersed throughout the polymer matrix and that there is good adhesion between the B₄C NWs and PMMA (Figure 49-50, additional SEM micrographs of NWs embedded with the polymer matrix).

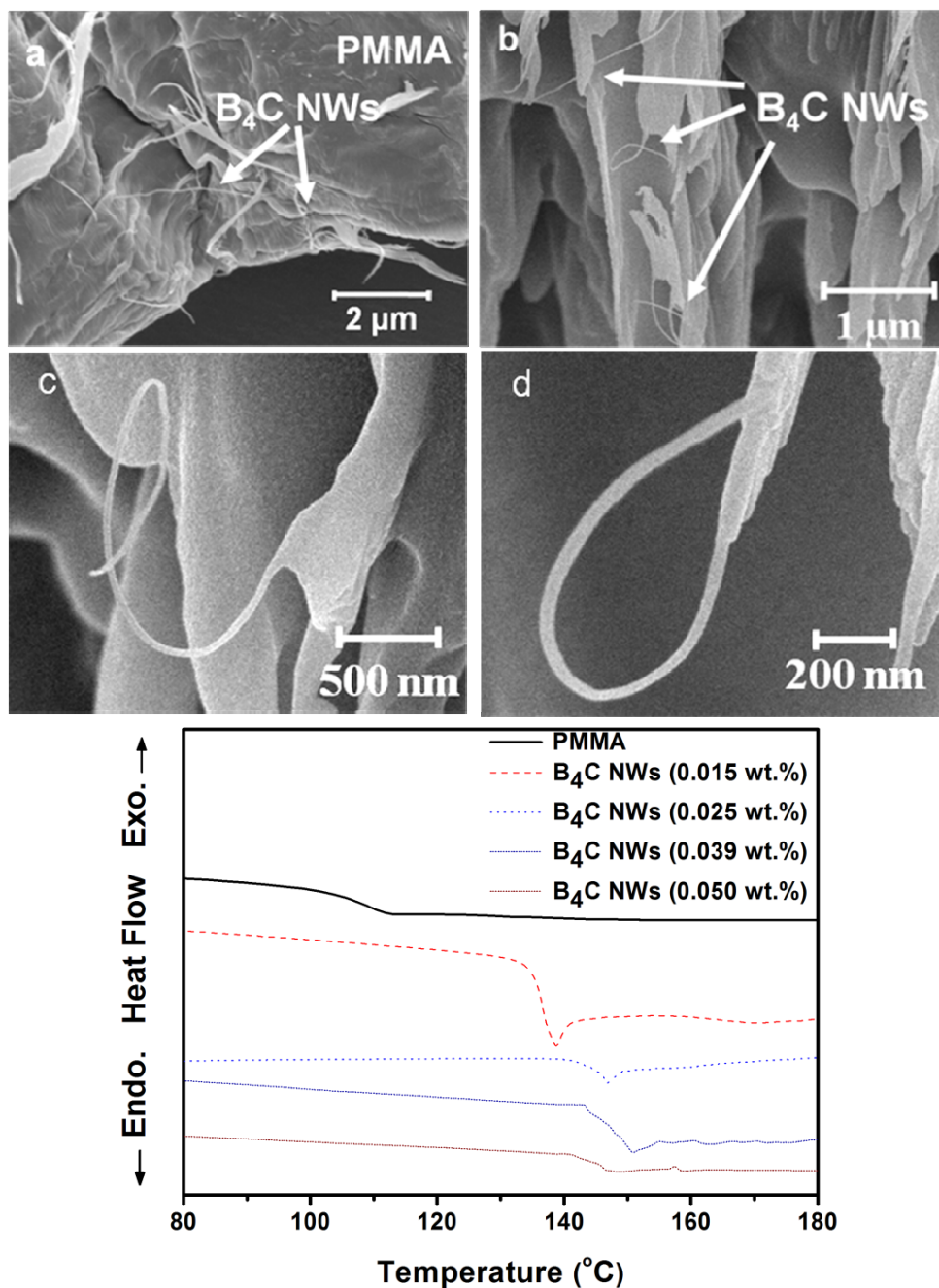


Figure 48. Nanocomposite fabrication and structural properties. (a) typical morphology of nanocomposites (0.025 wt.%) examined using SEM, revealing the presence of B₄C NWs (indicated by arrows) in the PMMA matrix. Specimens in (b)-(d) were prepared by focused ion beam etching. Images in (b)-(d) are high magnification images of NWs protruding from the polymer matrix. (e) The glass transition (T_g) temperature monitored by differential scanning calorimetry (DSC, TA Instruments Co. Model: 2010). Adding 0.025 wt% of ultra-long B₄C NWs into PMMA increases the T_g by $\sim 40^\circ\text{C}$ of the nanocomposites.

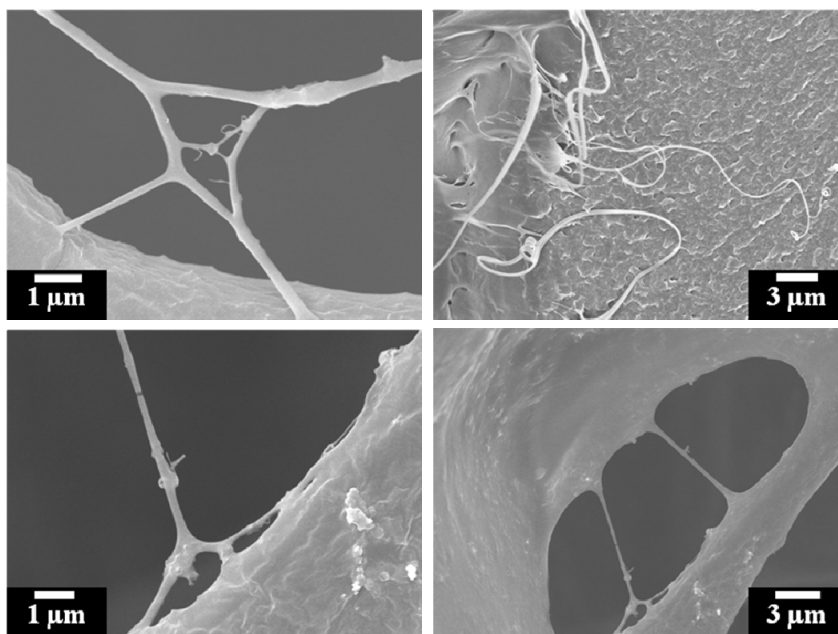


Figure 49. Typical SEM images from nanocomposite containing 0.025 wt.% B_4C NWs in PMMA matrix. The NWs are generally covered with the polymer indicating good adhesion with the polymer matrix.

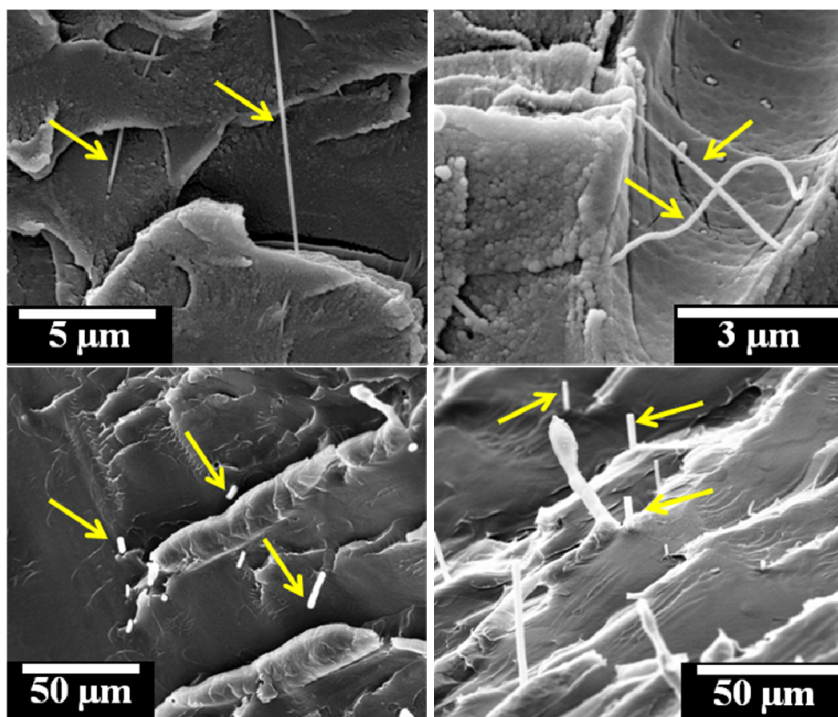


Figure 50. Typical SEM images from nanocomposite containing 0.015 wt.% B_4C NWs in PMMA matrix. The NWs are generally covered with the polymer indicating good adhesion with the polymer matrix.

To investigate the impact of ultra-long B₄C NWs on the PMMA matrix, differential scanning calorimetry (DSC) was performed to monitor the glass transition temperature (T_g). We found that adding 0.025 wt% of ultra-long B₄C NWs into PMMA increased the T_g by ~ 40 °C, from ~ 105 °C for PMMA to ~ 145 °C for B₄C NWs/PMMA nanocomposites (see Figure 48e). The increase in T_g is remarkable given the small NW content in the nanocomposite. It suggests that the thermal integrity of B₄C NWs/PMMA is superior to that of PMMA alone and can be attributed to the restriction of polymer chain movements and lower free volume imposed by the presence of the ultra-long NWs. Although a similar trend in glass transition was observed in polypropylene (PP)/SWNT [147] and polystyrene (PS)/MWNT [148] nanocomposites, neither achieved the ~ 40 °C shift observed here. Recently, graphene based composites reported similar increase in T_g [149]. Changes in the glass transition temperature are particularly important in nanocomposites because they not only provide insight into the fundamental changes in polymer chain dynamics, but also because the associated gains in thermal stability are critical for thermal management applications.

The thermal and electrical conductivities of nanocomposites up to a loading concentration of 0.05 wt.% are shown in Figure 51a. It can be seen that there is dramatic improvement in both conductivities with NW incorporation. The maximum thermal conductivity we obtained at 0.025 wt.% was 1.11 W/mK at ambient temperature. This value is extraordinary because it is 3 - 4% of the thermal conductivity of commercially available bulk B₄C (30 - 40 W/mK) [150] even though the loading concentration of the NWs in the nanocomposites is exceptionally low. Indeed the thermal conductivity is significantly better (at 0.025 wt.%) than that of SWNT nanocomposites

with much larger (two orders of magnitude higher) loading concentrations reported in Ref [151]. Although comparable (0.85 W/mK) and higher (1.95 W/mK) thermal conductivity values have been obtained with 7.5 wt. % SWNTs [152] and 34 wt.% colloidal graphite [153], respectively, the much lower loading concentrations reported here offer significant cost and processing advantages. Above 0.025 wt.%, the thermal conductivity of B₄C NW/PMMA nanocomposites decreases to values that are comparable to SWNT/polymer samples. This is attributed to bundling of the ultra-long B₄C NWs, which leads to poor dispersion within the polymer matrix.

Examining the thermal and electrical conductivity trends with B₄C NW loading concentration in Figure 51a reveals that there is a gradual increase in the thermal conductivity from pure PMMA to 0.025 wt.% loading. In contrast, the electrical conductivity exhibits a percolation threshold with loading, as indicated by the sudden increase at the lowest concentration investigated (0.015 wt.%). The extremely low electrical percolation threshold is attributed to the very high aspect ratios ($\sim 10^5$) of the B₄C NWs [154]. These results suggest that the electrical percolation has no significant effect on the thermal conductivity enhancement, consistent with phonon-dominated picture of thermal transport in nanocomposites [155]. Furthermore, with 100 times higher aspect ratio and diameter than SWNTs, the B₄C NWs are flexible and curved, which decreases the interfacial area and permits much easier contact between NWs and the polymer matrix, which reduces the thermal interfacial resistance. The adhesion between the filler and polymer matrix is likely to be a more important factor for the enhancement in thermal conductivity because phonon transfer at the interface between the filler and matrix cannot occur by hopping [156]. Furthermore, the ultra-long lengths of the B₄C

NWs provide an effectively larger volume, which allows the PMMA/B₄C NW interface to cover a substantial portion of the polymer matrix. That is, the volume of an individual ultra-long B₄C NW is $\sim 10^4$ times higher than typical B₄C NWs that are few microns long. Therefore, the effective volume is substantially higher, allowing phonons created in the PMMA to be effectively transferred to the B₄C NWs.

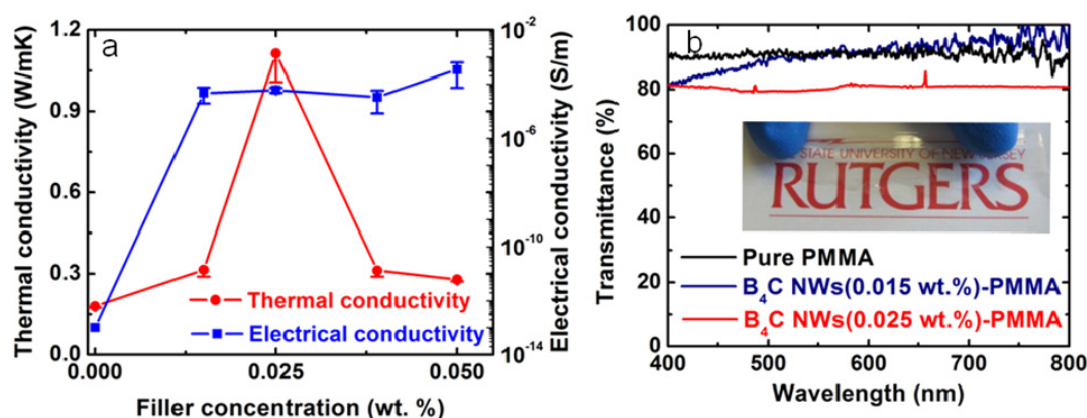


Figure 51. Thermal, electrical and optical properties of the nanocomposites. (a) Thermal and electrical conductivities of the nanocomposites as a function of filler (B₄C NWs) concentration. b) UV-VIS (Perkin Elmer) spectrum of the transmittance versus wavelength of pure PMMA and free standing composite. The transmittance at 550 nm was found to be approximately 80 – 85 %, slightly less than pure PMMA. The photograph in the inset clearly indicates the transparent nature of the nanocomposite.

The transparency of the thermally conducting nanocomposites was confirmed by UV-VIS spectroscopy. The transmittance versus wavelength of pure PMMA and free standing composite is shown in Figure 51b. It can be seen that the nanocomposites are only slightly less transmitting than pure PMMA. The transmittance at 550 nm was found to be approximately 80% at a loading concentration of 0.025 wt.%. The photograph in the inset of Figure 51b clearly indicates the transparency of the nanocomposite. To investigate suitability for flexible electronics, the properties were monitored after flexing

the samples 10 times at 45°. Although the 1 mm nanocomposites are rigid, thinner samples are flexible, as indicated by negligible changes in the properties.

7.4 Summary

In summary, we describe improvement in the thermal conductivity (from 0.176 W/mK to 1.11 W/mK) of PMMA by almost an order of magnitude by adding 0.025 wt.% of ultra-long B₄C NWs. The exceptionally low concentration of the filler at which this improvement occurs is attributed to the very high aspect ratio of the ultra-long B₄C NWs. The gradual increase in thermal conductivity, in contrast to the sudden increase in electrical conductivity, along with the qualitative observations of good adhesion between the NWs and the polymer matrix suggests that the enhancement in thermal conductivity is due to phonon-dominated processes. The very low B₄C NW concentration in PMMA renders the nanocomposites transparent, which we envision will be useful for organic electronics applications. Although the thermal conductivity value reported here is lower than metals, it exceeds those of existing commercially available thermal adhesives for flexible applications. Therefore, B₄C NW/PMMA nanocomposites may be well suited for next generation of large area flexible electronics where heat dissipation requirements are not expected to be as stringent (due the temperature sensitivity of active organic components) as in inorganic circuits and other unique attributes such as transparency, flexibility, and solution processing are likely play important roles in implementation.

| CHAPTER 8 | CONCLUSIONS AND FUTURE WORK

A method for investigation of catastrophic failure in boron carbide has been developed through a combination of Raman analysis and indentation. In addition to boron carbide work described in this thesis, our technique can be successfully applied to other hard and brittle materials.

Under *in situ* Electrical Raman spectroscopy, boron carbide was found to undergo a phase transformation. Specifically, amorphization and eventually large amorphous carbon clusters were detected using Raman spectroscopy during the application of pulses. It was found observed that electrical field pulses in boron carbide produce effects that appear to be similar to those induced by mechanical stress or shock impact.

A novel technique was developed to actually synthesize Si doped boron carbide at nanoscale. Nanowires of boron carbide and Si doped boron carbide were produced by Solid Liquid Solid (SLS) growth mechanism. The diameter of the nanostructures varied widely, ranging from 5 nm to 2 μm . The lengths of the nanowires were found to vary from several micrometers up to a few millimeters (ultra long). By using these ultra long nanowires, thermally conducting, transparent nanocomposites were fabricated from direct solution blending of ultra-long boron carbide (B_4C) nanowires (NWs) with poly(methyl methacrylate) (PMMA). Introduction of just 0.025 wt% of B_4C NWs into PMMA leads to an almost one order of magnitude increase in the thermal conductivity and diffusivity (from 0.176 W/m-K and $1.26 \times 10^{-3} \text{ cm}^2/\text{sec}$, respectively, for PMMA to 1.11 W/mK and $8.538 \times 10^{-3} \text{ cm}^2/\text{sec}$, respectively, for the nanocomposite) along with a substantial increase (by $\sim 40^\circ\text{C}$) in the glass transition temperature. The exceptional low loading of

B₄C NWs into PMMA at which these properties are achieved in comparison to other filler materials is attributed to the very high aspect ratio (10^4 – 10^5) of the ultra-long NWs.

8.1 Future Work

8.1.1 In situ TEM investigation under electric field

In order to understand and observe the fundamental phenomena and failure mechanism in boron carbide, further work needs to be done. The basic approach is to formulate single crystal samples which are electronically transparent (TEM samples). These samples should be subjected to different electrical pulses in a TEM and phase transformation should be monitored in real time.

There has been limited work on studying the relationship between phase transformation and electrical pulses. It can provide wealth of information on such relationships between the failure mechanism and potential phase transformation.

8.1.2 Investigation of mechanical properties of Si-doped boron carbide nanostructures

While successful synthesis of boron carbide and Si-doped boron carbide structures has been shown, more work needs to be done evaluate their mechanical properties. Two different approaches can be utilized to measure their mechanical properties: (a) the nanowires and nanostructures of Si-doped boron carbide can be consolidated by using conventional ceramic processing techniques (hot press, hot isostatic press etc.) and (b) developing a system to measure the individual properties of single nanowires. One such method is via use of AFM. AFM can be used to measure the mechanical response of a single nanowire as shown in the Figure A1.

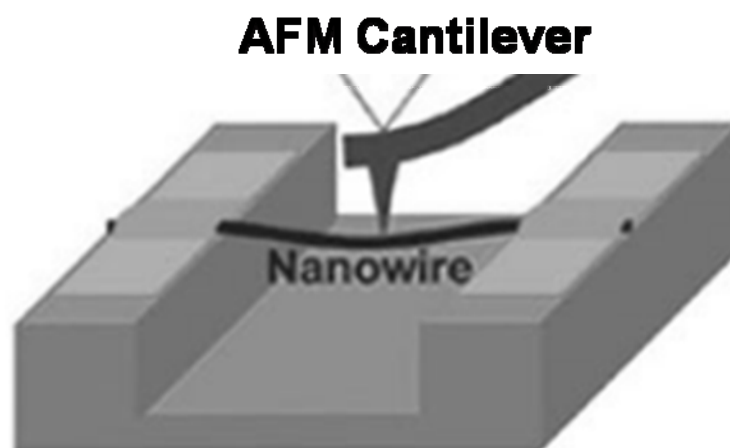


Figure 1A

8.1.3 Understanding the effect of higher boron content in boron carbide

The same effect of a reduction in the $B_{12}(CCC)$ phase concentration might be obtained by other routes. For instance it can be speculated that enriching Boron Carbide in Boron over the B_4C stoichiometry may deplete the chains of carbon, disfavoring the formation of (CCC) chains, hence strengthening the material.

However, a number of intermediate phases between B_4C and pure boron (e.g. B_6C , B_9C , $B_{13}C_2$) have been postulated and their identification is somewhat problematic. However, in order to obtain some insight into how incorporation of excess boron may influence the structure of Boron Carbide. Preliminary investigations on Boron rich B_4C samples with Raman spectroscopy is shown in Figure A2. Future work may focus on the possibility of reduction in concentration of (CCC) chains with increasing Boron content.

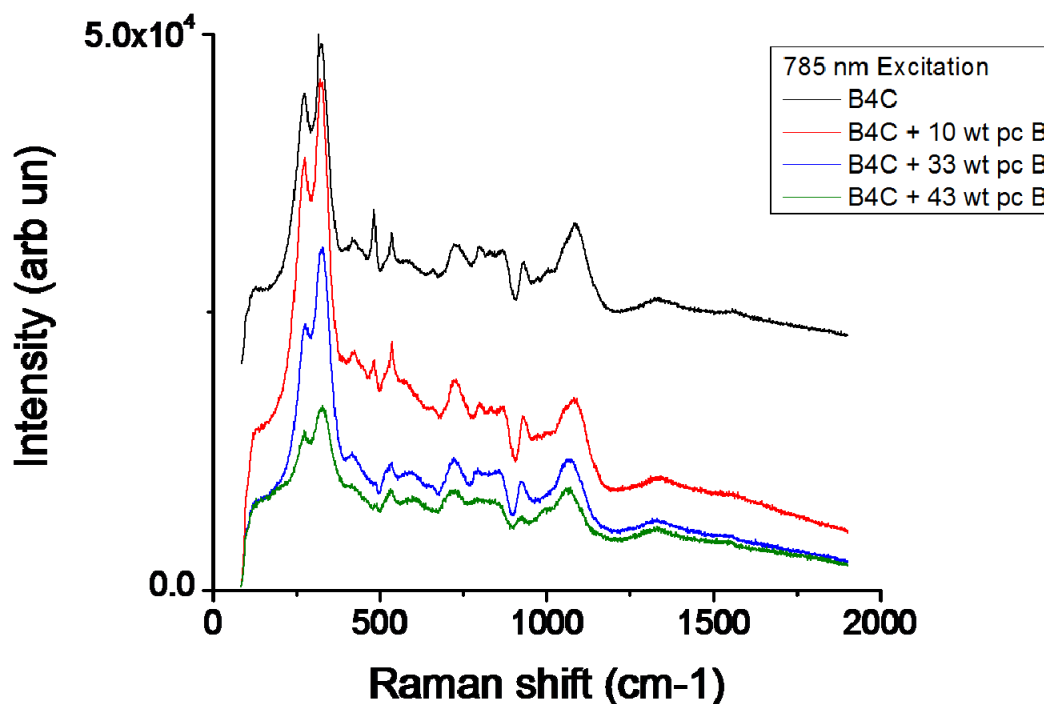


Figure A2.

8.1.4 Structural Analysis using Monte Carlo Simulation

Phase transformation in boron carbide can result in structural re-arrangement of carbon or boron atoms that possibly results in failure of boron carbide. While XRD, Raman analysis and TEM provides information about the structure of boron carbide, they are not sufficient for atomic level understanding. Thus, it becomes very much necessary to visualize the phase transformation and structure rearrangement in B₄C. One of the ways is to determine the radial distribution of carbon and boron atoms using a combination of glass, liquid and amorphous materials diffractometer (GLAD) and diffraction methods (SAXS) and then applying Monte Carlo simulation to visualize various phases. The results from Monte Carlo simulations can be used to theoretically determine the heat of adsorption, heat of formation etc. of different phases and then can

correlate them with experimentally obtained data in the literature. Such comparison can provide information about pre and post failure structural fluctuations in boron carbide.

LIST OF REFERENCES

1. Chen, M. W., McCauley, J. W., and Hemker, K. J., Shock-Induced Localized Amorphization in Boron Carbide. *Science*, 2003. 299: p. 1563.
2. Giovanni Fanchini, James W. McCauley, and Chhowalla, M., Behavior of Disordered Boron Carbide under Stress. *Phys. Rev. Lett.* 97, 2006. 97: p. 035502.
3. Cristina, L., Joao, Oliveira, Manish, Chhowalla, Albano, Cavaleiro, Silicon Effect on the Hardness of r.f. Sputtered B-C:Si Amorphous Films. *Plasma Process. Polym.*, 2009. 6: p. 000.
4. Thevenot, F. J., Boron Carbide A Comprehensive Review. *Journal of the European Ceramic Society*, 1990. 6 p. 205.
5. Ferrari, G., The “Hows” and “Whys” of Armour Penetration. In: *MILTECH*, 1988: p. 81.
6. Rigdway, R. R., Boron carbide. A new crystalline abrasive and wear-resisting product. *Trans. Am. Electrochem. Soc.* , 1934. 66: p. 117.
7. Schroll, F. and Vogt, A., Electrothermic production of boron carbide, in US Patent no. 2 163 293. 1939.
8. Scott, J. J., Arc furnace process for the production of boron carbide, in US patent no. 3 161 471. 1964.
9. Schwetz, K. A. and Lipp, A., Boron carbide, boron nitride and metal borides. *Ullmann's encyclopedia of industrial chemistry*. Weinheim: Verlag Chemie, 1985. 4A: p. 265.
10. Bougoin, M., Thevenot, F., Dubois, J. and Fantozzi, G., Synthese et caracterisation de ceramiques denses en carbure de bore *J. Less Common. Met.*, 1985. 14.
11. G. Goller, C. T., A. Tekin and C. K. Gupta, The production of boron carbide by carbothermic reduction. *High Temp. Mater.*, 1996. 15(1-2): p. 117.
12. Rentzepis, P., White, D. A. and Walsh, P. N., Heat of Formation of $B_2O_2(g)$. *J. Phys. Chem.* , 1960: p. 64.
13. MacKinnon, I. M. a. R., B. G., The synthesis of boron carbide in a r.f. plasma. *J. Electrochem. Soc.*, 1975. 22.

14. MacKinnon, I. M. a. W., A. , The preparation of boron carbide using a radio frequency plasma. J. Chem. Ind., 1973: p. 800.
15. Berjonneau, J., Chollon, G. and Langlais, F., Deposition process of amorphous boron carbide from CH₄/BCl₃/H₂ precursor. Journal of The Electrochemical Society 2006: p. 153.
16. Moore, A. W. a. V., H. F., Chemical vapor deposition of boron carbide (Parma: Union Carbide Corp.), 1969: p. 45.
17. Cholet, V., Herbin, P. and Vandenbulcke, L. CVD of boron carbide from BBr₃-CH₄-H₂ mixtures into a microwave plasma. in 9th Int. Symp. Boron, Borides and Related Compounds. 1987. Duisburg, FRG
18. Mazurowski, J., Ramseye, G. and Dowben, P. A. , Characterization of boron carbide thin films fabricated by plasma enhanced chemical vapor deposition from boranes. J. Appl. Phys., 1992. 72.
19. Hu, T., Steihl, L., Rafaniello, W., Fawcetta, T., Hawn, D. D., Mashall J. G., Rozeveld, S. J., Putzig, C. L., Blackson, J. H., Cermignani, W. and Robinson, M. G., Structures and properties of disordered boron carbide coatings generated by magnetron sputtering. Thin Solid Films 1988. 332.
20. Katz, J. D., Microwave Sintering of Ceramics. Annual Review of Materials Science 1992. 22.
21. Lazzari, R., Vast, N., Besson, J. M., Baroni, S. & Corso, A. D., Atomic Structure and Vibrational Properties of Icosahedral B₄C Boron Carbide. Phys. Rev. Lett., 1999. 83(3230).
22. Wei, J., Jiabg, B., Li, Y., Xu, C., Wu, D., and Wei, B., Straight boron carbide nanorods prepared from carbon nanotubes. Journal of Materials Chemistry, 2002. 12: p. 3121.
23. Mauri, F., Vast, N., and Pickard, C. J., Atomic Structure of Icosahedral B₄C Boron Carbide from a First Principles Analysis of NMR Spectra. Phys. Rev. Lett., 2001. 87(085506).
24. Pierson, H. O., Handbook of Refractory Carbides and Nitrides. 1996: William Andrew Publishing/Noyes.
25. Elliott, R. P. The boron carbon system. in Rep. ARF 220012: Armour Res. Found). 1961.
26. Emin, D., Structure and Single-Phase Regime of Boron Carbides. Phys. Rev. B, 1988. 38(9): p. 6041.

27. Kwei, G. H. a. M., B., Structures of the boron-rich boron carbides from neutron powder diffraction: Implications for the nature of the inter-icosahedral chains. *J. Phys. Chem.* , 1996. 100.
28. Wood, C., Emin, D. and Gray, P. E., Thermal Conductivity of Boron Carbides. *Phys. Rev. B*, 1985. 31: p. 6811.
29. Aselage, T. L., Emin, D. and McCready, S. S., Bipolaron hopping conduction in boron carbides. *Physica Status Solidi B*, 2000. 218(1): p. 255.
30. Gogotsi, G. A., Gogotsi, Y. G., and Ostrovoj, D. Y., Mechanical behaviour of hot-pressed boron carbide in various atmospheres *Journal of Materials Science Letters*, 1988. 7(8): p. 814.
31. Gogotsi, Y. G., Yaraoshenko, V. P., and Porz, F., Oxidation resistance of boron carbide-based ceramics. *Journal of Materials Science Letters*, 1992. 11: p. 308.
32. Viricelle, J. P., Goursat, P., and Bahloul-Hourlier, D., Oxidation Behaviour of Boron Carbide based Material in Dry and Wet Oxygen. *Journal of Thermal Analysis and Calorimetry*, 2001. 63: p. 507.
33. Makarenko, G. N. a. P., O. I., Comparative characteristics of phases in the boron-carbon and boronsilicon systems *J. Less Common Met.*, 1986. 117: p. 209.
34. Goeuriot, P., Thevenot, F. and Driver, J., Surface treatment of steels: Borudif, a new boriding process. *Thin Sol Films*, 1981. 78: p. 67.
35. Dash, R. K., Nikitin, A. and Gogotsi, Y., Microporous carbon derived from boron carbide. *Microporous and Mesoporous Materials*, 2004. 72.
36. Gogotsi, Y., Dash, R. K., Yushin, G., Yildirim, T., Laudisio, G., Fischer, J. E., Tailoring of Nanoscale Porosity in Carbide-Derived Carbons for Hydrogen Storage. *J. Am. Chem. Soc.*, 2005. 127: p. 16006.
37. Bouchacourt, M. a. T., F. , The properties and structure of the boron carbide phase. *J. Less Common Met.*, 1981. 82: p. 227.
38. Allen, R. D., The solid solution series, boron-boron carbide. *J. Am. Chem. Soc.*, 1953. 75.
39. Lipp, A. a. S., K. H. , airte und Hartebestimmung yon nichtmetallischen Hartstoffen. *Ber. Deutsch Keram. Ges*, 1975. 52.

40. Kaufmann, C., Cronin, D., Worswick, M., Pageau, G. and Beth, A., Influence of Material Properties on the Ballistic Performance of Ceramics for Personal Body Armor Shock and Vibration, 2003. 10: p. 51.
41. Holleck, H., Chem. Ztg., 1982. 106: p. 213.
42. Bourne, N. K. Shock-induced brittle failure of boron carbide in Proc. R. Soc. London Ser. A-Math. Phys. Eng. Sci. 2002.
43. Mashimo, T. a. U., M. J., Heterogeneous free-surface profile of B4C polycrystal under shock compression J. Appl. Phys., 1997. 81.
44. Johnson, G. R. and Holmquist, T. J., Response of boron carbide subjected to large strains, high strain rates, and high pressures J. Appl. Phys., 1999. 85: p. 8060.
45. Dandekar, D., Shock Response of Boron Carbide. 2001, Army Research Laboratory: Aberdeen Proving Ground, Aberdeen, MD.
46. Domnich, V., Gogotsi, Y., Trenary, M., and Tanaka, T., Nanoindentation and Raman spectroscopy studies of boron carbide single crystals. Appl. Phys. Lett., 2002. 81(20): p. 3783.
47. Vogler T. J., Reinhart, W. D., Chhabildas, L. C., and 95, Dynamic behavior of boron carbide. Appl. Phys. Lett., 2004. 92.
48. Grady, D. E., Dynamic Properties of Ceramic Materials. 1995, Sandia National Laboratory.
49. Moynihan, T. J., LaSalvia, J. C., and Burkins, M. S., in 20th International Conference at Ballistics. 2002: Orlando, FL.
50. D. Ge, V. D., T. Juliano, E. Stach, Y. Gogotsi, Structural damage in boron carbide under contact loading. Acta Materialia, 2004. 52(13): p. 3921.
51. Yan, X. Q., Li, W. J., Goto, T., and Chen, M. W., Raman spectroscopy of pressure-induced amorphous boron carbide. Appl. Phys. Lett., 2006. 88: p. 131905.
52. Yan, X. Q., Tang, Z., Zhang, L., Guo, J. J., Jin, C. Q., Zhang, Y., Goto, T., McCauley, J. W., and Chen, M. W., Depressurization Amorphization of Single-Crystal Boron Carbide. Phys. Rev. Lett., 2009. 102(7): p. 075505
53. Ghosh, D., Ghatu Subhash, Chee Huei Lee, and Yap, Y. K., Strain-induced formation of carbon and boron clusters in boron carbide during dynamic indentation. Appl. Phys. Lett., 2007. 91(6): p. 061910.

54. Schmechel, R., Werheit, H., Robberding, K. , IR Active Phonon Spectra of B–C–Al Compounds with Boron Carbide Structure. *Journal of Solid State Chemistry*, 1997. 33: p. 254.
55. Wood, C., Emin, D., Aselage, T., Beckel, C., and Howard, I., Boron-Rich Solids, in *AIP Conference Proceedings* C. Wood, Editor. 1986, American Institute of Physics: New York. p. 362.
56. Cai, K. F., Nan, C. W., and Min, X. M., The effect of silicon addition on thermoelectric properties of a B/sub 4/C ceramic. *Materials Science & Engineering B*, 1999. B67(3): p. 102.
57. G. Fanchini, D. E. N., R.A. Haber, J.W. McCauley, and M. Chhowalla, . V2ol. 27 Issue 7, p. 131, 2006. *Ceramic Engineering and Science Behavior of disordered boron carbide under stress*. 27(7): p. 131.
58. Mayerhöfer, J. P. a. T., Surface-enhanced Raman spectroscopy. *Analytical and Bioanalytical Chemistry*, 2009. 394(7): p. 1717.
59. Emory, S. N. a. S. R., Probing Single Molecules and Single Nanoparticles by Surface-Enhanced Raman Scattering *Science* 1997. 275(5303): p. 1102.
60. S. Stewart and Fredericks, P. M., Surface-enhanced Raman spectroscopy of peptides and proteins adsorbed on an electrochemically prepared silver surface. *Spectrochimica Acta Part A*, 1999. 55: p. 1615.
61. William L. Barnes, A. D. a. T. W. E., Surface plasmon subwavelength optics. *Nature*, 2003. 424: p. 824.
62. Goldstein, J. I., Newbury, D.E., Echlin, P., Joy, D.C., A. D. Romig, J., Lyman, C.E., Fiori, C. and Lifshin, E. , *Scanning Electron Microscopy and X-Ray Microanalysis: A Text for Biologists, Materials Scientists, and Geologists*. 2nd ed. 1992: Plenum Press, New York.
63. M. R. Derrick, E. F. D., A. E. Parker, and D. C. Stulik, Some new analytical techniques for use in conservaion. *Journal of American Institute of Conservation* 1994. 33(2): p. 171.
64. Haine, M. E. a. C., V. E., *The Electron Microscope*. 1961, London: Spon.
65. Newbury, D. E., Joy, D. C., Echlin, P., Fiori, C. E. and Goldstein, J. I., *Advanced Scanning Electron Microscopy and X-Ray Microanalysis*. 3 ed. 1986: Kluwer Academic/Plenum Press, New York.
66. Goodhew, P. J., Humphreys, J., and Beanland, R., *Electron Microscopy and Analysis*. 3rd ed. 2001, London: Taylor and Francis.

67. Williams, D. B. and Carter, C. B., Transmission Electron Microscopy. 1996, New York: Plenum.
68. Edington, J. W., Practical Electron Microscopy in Materials Science. 1991, Marietta: CBLIS.
69. Steeds, J. W., Introduction to Analytical Electron Microscopy. 1979, New York: Plenum.
70. Chen, M. W., McCauley, J. W., LaSalvia, J. C., and Hemker, K. J., Microstructural Characterization of Commercial Hot-Pressed Boron Carbide Ceramics. Journal of the American Ceramic Society, 2005. 88(7): p. 1955.
71. Bylander, B. M. and Kleinman, L., Structure of $B_{13}C_2$ Physical Review B, 1991. 43(2): p. 1487.
72. Ferrari, A. C. and Robertson, J., Interpretation of Raman spectra of disordered and amorphous carbon. Phys. Rev. B, 2000. 20(61): p. 14095.
73. Ferrari, A. C. and Robertson, J., Resonant Raman spectroscopy of disordered, amorphous, and diamondlike carbon. Phys. Rev. B 64, 2001. 64(7): p. 075414.
74. Lespadea, P., Al-Jishic, R., and Dresselhaus, M. S., Model for Raman scattering from incompletely graphitized carbons Purchase the full-text article. Carbon, 1982. 20(5): p. 427.
75. Matthews, M. J., Pimenta, M. A., Dresselhaus, G., Dresselhaus, M. S., and Endo, M., Origin of dispersive effects of the Raman D band in carbon materials. Phys. Rev. B, 1999. 59(10): p. R6585.
76. Tuinstra, F. and Koenig, J. L., Raman spectrum of graphite. J. Chem. Phys. , 1970. 53(3): p. 1126.
77. Werheit, H., Rotterb, H. W., Meyerc, F. D., Hillebrechte, H., Shalamberidzed, S. O., Abzianidzed, T. G., and Esadze, G. G., FT-Raman spectra of isotope-enriched boron carbide. Journal of Solid State Chemistry, 2004. 177(2): p. 569.
78. LaSalvia, J., McCuiston, R. C., Fanchini, G., McCauley, J. W., Chhowalla, M., Miller, H. T., and MacKenzie, D. E. Shear Localization in Sphere-Impacted Armor-Grade Boron Carbide. in 23rd International Symposium on Ballistics. 2007. Tarragona, Spain.
79. Shirai, K. and Emura, S., Lattice vibrations and the bonding nature of boron carbide. J. Phys.: Condens. Matter 1996. 8(50): p. 10919.

80. Moskovits, M., Surface-enhanced spectroscopy. *Rev. Mod. Phys.*, 1985. 57(3): p. 783.
81. Tallant, D. R., Aselage, T. L., Campbell, A. N., and Emin, D., Boron carbide structure by Raman spectroscopy. *Phys Rev. B*, 1989. 40(8): p. 5649.
82. Dresselhaus, M. S. and Eklund, P. C., Phonons in carbon nanotubes. *Adv. Phys.*, 2000. 49(6): p. 705.
83. Thomsen, C. and Reich, S., Double Resonant Raman Scattering in Graphite. *Phys. Rev. Lett.*, 2000. 85(24): p. 5214.
84. Ashcroft, N. W. and Mermin, N. D., *Solid State Physics*. 1976, Philadelphia: Saunders College.
85. Hummer, K., Puschnig, P., and Ambrosch-Draxl, C., Ab initio study of anthracene under high pressure. *Phys. Rev. B*, 2003. 67(18): p. 184105.
86. Ferrari, A. C. and Robertson, J., Origin of the 1150-cm⁻¹ Raman mode in nanocrystalline diamond. *Phys Rev. B*, 2001. 63(12): p. 121405(R).
87. Profeta, M. and Mauri, F., Theory of resonant Raman scattering of tetrahedral amorphous carbon. *Phys Rev. B*, 2001. 63(24): p. 245415.
88. Cronin, D. S., McIntosh, G., Kaufman, C., Bul, K., and Berstad, T. in 4th European LS-DYNA Users Conference Proceedings. 2003. Ulm, Germany.
89. Ge, D., Domnich, V., Juliano, T., Stach, E., and Gogotsi, Y., Structural damage in boron carbide under contact loading. *Acta Materialia*, 2004. 52(13): p. 3921.
90. Fanchini, G., Gupta, V., Mann, A. B., and Chhowalla, M., Unpublished, Submitted for Publication. 2009.
91. Fanchini, G., Tagliaferro, A., and Ray, S. C., Electronic and Vibrational Structures of Amorphous Carbon Nitrides. *Diam. Rel. Mater.*, 2003. 12: p. 208.
92. Samara, G. A., Emin, D., and Wood, C., Pressure and Temperature Dependences of the Electronic Conductivity of Boron Carbides. *Phys Rev. B*, 1985. 32(4): p. 2315.
93. Wood, C. and Emin, D., Conduction Mechanism in Boron Carbide. *Phys. Rev. B*, 1984. 29: p. 4582.
94. Dasgupta, D., Demichelis, F., and Tagliaferro, A. B., Electrical Conductivity of Amorphous Carbon and Amorphous Hydrogenated Carbon. *Phil. Mag. b*, 1991. 63(6): p. 1255.

95. Petrovic, J. J., McClellan, K. J., Kise, C. D., Hoover, R. C., and Scarborough, W. K. Functionally Graded Boron Carbide. in *Ceram. Eng. Sci. Proc.* 1998.
96. Ulrich, S., Ehrhardt, H., Schwan, J., Samlenski, R., and Brenn, R., Subplantation effect in magnetron sputtered superhard boron carbide thin films. *Diamond Relat. Mater.*, 1998. 7: p. 835.
97. Guo, L., Singh, R., and Kleebe, H., Growth of Born-Rich Nanowires by Chemical Vapor Deposition (CVD). *Journal of Nanomaterials*, 2006: p. 1.
98. Ma, R. and Bando, Y., Investigation of the Growth of Boron Carbide Nanowires. *Chem. Mater.* , 2002. 14: p. 4403.
99. Ma, R. and Bando, Y., High purity single crystalline boron carbide nanowires. *Chemical Physics Letters*, 2002. 364: p. 314.
100. Mondal, S. and Banthia, A. K., Low-temperature synthetic route for boron carbide. *Journal of the European Ceramic Society* 2005. 25: p. 287.
101. Pender, M. J., Forsthoefel, K. M., and Sneddon, L. G., Molecular and polymeric precursors to boron carbide nanofibers, nanocylinders, and nanoporous ceramics. *Pure Appl. Chem.*, 2003. 75(9): p. 1287.
102. Pender, M. J. and Sneddon, L. G., An Efficient Template Synthesis of Aligned Boron Carbide Nanofibers using Nanofibers using a Single-Source Molecular Precursor. *Chem. Mater.*, 2000. 12(2): p. 280.
103. Pender, M. J. and Sneddon, L. G., Polyalkenyldecaboranes: New Polymeric Precursors to Boron Carbide Ceramics. *Polymer Chemistry*, 2000. 41(1): p. 551.
104. Han, W., Silicon Doped Boron Carbide Nanorod Growth via a Solid-Liquid-Solid Process. *Applied Physics Letters*, 2006. 88: p. 133118.
105. Lourie, O., Jones, C., Bartlett, B., Gibbons, P., Ruoff, R., and Buhro, W., CVD Growth of Boron Nitride Nanotubes. *Chem. Mater.*, 2000. 12: p. 1808.
106. Ahlen, N., Johnsson, M., and Nygren, M., Carbothermal synthesis of TiC whiskers via a vapor-liquid-solid growth mechanism. *Journal of the American Ceramic Society*, 1996. 79(11): p. 2803.
107. Johnsson, M. and Nygren, M., Carbothermal synthesis of TaC whiskers via a vapor-liquid-solid growth mechanism. *J. Mater. Res.*, 1997. 12(9): p. 2419.
108. Gogotsi, Y., Carbon Nanomaterials. *Advanced Materials and Technologies*, ed. Gogotsi. Vol. 1. 2006: CRC Press, Boca Raton. 350.

109. Liao, P. K. and Spear, K. E., The B--Co (Boron--Cobalt) System. Bull. Alloy Phase Diagrams, 1988. 9(4): p. 452.
110. Liao, P. K. and Spear, K. E., Alloy Phase Diagrams. ASM Handbook. Vol. 3. 1992: ASM International, Materials Park, OH.
111. Olesinski, R. W. and Abbaschian, G. J., The C--Si (Carbon--Silicon) System Bull. Alloy Phase Diagrams, 1984. 5(5): p. 486.
112. Lavrenko, V. A. and Gogotsi, Y. G., Influence of Oxidation on the Composition and Structure of the Surface Layer of Hot-Pressed Boron Carbide. Oxidation of Metals, 3/4, 1988, 1988. 29(3/4): p. 193.
113. Lavrenko, V. A. and Gogotsi, Y. G., Corrosion of structural ceramics. 1989, Moscow: Metallurgiya.
114. Matje, P. and Schwetz, K. A. in Ceramic Powder Processing Science, Proceedings of the 2nd International Conference. 1988. Berchtesgaden, FRG.
115. Litz, L. M. and Mercuri, R. A., Oxidation of Boron Carbide by Air, Water, and Air-Water Mixtures at Elevated Temperatures. J. Electrochem. Soc., 1963. 110(8): p. 921.
116. Wagner, R. S. and Ellis, W. C., Vapor-liquid-solid mechanism of single crystal growth. Applied Physics Letters 1964. 4: p. 89.
117. Y. Cui, L. I. Lauhon, M. S. Gudiksen, G. Wang, and Lieber, C. M., Diameter-controlled synthesis of single-crystal silicon nanowires. Appl. Phys. Lett., 2005. 86: p. 123109.
118. Baker, H., Alloy Phase Diagrams. ASM handbook, ed. H. BAKER. Vol. 3. 1992, Metals Park, Ohio: ASM International.
119. G. Zhou, J. C. Yang, F. Xu, J. A. Barnard, and Z. Zhang. Quantitative V-L-S Growth Model and Experiments of Fe Catalyzed Si Nanowire Formation. in Mat. Res. Soc. Symp. Proc. 2003.
120. V. G. Dubrovskii, N. V. Sibirev, G. E. Cirilin, C. Harmand, and Ustinov, V. M., Theoretical analysis of the vapor-liquid-solid mechanism of nanowire growth during molecular beam epitaxy. Phys Rev E, 2006. 73(21603).
121. J. Bauer, V. Gottschalch, H. Paetzelt, G. Wagner, B. Fuhrmann, and Leipner, H. S., MOVPE growth and real structure of vertical-aligned GaAs nanowires. Journal of Crystal Growth, 2007. 298: p. 625.

122. Seifert, H. J. and Aldinger, F., Structure and Bonding—High Performance Non-Oxide Ceramics. Vol. 101. 2002: Springer-Verlag Berlin, Hiedelberg 58.
123. Cao, Q., Kim, H. S., Pimparkar, N., Kulkarni, J. P., Wang, C. J., Shim, M., Roy, K., Alam, A., and Rogers, J. A., Medium-scale carbon nanotube thin-film integrated circuits on flexible plastic substrates. *Nature*, 2008. 454: p. 495.
124. Forrest, S. R., The path to ubiquitous and low-cost organic electronic appliances on plastic. *Nature*, 2004. 428: p. 911.
125. Forrest, S. R. and Thompson, M. E., Introduction: Organic electronics and optoelectronics. *Chemical Reviews*, 2007. 107: p. 923.
126. Kim, D. H. and Rogers, J. A., Stretchable Electronics: Materials Strategies and Devices. *Advanced Materials*, 2008. 20: p. 4887.
127. Gruner, G., Carbon Nanotube Networks for Transparent and Flexible Electronics. *Journal of Materials Chemistry*, 2006. 6: p. 3533.
128. Ju, S., Li, J. F., Liu, J., Chen, P. C., Ha, Y. G., Ishikawa, F., Chang, H., Zhou, C. W., Facchetti, A., Janes, D. B., and Marks, T. J., Transparent active matrix organic light-emitting diode displays driven by nanowire transistor circuitry. *Nano Letters*, 2008. 8: p. 997.
129. Kim, S., Ju, S., Back, J. H., Xuan, Y., Ye, P. D., Shim, M., Janes, D. B., and Mohammadi, S., Fully Transparent Thin-Film Transistors Based on Aligned Carbon Nanotube Arrays and Indium Tin Oxide Electrodes. *Advanced Materials*, 2008. 20: p. 1.
130. Viswanath, R., Wakharkar, V., Watwe, A., and Lebonheur, V., Thermal performance challenges from silicone to systems. *Intel Technol, J.*, 2000. Q3: p. 1.
131. Cok, R. S., OLED Display Having Thermally Conductive Adhesive. United States Patent, 2007.
132. For information on Arlon Technology Enabling Innovation, see: <http://www.pcb007.com/preshow/newpro.htm> and <http://www.arlon-std.com/>.
133. King, J. A., Miller, M.G.,Barton, R.L.,Keith, J.M.,Hauser, R.A.,Peterson, K.R. and Sutter, L.L., Thermal and electrical conductivity of carbon-filled liquid crystal polymer composites. *Journal of Applied Polymer Science*, 2005. 99(4): p. 1552.
134. King, J. A., Barton, R.L.,Hauser, R.A. and Keith, J.M., Synergistic Effects of Carbon Fillers in Electrically and Thermally Conductive Liquid Crystal Polymer Based Resins. *Polymer Composites*, 2008. 29(4): p. 421.

135. Strümpfer, R., Maidorn, G. and Rhyner, J., Fast current limitation by conducting polymer composites. *J. Appl. Phys.*, 1997. 81(10): p. 6786.
136. Agari, Y., Ueda, A., and Nagai, S., Thermal conductivities of composites in several types of dispersion systems. *J. Appl. Polym. Sci.*, 1991. 42(6): p. 1665.
137. Bigg, D., Thermal conductivity of heterophase polymer compositions. *Therm. Electr. Conduct. Polym. Mater.* Berlin/Heidelberg, Springer, 1995: p. 1.
138. Bryning, M. B., Islam, M. F., Kikkawa, J. M., and Yodh, A. G., Very Low Conductivity Threshold in Bulk Isotropic Single-Walled Carbon Nanotube-Epoxy Composites. *Advanced Materials*, 2005. 17(9): p. 1186.
139. Bryning, M. B., Milkie, D. E., Islam, M. F., Kikkawa, J. M., and Yodh, A. G., Thermal conductivity and interfacial resistance in singlewall carbon nanotube epoxy composites. *Appl. Phys. Lett.*, 2005. 87: p. 1619091.
140. Huxtable, S. T., Cahill, D. G., Shenogin, S., Xue, L., Ozisik, R., Barone, P., Usrey, M., Strano, M. S., Siddons, G., Shim, K. S., and Keblinski, P., Interfacial heat flow in carbon nanotube suspensions. *Nature Materials*, 2003. 2: p. 731.
141. Moniruzzaman, M. and Winey, K. I., Polymer nanocomposites containing carbon nanotubes. *Macromolecules*, 2006. 39: p. 5194.
142. Kim, S. R., Kim, D. H., Kim, D. J., Kim, M. H., and Park, J. M., Study on thermal conductivity of PEEK/thermally conductive filler composites. *Solid State Phenomena*, 2007. 124: p. 1079.
143. Alexandre, M. and Dubois, P., Polymer-layered silicate nanocomposites: preparation, properties and uses of a new class of materials. *Materials Science and Engineering: R*, 2000. 28: p. 1.
144. Berber, S., Kwon, Y. K., and Tománek, D., Unusually High Thermal Conductivity of Carbon Nanotubes. *Phys. Rev. Lett.*, 2000. 84: p. 4613.
145. Kim, P., Shi, L., Majumdar, A. and McEuen, P. L., Thermal Transport Measurements of Individual Multiwalled Nanotubes. *Phys. Rev. Lett.*, 2001. 87(21): p. 215502.
146. Gupta, V., Fanchini, G., Miller, S., Al-Sharab, J. E., Bentley, J., and Chhowalla, M., Effect of Growth Parameters and Si-doping on Boron Carbide Nanostructures. Submitted, 2008.
147. Gordeyev, S. A., Macedo, F. J., Ferreira, J. A., van Hattum, F. W. J., and Bernardo, C. A., Transport properties of polymer-vapour grown carbon fibre composites. *Physica B: Condensed Matter*, 2000. 279(1-3): p. 33.

148. Thostenson, E. T. and Chou, T. W., Aligned multi-walled carbon nanotube-reinforced composites: processing and mechanical characterization. *J. Phys. D: Appl. Phys.*, 2002. 35(16): p. L77.
149. Ramanathan, T., Abdala, A. A., Stankovich, S., Dikin, D. A., Herrera-Alonso, M., Piner, R. D., Adamson, D. H., Schniepp, H. C., Chen, X., Ruoff, R. S., Nguyen, S. T., Aksay, I. A., Prud'Homme, R. K., and Brinson, L. C., Functionalized graphene sheets for polymer nanocomposites. *Nature Nanotechnology*, 2008. 3(6): p. 327.
150. See for example information provided at: <http://www.azom.com/details.asp?ArticleID=75>.
151. Yu, C., Kim, Y. S., Kim, D., and Grunlan, J. C., Thermoelectric behavior of segregated-network polymer nanocomposites. *Nano Letters*, 2008. 8(12): p. 4428.
152. Yu, A., Itkis, M. E., Berkysarova, E., and Haddon, R. C., Effect of single-walled carbon nanotube purity on the thermal conductivity of carbon nanotube-based composites. *Appl. Phys. Lett.*, 2006. 89: p. 1331021.
153. Tu, H. and Ye, L., Thermal conductive PS/graphite composites. *Polymers for Advanced Technologies*, 2008. 20(1): p. 21.
154. Hu, L., Hecht, D. S., and Gruner, G., Percolation in transparent and conducting carbon nanotube networks. *Nano Letters*, 2004. 4: p. 2513.
155. Balandin, A. a. W., K.L., Significant decrease of the lattice thermal conductivity due to phonon confinement in a free-standing semiconductor quantum well. *Physical Review B*, 1998. 58(3): p. 1544.
156. Al-Saleh, M. H. and Sundararaj, U., A review of vapor grown conductive composites. *Carbon*, 2009. 47(1): p. 2.

APPENDIX

I. List of Abbreviations

B ₄ C	Boron Carbide
TEM	transmission electron microscopy
DAC	diamond anvil cell
SEM	scanning electron microscopy
DP	diffraction pattern
SAD	selected area diffraction
BF	bright filed
DF	dark field
DFT	density functional theory
XRD	X-ray diffraction
SAX	small angle X-ray diffraction
SERS	surface enhanced Raman spectrscopy
HRTEM	high resolution transmission electron microscopy
EDS	energy dispersive X – ray spectrometer
EELS	electron energy loss spectrometer
FFT	fast Fourier transformation

VITA

Name:	Varun Gupta
Education:	<p>Ph.D. Materials Science and Engineering, Rutgers University, Philadelphia, NJ 2010</p> <p>M.S. Materials Science and Engineering, Drexel University, Philadelphia, PA 2006</p> <p>B.Tech. Ceramic Engineering, Institute of Technology-Banras Hindu University, (IT-BHU), Varansi, India 2003</p>
Professional experience	<p>Summer Intern, Bristol Myers Squibb, Co., U.S. Pharmaceuticals, 777 Scudder Mills. Road Plainsboro, NJ 08774, June 2009-August 2009</p> <p>Graduate Assitant, Department of Materials Science and Engineering, Rutgers University, Piscataway, NJ 2006 – 2009</p>
Publications	<ol style="list-style-type: none"> 1. Seung Yol Jeong, Bhavin Parekh, <u>Varun Gupta</u>, Giovanni Fanchini, and Manish Chhowalla, “Direct thin film formation of isolated single-walled carbon nanotube networks via room temperature deposition”, Submitted (2010). 2. S. R. Kim, <u>V. Gupta</u>, S. W. Yim, M. Chhowalla, “Transparent and thermally conducting nanocomposites from ultra-long boron carbide nanowires and poly(methyl methacrylate)”, Submitted (2009). 3. <u>Varun Gupta</u>, Giovanni Fanchini, Steve Miller, Jafar El-Sharab, Jim Bentley and Manish Chhowalla, “Effect of Growth Parameters and Silicon doping on Boron Carbide Nanostructures”, Submitted (2009). 4. Al-Sharab, J. F., <u>Gupta, V.</u>, Bentley, J., Chhowalla, M., EELS and EDS Compositional Imaging of B₄C Nanostructures Synthesized by a Solid-Liquid-Solid Method, <i>Microscopy and Microanalysis</i>, vol. 15, issue S2, p. 1252 (2009). 5. Giovanni Fanchini, <u>Varun Gupta</u>, Adrian Mann and Manish Chhowalla, “Assessment of boron carbide samples for armor applications by Raman and surface-enhanced-Raman spectroscopy”, Submitted (2009). 6. Giovanni Fanchini, <u>Varun Gupta</u>, Adrian Mann and Manish Chhowalla, “<i>In Situ</i> Monitoring of Structural Changes in Boron Carbide Under Electric Fields”, <i>Journal of the American Ceramic Society</i>, Volume 91 Issue 6, Pages 2666-2669 (2008). 7. N Raykar, <u>V Gupta</u>, B Kear, M Chhowalla, A B Mann “Nanomechanics of a high H/E carbonaceous material” <i>Scripta Materialia</i> 57 925-928 (2007).